MODELING BRANCHED WIRING NETWORKS

USING INVERSION

by

Carl Petter Brewer

A thesis submitted to the faculty of
The University of Utah
in partial fulfillment of the requirements for the degree of

Master of Science

Department of Electrical and Computer Engineering

The University of Utah

May 2011

The University of Utah Graduate School

STATEMENT OF THESIS APPROVAL

The thesis of Carl Petter Brewer
has been approved by the following supervisory committee members:

Cynthia Furse	, Chair	1/31/10 Date Approved
Paul Smith	, Chair	10/27/10 Date Approved
Chet Lo	, Chair	 Date Approved

and by Gianluca Lazzi , Chair of
the Department of Electrical and Computer Engineering

and by Charles A. Wight, Dean of The Graduate School.

ABSTRACT

A network algorithm is developed to analyze a branched wire network to determine the branch and fault topology of the network, using an array of hand-held (EM) electro-magnetic field sensors in conjunction with a SSTDR (Spread-Spectrum Time Domain Reflectometry) wire tester. The algorithm provides an analysis of the convolved reflectometry data collected at multiple data points along a test wire by the field sensors. The faults are located using a reconstruction of forward and backward traveling waveforms created from a mathematical inversion of a collection of convolved reflectometry data. The methods and algorithms developed to model the topology of the test wires are described. The topology refers to the locations of the major reflection points within a branched network, and the lengths and connections of the segments of wire that exist between reflectors. Simulations are developed to determine the effectiveness of the algorithm without the limitations of the test hardware. Tests are performed in a controlled lab environment to assess the abilities of the developed algorithms.

TABLE OF CONTENTS

LIST OF FIGURES

LIST OF TABLES

LIST OF ACRONYMS

DTF	Distance To Fault, as calculated from a signal source
EM probe	Electro-Magnetic probe, an array of antennas combined into one handheld probe used to sense electric and magnetic fields
STDR	Sequence Time Domain Reflectometry
SSTDR	Spread Spectrum Time Domain Reflectometry
TDR	Time Domain Reflectometry
VOP	Velocity Of Propagation

LIST OF VARIABLES

Γ	Reflection coefficient, a ratio of the amount of signal that is reflected.
Z_L	Load impedance or impedance anomaly.
Z_0	Characteristic transmission impedance of the line (typically 50-300 Ohms).
$V_{reflected}$	Voltage reflected back to the source at a particular point.
$V_{incident}$	Incidental voltage as it was presented by the source.
$\mathbf{m}_{real}$	Matrix of values that ultimately comprise the theoretical model, a precise combination of all convolved traveling waveforms on the wire bundle. This represents the measured model, if it were measurable.
$\mathbf{A}$	Forward operator performed upon the waves to create data. In this thesis it represents the sum operation of each component of **g** at a given location and point in time.
$\mathbf{d}_{calc}$	Resultant data of the forward operation A performed on the theoretical model $\mathbf{m}_{real}$.
$\mathbf{m}$	Matrix of values comprising a model of the forward and backward traveling waveforms as observed from the source. The model is estimated using inversion techniques.
$\delta\mathbf{m}$	Change in the model from one iteration to the next.
$\mathbf{d}$, $\mathbf{d}_{meas}$	Rows of measured data points. In this thesis this is the convolved TDR data collected by the hardware.

$\mathbf{A}^{-1}$	Inverse of the forward operator **A**. In this thesis it represents the separation process of waveform components that cause the measured data $\mathbf{d}_{meas}$.
ϕ	The misfit, or difference between the measured and calculated result. $\phi(\mathbf{m})$ refers to the difference between the data calculated from the model estimate and actual data.
D	Denotes the dimensional space of the data d. See Equation 24 for an example of how data space is organized for this thesis.
M	Denotes the dimensional space of the model **m.** See Equation 26 for an example of how data space is organized for this thesis.
μ^2	The squared norm.
$\mathbf{F_m}$	The Frechet derivation of A.
$\mathbf{F_m^*}$	The mathematical inverse of the Frechet derivative.
$\mathbf{L(m)}$	Matrix of values describing the direction of steepest ascent, or wrong direction, for finding the most accurate model.
$\boldsymbol{k}$	The vector of values describing the calculated step-size in which to move in the direction of steepest descent.
$\mathbf{g}$	Intermediate matrix of values used to calculated $\boldsymbol{k}$.
n	Represents the current iteration of the steepest descent formula.
N	The total number of iterations of the formula performed.
$\mathbf{r}_n$	The misfit for one iteration, n, or difference between the data produced by the estimated model and the measured data.
ε_0	The predetermined level of acceptable error in the estimate of the model.
c	The speed of light constant.
VOP	The velocity of propagation for electricity on a given wire.

$(\,)_{fb}$	Refers to a matrix organized in model space M, so that row one contains information for the forward traveling waveform, and row two contains information for the backward traveling waveform. Each row can be individually identified using $(\,)_f$ or $(\,)_b$ symbols.
j	Generic variable for one specific index into either the forward or backward vector.
Fcol, Bcol, Dcol, Mcol, Gcol	The column vector of the associated matrix, $\mathbf{L}_f$, $\mathbf{L}_b$, **d**, **m**, and **g**.
Drow, Grow	The row vector of the associated matrix, **d** and **g**.
$\#Fcols, \#Bcols, \#Dcols, \#Mcols$	Constant number of column elements of the associated vector.

LIST OF DEFINITIONS

Forward Traveling Waveform – The patterns of the convolved TDR signal that appears to travel from the direction of the source to the EM probe, when moving the probe along the cable away from the source. This includes elements of the convolved signal coming either from the source or from reflection points on other branches whose branching point exists between the source and the EM probe.

Backward Traveling Waveform – The patterns of the convolved TDR signal that appears to travel from the direction of the wire or branch to the source, when moving the probe along the cable toward the source. This includes all reflected elements of the convolved signal caused by reflectors that have not yet been passed by the sensor.

Branched Wire - A branched wire is defined for this research as a minimum of two wires that have been electrically spliced, so that the original paired wires split off into two branches of paired wires. Many of the figures in this document show one line to represent the identical topology of both the test and reference wire.

Wire Segment – A section of the test wire on which no major reflection points exist. A wire network is divided into segments by reflection points.

Reflection Point – The location of an impedance mismatch on a wire that causes electrical signals to fully or partially reflect. Reflection points can be caused by open circuits, short circuits, branch points, or any other thing that significantly changes the impedance at a single point on the wire.

Network Topology - The topology described here refers to the locations of the major reflection points within a branched network, and the lengths and connections of the segments of wire that exist between reflectors. This definition assumes that all branches (splices) occur to both the test wire and the reference wire used for the test.

CHAPTER 1

INTRODUCTION

Aging electrical wiring is among the most expensive and frustrating systems to maintain on aircraft. As an example, the US Navy currently expends approx. 1.8 million staff-hours annually troubleshooting and repairing aircraft wiring systems [1]. Modern commercial aircraft are known to have more than 100 km of wire [3]. Electrical faults generally occur with no apparent warning, often grounding the aircraft and requiring immediate attention, or potentially causing catastrophic failure, as has been implicated in several serious accidents including the explosion of Swiss Air Flight 111 [9] and TWA Flight 800 [4].

During the lifetime of aircraft wires, they become subject to a variety of electrical, chemical and mechanical stresses. Abruptly or over time, these stresses lead to cracks, abrasions, breaks, loose connections, and other damage. Wire faults include open circuits, short circuits, intermittent shorts, and unintended connections. Because this damage can lead to serious failures and expensive repairs, such damage is best corrected as soon as it can be detected. In addition to aircraft, nuclear power plants, communication infrastructure, mass transit systems, and many other applications are subject to the risks of downtime and/or potential fire hazard or loss of control from aging wiring.

Technologies exist, or are being developed, that can detect and provide a distance to these faults in aircraft wiring [11] [2]. Once a fault is detected, a maintainer has two

choices: repair the existing wire, or replace the wire. Replacing the wire can be a very costly process, often involving the replacement of the entire wiring bundle. Often aircraft wiring is routed behind panels or wrapped in special protective jackets, and is often subject to tight routing and bundling. Repair can also be a costly process if the location of the fault is not known. This may involve exposing the entire wire, one panel at a time, until a visual inspection verifies a damaged wire. To further complicate that process, many wiring faults are not visually observable.

On top of this, multiple branches are possible within wiring systems and exist with a variety of terminations. Wiring faults can occur at any location within the network of wires. Determining the location of the fault within a branched network can be extremely difficult with the set of tools available to maintainers today.

To simplify the troubleshooting and maintenance process, two pieces of knowledge are desirable: numerical distance to the fault, and physical location of the fault. Armed with this knowledge, a wiring maintainer could quickly and efficiently repair wiring damage. This knowledge can greatly reduce overall costs to an airline due to reduced aircraft downtime and maintenance costs. Emerging technology can provide a numerical distance to the fault, but does not provide a physical location or specify the branch on which a fault occurred [11].

The state of the art includes a method published for modeling wiring network topologies [7]. The method divides the problem into two main issues: the ability to identify reflections caused by faults and branches, and the analysis of the reflections to determine the topology of the network. The authors focus on the latter, and are able to successfully map several network topologies. Successful determination of the topology is

dependent on accurate identification of the reflections. At the present time, this also depends on the algorithms' ability to effectively peel away a wave from the data in order to analyze the next wave in line. The presence of noise and overlapping reflections can make this difficult. By using inversion and multiple electromagnetic sensor positions, waves can be isolated into their respective models. This enables algorithms to more successfully calculate the distance to those waves, in turn providing a more accurate distance to the fault, branch, or endpoint, and ultimately a more accurate network topology.

The purpose of the methods derived in this paper is to reliably guide an aircraft wiring maintainer to the precise location of an existing fault on an unbranched and branched wire. Using the methods described with the proper hardware could allow the maintainer to quickly locate the fault within +/- 1.5 ft, even if the wire bundles are hidden behind nonmetallic paneling, as is common in the interior of aircraft.

This thesis develops and quantifies the ability to separate and model reflectometry signals in order to characterize simple unbranched and branched wiring network topologies. Data are collected using a reflectometry system in tandem with a field sensor at multiple positions, analyzed, and information about that network is displayed to the user.

CHAPTER 2

BACKGROUND

2.1 Reflectometry

2.1.1 General Reflectometry Theory

Time Domain Reflectometry (TDR) and its derivatives are common technologies employed to find static faults in wires. Spread spectrum time domain reflectometry (SSTDR) and sequence time domain reflectometry (STDR) are demonstrated methods for location of faults on unbranched electrical wiring [11].

Reflectometry is the practice of propagating a signal onto a transmission line, and recording and analyzing the signals that reflect back to the source. The reflected signals can be analyzed for timing delay, distortion, and duplication to understand the nature of the transmission line. The propagated signal will reflect off of significant impedance changes along the transmission line, such as those caused by discontinuities. The wave reflected from a particular section along a transmission line is proportional to its reflection coefficient:

$$\boldsymbol{\Gamma = \frac{Z_L - Z_0}{Z_L + Z_0} = \frac{V_{reflected}}{V_{incident}}} \qquad \textbf{Equation 1}$$

where Γ is the reflection coefficient, Z_L is the load impedance or impedance anomaly, Z_0 is the characteristic transmission impedance of the line (typically 50-300 Ohms) [12],

$V_{reflected}$ is the voltage reflected back to the source, and $V_{incident}$ is the incidental voltage as it was presented by the source.

To apply the theory, if one were to divide a conductor up into measureable sections and apply this equation to each section, they would find that the reflected wave, proportional to the reflection coefficient, would be larger for sections where the line impedance was significantly different from the characteristic impedance.

Reflected signals are collected, generally at the source, and compared to the incident signal. The time delay between the incident and reflected waves is converted to a distance using a measured or assumed velocity of propagation, providing a distance to fault (DTF) measurement. Figure 1 shows an example of the mechanics of reflectometry as it is applied to wire testing.

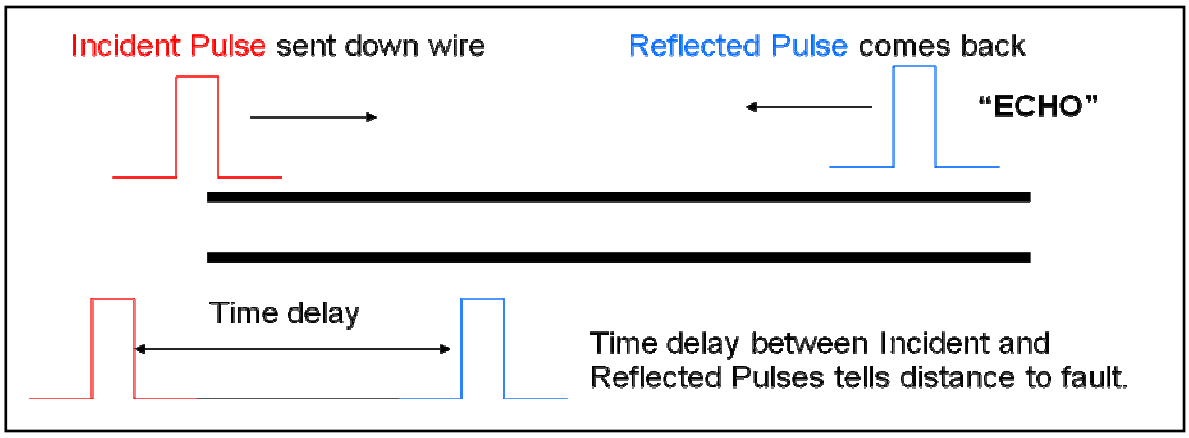

Figure 1: Example showing the mechanics of reflectometry as it is applied to wire testing.

2.1.2 SSTDR Reflectometry Methods

STDR and SSTDR are specific forms of reflectometry that are particularly effective on wiring. Spread spectrum is the method of spreading the signal power spectrum over a broad bandwidth. These methods utilize a digital pseudo-noise (PN) code or sine wave modulated PN code as test signals for advanced reflectometry measurements. The high frequency PN code passes down the wire and reflects at any impedance discontinuity such as an open circuit or short circuit. Impedance mismatches produce reflections of the test signal which return to the test location like 'echoes' of the initial response. The electrical echoes are then correlated with the original test signal by hardware on the S/SSTDR tester to determine the time delay between the incident signal and the reflected echo. The correlation is a comparison of the returning PN code to an internal copy of the PN code. These are continuously correlated as the returning PN code passes. The result (sample) of each correlation is stored as a voltage level. Because samples are collected at a uniform rate, each sample can be directly related to a period of time, and hence a distance to fault.

2.1.3 Testing Branched Wire Networks

Branched networks of wires, such as those often encountered in power distribution systems on aircraft, create significant challenges in the interpretation of the signatures for any reflectometry method, including STDR and SSTDR [2]. A branched wire is one that has been spliced, so that the original wire and also its ground or reference wire split off into two or more branches. This is different from a branching bundle of wires, where some of the wires are routed in one direction, and the rest in another direction. This research also assumes that the reference wire follows the topology of the

test wire, meaning that two wires are branched at the same location, as is depicted in Figure 2.

Branched wires are challenging for all reflectometry test systems because impedance mismatches and their resultant reflections and multiple reflections occur at the branch locations. The fact that the reflections get smaller and smaller beyond the multiple junctions of a branched network makes it very difficult to locate faults beyond the branch. The 'deeper' within the network, the more difficult the detection of the fault location becomes. Depending on the sensitivity (signal to noise ratio) of the reflectometry equipment, these faults will become impossible to find as they are imbedded deeper and deeper within the network.

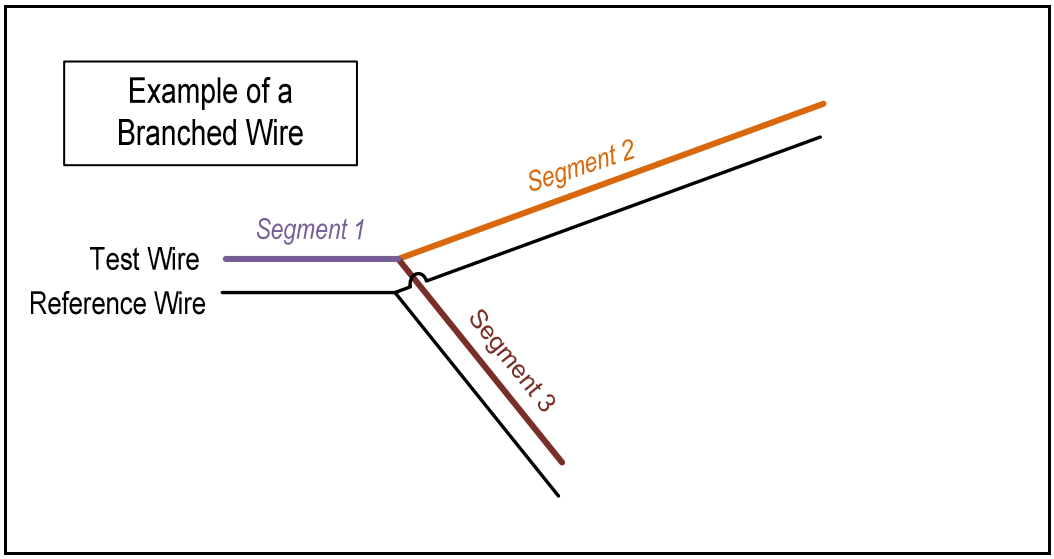

Figure 2: Example of a branched test wire and its reference. The reference wire is assumed in all other figures.

2.2 Data Collection Hardware

2.2.1 SSTDR Hardware

S/SSTDR methods can be used to detect faults on wiring, but present implementations fall short of being able to determine the branch on which a fault exists, or physically locating the fault. To improve the ability to analyze branched wires, signal analysis methods are combined with an electric and magnetic sensing wand (EM probe) and S/SSTDR tester [5].

The major tasks performed by the tester are summarized as follows:

1. Generation of a pseudo-noise (PN) signal, consisting of a particular 1023-bit sequence transmitted at a frequency of 144 MHz.
2. Propagation of the PN signal onto the test wire.
3. Collection of the reflected PN signals from the test wire with proper filtering and surge protection. Data are collected at a rate of 1 test per millisecond.
4. Correlation of the reflected PN signal to the original signal, producing a set of data points containing signature waveforms which relate to the time-delayed reflection of the PN signal off of faults, branches and endpoints.
5. Storage and/or transfer of data sets for analysis.
6. Data analysis is performed within the tester or externally.

A typical test scenario includes the tester, the EM sensor (consisting of the probe and handheld), and a test harness or bundled wires as depicted in Figure 3.

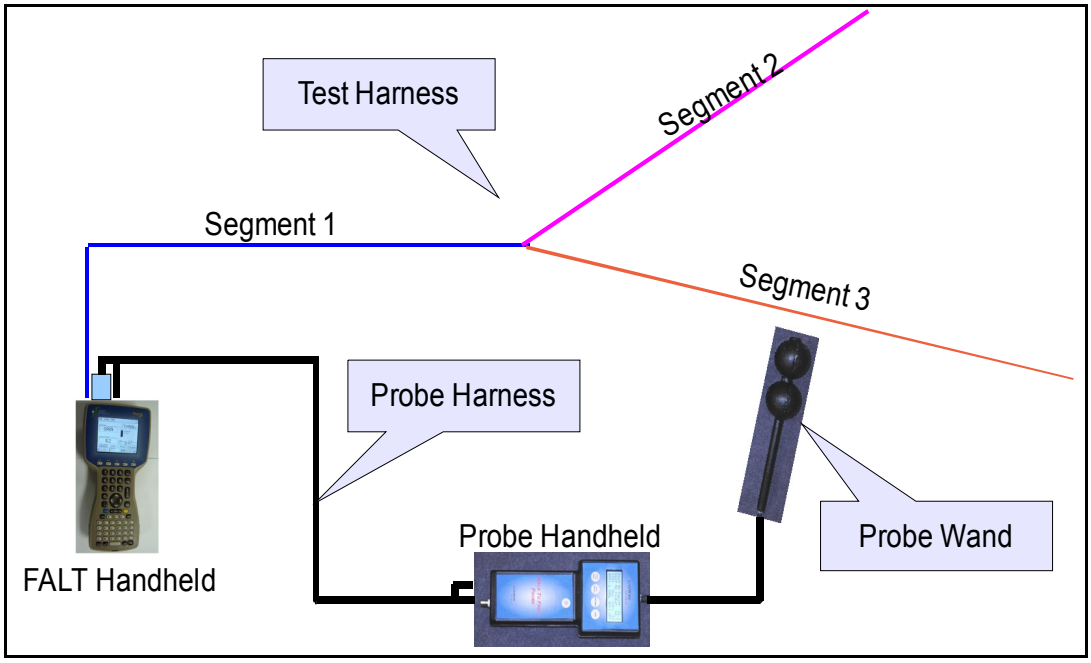

Figure 3: An overview of the hardware connections

2.2.2 Electric and Magnetic Field Antennas

After a test has been collected on a certain wire and the distance to a fault has been found, a second testing device, known as the probe, is used to sense the transmitted signal in the form of electric and magnetic fields surrounding the wire, in an effort to guide the user to the fault location.

The EM probe used for collecting data is an electro-magnetic sensor array that works in conjunction with the handheld S/SSTDR reflectometer. The handheld places a sine wave modulated PN code (SSTDR) on the wire under test. Electric and magnetic fields are generated as the test wire is energized [8]. These fields, or waves, exist around and between the wire conductor and its reference when the wire is energized with the SSTDR signal.

The EM probe is made up of electric (dipole) and magnetic (small-loop) receiving antenna arrays designed to sense the waves radiating from the wire. The antenna arrays are optimized to pick up the PN codes transmitted on the wires. Parameters that will affect the accuracy/effectiveness of this system are the amount of power picked up by the antennas, and the bandwidth of that pick up. The amount of power is affected by the type of antenna (which also affects whether it is receiving E or H fields), efficiency of the antenna, distance from the wire, and polarization of the antennas relative to the wire. The waves picked up from the EM probe are filtered for the appropriate frequencies and are then transferred along a wire directly connected to the handheld, as shown in Figure 4. This received signal is correlated and processed to determine how far down the wire from the handheld the EM probe is located. This distance is then communicated back to the EM probe, where it is displayed. The maintainer can scan the wires to reach the fault or desired location.

Multiple antennas are used to overcome several issues in the collection of relevant signals. One issue is that a single small loop antenna picks up only the magnetic fields that are orthogonal to it and that cross its cross sectional surface [12]. From the perspective of the source, magnetic fields travel around a conductor orthogonal to the flow of electrons, in a clockwise direction. Only those magnetic fields that pass through the loop of the antenna are sensed. The best reception of magnetic fields can occur if the antenna is rotated so that its loop exists on a plane that includes the line of the conductor. This is an inconvenience if the direction of the test wire is obscured. To resolve the problem, the probe employs two small loop antennas that occupy the same space, but at perpendicular position. This allows the antenna probe to receive all polarizations of

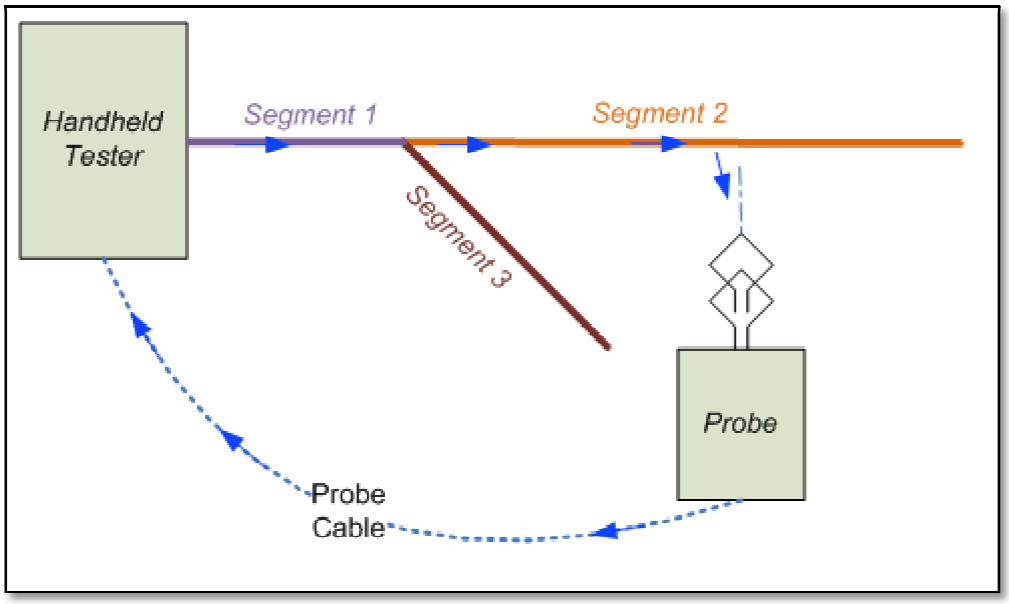

Figure 4: Most direct path of the test signal.

magnetic field, and the user no longer needs to be concerned about the rotational orientation of the probe loop antennas.

When electric current is flowing along the wire, a magnetic field is produced outside of that wire (unless the wire is shielded). A magnetic field pick up antenna is used to receive this signal for analysis. In some cases, such as at the end of the wire, or at an open circuit fault, the net current flow is zero because of the overlapping reflections, and the magnetic fields are close to zero. For these cases when the magnetic fields are low the electric fields are generally high. Hence an electric field pick up antenna is included as a substitute.

2.3 Inversion Theory

2.3.1 The Generic Inversion Model

The main algorithmic tool used in the proposed method is described by inversion theory. Inversion theory is the method and practice of deriving a model from data collected about that model. A classic example is to develop a three-dimensional estimate (the model of desired attributes) of an underground oil reserve (the physical occurrence) from seismic vibrations recorded (the collected data) while blasting charges into the ground [13]. In the case of this thesis, a model of the separated traveling waveforms is derived using data collected from sensing and correlating the fields surrounding a bundle of wires. Analysis of an accurate model can then be used to create an estimate of the locations of major impedance changes within the bundle, and from that, an understanding of the topology of the wire bundle can be derived.

An understanding of the forward equation is used to develop the inverse equation. In the case of this thesis, the ideal forward operation only exists academically, because the model is not measurable. In basic form, a forward operation consists of these basic elements:

$$\mathbf{A}(\mathbf{m}_{ideal}) = \mathbf{d}_{calc} \qquad \textbf{Equation 2}$$

where $\mathbf{m}_{ideal}$ is an ideal forward and backward waveform, A is the generic forward operator performed upon the waveforms of the model to create data points, and $\mathbf{d}_{calc}$ is the resultant data based on the model $\mathbf{m}_{ideal}$**.** By operating on an ideal model, the forward operation provides ideal data. In the real world, the model is not measurable. We

must collect data in order to arrive at an accurate estimation of the model, therefore we apply the principles of inversion theory.

Inversion is the art of determining or estimating the model parameters from the collected data. Whatever operation is applied in the forward equation must be inversely applied in the inverse equation:

$$\mathbf{A^{-1}}(\mathbf{d}_{meas}) = \mathbf{m} \qquad \textbf{Equation 3}$$

where the model $\mathbf{m}$ is a matrix of values comprising a model of the forward and backward traveling waveforms, $\mathbf{d}_{meas}$ is the convolved SSTDR data collected by the hardware, and $\mathbf{A}^{-1}$ is the inverse of the forward operator.

In the field of wiring integrity analysis, the measured data $\mathbf{d}_{meas}$ is collected and derived using the SSTDR reflectometry methods described in this paper. Each row of data represents one "snapshot" sampling at a particular probe position. The model $\mathbf{m}$ represents a set of two vectors, called forward and backward waveforms, separated from each other and filtered by the direction the EM field was traveling at the time it was sensed by the EM probe. In this thesis $\mathbf{A}^{-1}$ represents the summation of the data elements, or pieces of information that are caused by similarly traveling SSTDR waveform components, with the application of offsets to the data collected to adjust for the location at which it was collected.

The inversion will take a matrix of measured data points as inputs and provide an estimated wave model as an output.

2.3.2 Derivation of the Steepest Descent Method

In the generic case presented in section 2.3.1, the inversion problem can be solved directly if the operator **A** is assumed to be linear and data are presented without noise. However, in the case of reflectometry data obtained from testing wires on live aircraft, the operator cannot be assumed to be linear, and noise will definitely be present. Therefore the solution is best found iteratively. One of the most widely used techniques for optimization is the steepest descent method, a particular variation of gradient-type methods [13].

The goal of the steepest descent method is to minimize the difference between the calculated and measured data without noise, called the misfit functional, by "descending" along the steepest path towards that minimum. That is, to minimize the misfit $\phi(\mathbf{m})$ between measured data and data derived from a particular assumed model $\mathbf{m}$.

$$\boldsymbol{\phi}(\mathbf{m})_{\mathbf{D}} = \boldsymbol{\mu}^{\mathbf{2}} \left(\mathbf{A}(\mathbf{m}_{\mathbf{M}}), \mathbf{d}\right)_{\mathbf{D}} \qquad \textbf{Equation 4}$$

where $\mathbf{d}$ is measured data $\mathbf{d}_{meas}$ (name changed for simplicity), D denotes the dimensional space of the data , and μ^2 is the squared norm of the misfit. See Equation 24 for an example of the dimensional space of D. The misfit is dimensionally the same as the data, and can be said to occupy the same metric space D. This is denoted in order to differentiate from the dimensional space, M, of the model, $\mathbf{m}$, as seen in Equation 26. M space is a matrix comprised of two rows that describe forward and backward travel. The metric spaces D and M are generally not denoted throughout the rest of the derivation, but appear when clarity is needed.

The misfit can also be described as

$$\boldsymbol{\phi(\mathbf{m})_D = \|\mathbf{A}(\mathbf{m}) - \mathbf{d}\|^2 = (\mathbf{A}(\mathbf{m}) - \mathbf{d}, \mathbf{A}(\mathbf{m}) - \mathbf{d})_D} \qquad \textbf{Equation 5}$$

A descent condition is imposed by a descent method that states that the next iteration (n+1) should be closer to the minimum than the last iteration, n.

$$\boldsymbol{\phi(\mathbf{m}_{n+1}) < \phi(\mathbf{m}_n) \text{ for all } n \geq 0} \qquad \textbf{Equation 6}$$

To find a subset of models at each iteration $\{\mathbf{m}_n\}$ which satisfy this descent condition and also minimize the misfit functional within the least number of iterations possible, we calculate the derivative, or first variation, of the misfit functional for the model $\mathbf{m}$:

$$\boldsymbol{\delta(\mathbf{A}(\mathbf{m}) - \mathbf{d}, \mathbf{A}(\mathbf{m}) - \mathbf{d}) = 2(\delta\mathbf{A}(\mathbf{m}), \mathbf{A}(\mathbf{m}) - \mathbf{d})} \qquad \textbf{Equation 7}$$

where δ represents the derivative with respect to time. Using the result of Equation 7, we work to solve for the change to the model, $\delta\mathbf{m}$. As a necessary step to this end, we assume the operator $\mathbf{A}$ is nonlinear, but also differentiable, so the Frechet [13] derivative $\mathbf{F_m}$ of $\mathbf{A}$ can be used:

$$\boldsymbol{\delta A(\mathbf{m}) = \mathbf{F_m}\delta\mathbf{m}} \qquad \textbf{Equation 8}$$

By substituting Equation 8 into Equation 7 we obtain

$$\boldsymbol{\delta\phi(\mathbf{m}) = 2(\mathbf{F_m}\delta\mathbf{m}, \mathbf{A(m)} - \mathbf{d})} \qquad \textbf{Equation 9}$$

This can be further simplified using the properties of the adjoint operator, $\mathbf{F_m^*}$, of the Frechet derivative. The adjoint operator makes it possible to move a linear operator of $\mathbf{F_m}$ from the left to the right hand side of the inner product in Equation 9. [13]

$$\boldsymbol{\delta\phi(\mathbf{m}) = 2(\delta\mathbf{m}, \mathbf{F_m^*(A(m)} - \mathbf{d}))} \qquad \textbf{Equation 10}$$

In practice, the adjoint operator is the key to relating points from data space, D, to model space, M.

A practical way to describe the descent condition (Equation 6) is in terms of the directions and magnitudes in which to make changes to the model, $\delta\mathbf{m}$. This is described by

$$\boldsymbol{\delta(\mathbf{m}) = -k\mathbf{L(m)_M}} \qquad \textbf{Equation 11}$$

where k, a positive real number, represents the magnitude, or step size of the proposed error correction, and $\mathbf{L(m)}_{\mathrm{M}}$ is a matrix of vectors in model space, representing the worst direction possible for convergence, or direction of ascent. A simple yet effective method for converging on the minimal misfit is using the opposite of the optimal direction of ascent, or the direction of descent. Thus the method employed is called the steepest descent method. [13] Therefore, Equation 11 is inverted so that the direction of steepest ascent:

$$\mathbf{L(m) = F_m^*(A(m)} - \mathbf{d}) \qquad \textbf{Equation 12}$$

becomes the assumed direction of steepest descent when inverted.

By substituting Equation 11 and Equation 12 into Equation 10 we have

$$\boldsymbol{\delta\phi(\mathbf{m}) = -2k(\mathbf{L(m)}, \mathbf{L(m)}) < 0} \qquad \textbf{Equation 13}$$

With the basic elements of the steepest descent iteration process defined, the iteration can be summarized as follows:

When describing single iterations, the misfit functional is described using a single variable, **r**, so that

$$\mathbf{r_n = (A(m_n) - d)} \qquad \textbf{Equation 14}$$

where $\mathbf{r}_n$ is the misfit and $\mathbf{m}_n$ is the model for the *n*th iteration. Therefore, substituting Equation 14 into Equation 12, we arrive at the direction of steepest ascent $\mathbf{L}_n$:

$$\mathbf{L_n = L(m_n) = F^*_{m_n} r_n} \qquad \textbf{Equation 15}$$

Several methods can be used for selecting the step length of the nth iteration, k_n. For brevity, this thesis will assume that k_n is selected using the line search method, where

$$\boldsymbol{k_n = \frac{\|\mathbf{L}_n\|^2}{\|\mathbf{g}_n\|^2}} \qquad \textbf{Equation 16}$$

and

$$\mathbf{g_n = -F_{m_n} L_n} \qquad \textbf{Equation 17}$$

where $\mathbf{g}_n$ is an intermediate step used for calculating the step size k_n.

We can now construct the adjustment amount to be applied to the model at the particular iteration:

$$\boldsymbol{\phi}(\mathbf{m}_{n+1}) = \mathbf{m}_n - \boldsymbol{k}_n \mathbf{L}_n \qquad \textbf{Equation 18}$$

Iterations using Equation 18 will continually minimize the misfit functional, satisfying Equation 4 when the normalized misfit reaches a given acceptable error level ε_0,

$$\boldsymbol{\phi}(\mathbf{m}_N) = \|\mathbf{r}_N\|^2 \leq \boldsymbol{\varepsilon_0} \qquad \textbf{Equation 19}$$

2.4 Example Configurations

A test suite consists of performing multiple tests while incrementally scanning the test wire in the fashion shown in Figure 5. Testing is avoided within 6 inches of the branch, as this can produce unreliable results. During the initial scan, each test position is approximately 8 inches apart, but this distance may be adjusted on shorter segments so that a minimum of 8 tests are performed on each segment.

The resolution of data collected by the probe is impacted by the following factors: number of data points collected, different positions along the wire, branches in the wires, distance of the probe from the wire, frequency spectrum used for the test, type of probe used, and likely a number of other factors. However, there are a number of factors that can be directly analyzed to provide insights as to the resolution of the probe system.

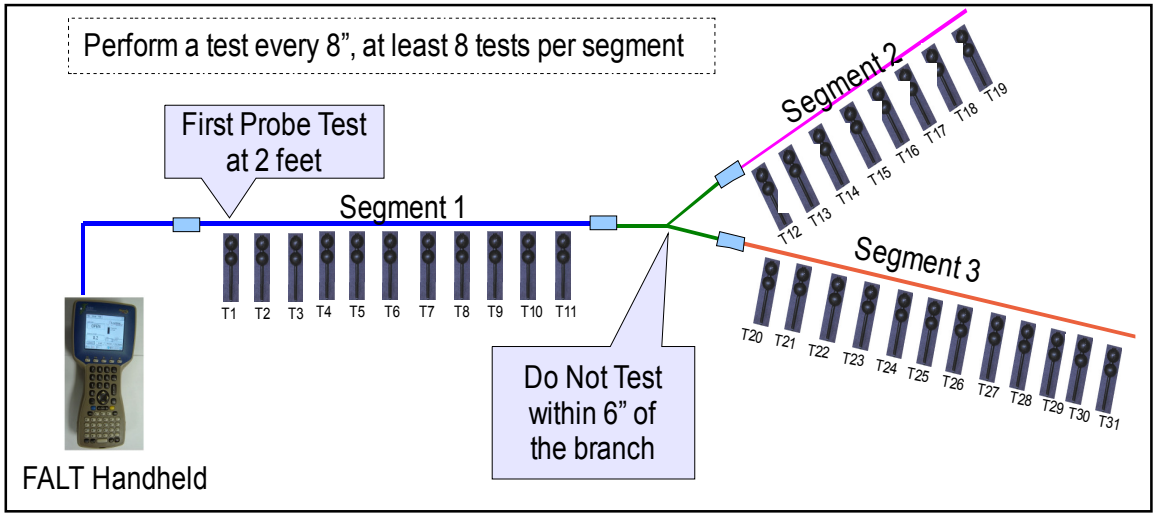

Figure 5: Basic method for testing a branched network with an EM probe.

Based on preliminary data collected using the probe it seems reasonable that the location of the probe can be found to within 1/10 the wavelength of the highest frequency observed with significant amplitude in the sensed signal. In practice, noise observed in the collected data may distort the waveform and suppress the ability to pick out the phase of the primary reflection from the end of the wire.

Preliminary data show that high frequencies die off along the length of the wire, so it stands to reason that the ability to pinpoint the location of the probe will decrease as the sensor is moved further along the length of the cable. Reasonable wire lengths are estimated to be between 5–100 feet, although longer cables may be feasible.

With an SSTDR system, the injected spectrum of the spread spectrum signal is not flat, but rather is bound by an overlapped sync function due to spectral aliasing that emphasizes the low frequencies. The signal introduced to the wire is essentially a square

wave summed with a sin wave carrier, causing a digital zero to produce a positive sin wave, and a digital one to produce an inverted sin wave. This is the carrier on which the PN code is delivered to the wire.

The collected data provide information that will aid in the development of the probe front-end to preserve the high frequency content that provides precision, while keeping the low-frequency content present that helps filter out noise and false observations.

As the probe is moved farther from the cable, the signal is observed from a broader range of wire and the resolution will be clouded and the lower limit of resolution with an omnidirectional probe will be on the order of the distance of the probe from the wire. Sample data also show the expected decrease in signal amplitude that will also cause background noise to corrupt the system's ability to locate the center of the incident and reflected data peaks.

Another observation is that at the end of the wire, the observed current approaches zero for an open circuit due to the destructive interference of forward and reverse traveling waves, so the electric probe will provide better resolution near the end of the wire than the magnetic field probe. The actual resolution will depend on the test environment, since the electric field probe is highly affected by coupled fields to adjacent wires.

Since the probe senses fields as they pass along the wire and does not need to wait for the reflection, the initial observation time is equal to the time of flight of the signal to the observation point. Unlike a reflection where the signal is observed as it passes down and back along the wire, the signal observed by the probe only passes once along the wire

before it is first observed. Thus, the expected resolution of the probe under normal circumstances for 144 MHz is approximately

$$\boldsymbol{Resolution \approx \frac{c(VOP)}{10(144\ MHz)} = 0.4ft} \qquad \textbf{Equation 20}$$

where c is the speed of light, and VOP is the velocity of propagation for the given wire under test.

Resolution is defined as the greatest amount of positive or negative error due to the granularity of the measurement. The actual resolution will depend on background reflection noise, high frequency loss, the distance away from the wire that the probe is held, and other factors. Under normal conditions, it is predicted that the location of the sensor relative to the signal source can be pinpointed with a resolution of 1/10 the length of 1 bit of the PN code, which translates to ±0.4 feet at 144 MHz.

Many wiring networks within aircraft are known to contain a single branch, such as those that split to run down each wing of the plane. As wiring networks contain more branches, the ability to map that network becomes increasingly difficult. The scope of this thesis allows for testing of simple single-branched networks, but more complicated branched networks will just be simulated (rather than measured) to determine the limits of the algorithm.

2.5 Specifications of the Final System

Accounting for noise, interference, and calculation error, a resolution of +/- 1.5 foot is set as an acceptable accuracy for finding the distance to the field sensor using a generated signal at 144 MHz. Using the proposed algorithm for modeling the backward

traveling waves, the distance to the nearest reflection point is expected to be discoverable with a resolution of +/- 2 feet.

CHAPTER 3

METHODS

3.1 Dividing the Waveform Model into Forward and Backward

The technical objective of this project was to devise a method for calculating the location in distance of major reflection points on the type of wire bundles where standard reflectometry fails, such as with branched wiring. From the research performed to understand the electro-magnetic properties of a conductor in relation to the field probe, it was found that one of the best indicators of major reflection points is the wave that is traveling back from a reflection point. Because the probe is referenced to free space, it will detect the full positive return wave, no matter the termination on the wire.

An accurate representation of a real-world model is often created from a large number of complex variables and influences. For this reason, specific characteristics of a particular model are singled out and separated or accentuated in order to limit the complexity of the model.

It is possible to model several different attributes of a signal on a wire, in both the frequency and time domains. The model derived in this research is based on the position of reflection points in relation to a moving sensor, as seen in the time domain. By taking snap shots of the behavior of the EM waveforms at multiple locations, the direction of

travel of the reflection points in relation to the sensor can be determined. As the sensor is moved away from the signal source to the right, as shown in Figure 6, EM signals traveling from left to right on a time scale are described as forward traveling waves. Signals traveling from right to left on a time scale are described as backward traveling waves. When these traveling waves are correlated and analyzed, they make up the sets of data. When the data are processed to separate the information from forward and backward signals, forward and backward traveling waveforms are created. The signature peaks in these waveforms provide information about the topology of the wire network topology.

Understanding the direction of travel of a reflection point leads to an understanding of whether that particular reflection point lies between the sensor and the source, on a different branch, or further down the wire being scanned. The direction of travel can be determined by collecting data from multiple points of observation.

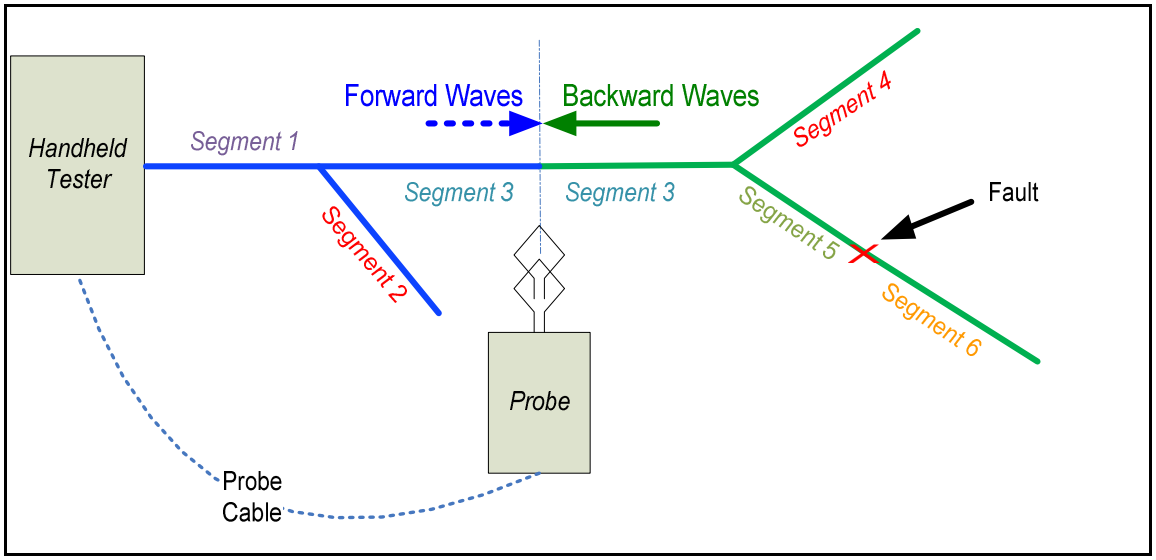

Figure 6: Representation of the test wire and classification of the waves detected at the point of the sensor.

The waveforms caused by reflection points, whether they are traveling forward or backward, have a tendency to overlap. Overlapping waveforms can cause distorted or indistinguishable features to appear, making the use of simple wave detection algorithms unreliable.

The progression of thought brings one to some type of peeling algorithm, in which waveforms are subtracted one at a time from the total. Simple applications using this approach can have success, but become unreliable when noise is introduced to the signal due to uncontrolled impedances, or due to the inability to reliably detect the location of the first wave to peel.

These issues have not been completely resolved, but can be greatly reduced using the methods and algorithm presented in this paper. Many overlapping waveforms are of forward and backward traveling waves. Using an algorithm to separate and model the waves traveling forward, F, and backward, B, the waveforms can be clearly represented to better allow a peak detect or waveform peeling algorithm to find the location of the reflectors.

3.2 The Algebraic Reconstruction Technique (ART)

The Algebraic Reconstruction Technique (ART) algorithm is a method for deriving a model from multiple data sets collected at various points [10]. In simple implementation, the model can be of a specific traveling wave, such as a forward or backward traveling wave. As the sets of data are lined up correctly and combined, the waves that were lined up are amplified, and the waves that were not lined up are diminished.

As a sensor is moved further down the wire, it moves farther from the signal source, and closer to the reflector or end point. The ART technique is performed by shifting and adding multiple sets of data in a way so that a particular piece of information is emphasized while others are mitigated, as shown in Figure 7. The shift accounts for the distance covered by the moving reference of the field sensor. Similar to creating a 3-D image of a human brain using a CAT scanner, data gathered from multiple viewpoints are combined to produce a single comprehensive result.

Specific to sensing field-emitting wires, the offset is a direct conversion of the distance of the sensor from the source. This is true for both forward and backward traveling waves, simply because when moving away from the signal source, one moves that much closer to reflectors and endpoints off of which the wave reflected.

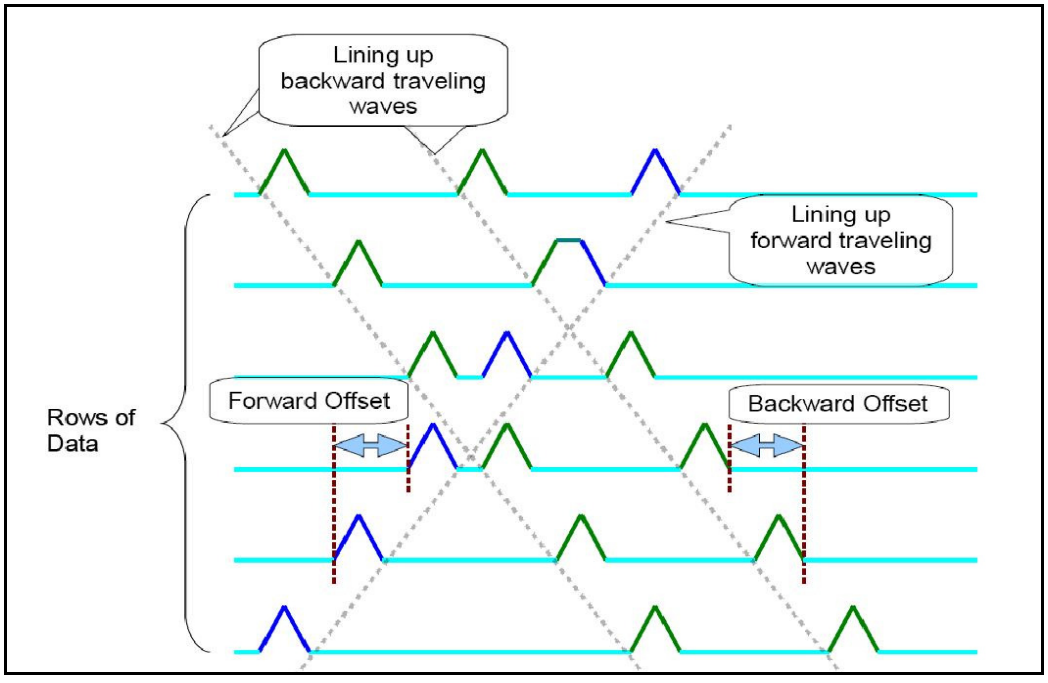

Figure 7: Drawing showing the methods used by the ART algorithm to align similar traveling waveforms using an offset.

3.3 Advantages of Using an Inversion Algorithm

The ART algorithm is a good method for emphasizing particular waveforms, but does not eliminate the other waves in a set of data. A twist on the ART algorithm provides several advantages when finding multiple elements of a model. If an inversion method is implemented on top of the ART algorithm, multiple parameters of the model can be resolved simultaneously and more accurately. Because waves are ear-marked for different parts of the model, if two waves traveling in opposite directions happen to fall on top of each other at some location of the sensor, each waveform can be extracted from the jumbled mix. The ability to separate the forward and backward traveling waves allows isolated analysis of the waves that first reflect off of the nearest reflectors down the cable, while ignoring those that have already passed by. Such isolation allows for a more reliable mapping of the separate segments of a wire, particularly when it includes branches and faults.

When searching for a particular traveling wave such as the backward wave, rather than dealing with a diminished or distorted forward waveform, the forward waveform is removed, allowing a clear analysis of the backward traveling waveform.

3.4 Application of Inversion to the Problem

This section is a description of a method for arriving at an accurate model of the network topology. The processes and equations presented in this section were developed by Paul Smith and Carl Brewer while employed at Livewire Test Labs.

The model of interest defines and separates the components of the forward and backward traveling waveforms. The model can then be described as:

$$\mathbf{m} = \mathbf{m}_{fb} \qquad \textbf{Equation 21}$$

where $\mathbf{m}_{fb}$ is the desired model, made up of forward and backward waveforms. The model is then refined over *n* iterations:

$$\mathbf{m}_n = \mathbf{m}_{fb_n} \qquad \textbf{Equation 22}$$

where $\mathbf{m}_{fb_n}$ refers to the *nth* iteration of the entire model, which is specifically consisting of both the forward and backward vectors.

This section describes the implementation of the algorithm with specific attention to defining the matrices and operators. As described in section 2.3.1, the forward model is given by $\mathbf{A}(\mathbf{m}) = \mathbf{d}$, where $\mathbf{m}$ is the model, $\mathbf{A}$ is an operator that operates on the model, and $\mathbf{d}$ is the calculated data produced based on the given model.

Data are traditionally organized in rows and columns,

$$\mathbf{d} = \begin{bmatrix} \boldsymbol{d_{1,1}} & \boldsymbol{d_{1,2}} & \cdots & \boldsymbol{d_{1,Drows}} \\ \boldsymbol{d_{2,1}} & \boldsymbol{d_{2,2}} & \cdots & \boldsymbol{d_{2,Drows}} \\ \vdots & \vdots & \ddots & \vdots \\ \boldsymbol{d_{Dcols,1}} & \boldsymbol{d_{Dcols,2}} & \cdots & \boldsymbol{d_{Dcols,Drows}} \end{bmatrix} \qquad \textbf{Equation 23}$$

where rows and columns within $\mathbf{d}$ are indicated with subscripts, respectively, and the variables $Drows$ and $Dcols$ are the respective maximum number of rows or columns of the dataset. In practice, each row represents a separate SSTDR probe test performed at a slightly different location along the wire. Therefore each data row provides a slightly different point of view of the system.

For the sake of the implementation of the algorithm, rows of the data are stood on end, effectively creating one long column of data, $\hat{\mathbf{d}}$.

$$\hat{\mathbf{d}} = \begin{bmatrix} \begin{bmatrix} \boldsymbol{d_{1,1}} \\ \boldsymbol{d_{1,2}} \\ \vdots \\ \boldsymbol{d_{1,Drows}} \end{bmatrix}_{\mathbf{1}} \\ \begin{bmatrix} \boldsymbol{d_{2,1}} \\ \boldsymbol{d_{2,2}} \\ \vdots \\ \boldsymbol{d_{2,Drows}} \end{bmatrix}_{\mathbf{2}} \\ \vdots \\ \begin{bmatrix} \boldsymbol{d_{Dcols,1}} \\ \boldsymbol{d_{Dcols,2}} \\ \vdots \\ \boldsymbol{d_{Dcols,Drows}} \end{bmatrix}_{\boldsymbol{Dcols}} \end{bmatrix} \qquad \textbf{Equation 24}$$

Individual data points are still identified with the original row and column indications. The model is broken into two pieces, and each submodel contains parameters that are broken into groups, as described in section 3.

$$\mathbf{m}_{\boldsymbol{fb_n}} = \begin{bmatrix} \mathbf{m}_{\boldsymbol{f}} \\ \mathbf{m}_{\boldsymbol{b}} \end{bmatrix}_{\boldsymbol{n}} \qquad \textbf{Equation 25}$$

where,

$\mathbf{m}_{fb_n}$ Entire model which includes both traveling waveforms at a particular iteration n of the steepest descent process.

$\mathbf{m}_f$ Forward traveling waveform model. The length of both model vectors is described as $Mcols$ and must be greater than the number of data columns, $Dcols\#$.

$\mathbf{m}_b$ Backward traveling waveform model.

To make the formation of the model and its components clear, the model $\mathbf{m}$ is further classified as,

$$\mathbf{m}_{fb} = \begin{bmatrix} \boldsymbol{m}_{f_1} & \boldsymbol{m}_{f_2} & \dots & \boldsymbol{m}_{f_{Mcols}} \\ \boldsymbol{m}_{b_1} & \boldsymbol{m}_{b_2} & \dots & \boldsymbol{m}_{b_{Mcols}} \end{bmatrix} \qquad \textbf{Equation 26}$$

where each element of $\mathbf{m}_{fb}$ is represented and the number of columns in the model is defined as $Mcols$.

The forward operation is defined by:

$$\mathbf{A}(\mathbf{m}_{fb}) = \begin{bmatrix} \begin{bmatrix} \boldsymbol{m}_{f_1} + \boldsymbol{m}_{b_1} \\ \boldsymbol{m}_{f_1} + \boldsymbol{m}_{b_2} \\ \vdots \\ \boldsymbol{m}_{f_1} + \boldsymbol{m}_{b_{Dcols}} \end{bmatrix}_{\mathbf{1}} \\ \begin{bmatrix} \boldsymbol{m}_{f_2} + \boldsymbol{m}_{b_1} \\ \boldsymbol{m}_{f_2} + \boldsymbol{m}_{b_2} \\ \vdots \\ \boldsymbol{m}_{f_2} + \boldsymbol{m}_{b_{Dcols}} \end{bmatrix}_{\mathbf{2}} \\ \vdots \\ \begin{bmatrix} \boldsymbol{m}_{f_{Drows}} + \boldsymbol{m}_{b_1} \\ \boldsymbol{m}_{f_{Drows}} + \boldsymbol{m}_{b_2} \\ \vdots \\ \boldsymbol{m}_{f_{Drows}} + \boldsymbol{m}_{b_{Dcols}} \end{bmatrix}_{\boldsymbol{Dcols}} \end{bmatrix} \qquad \textbf{Equation 27}$$

In order to update the model we need the Frechet derivative $\mathbf{F_m}$ of the forward operation, **A** [13]. The two waveform models, forward and backward, of the Frechet derivative used in calculations are $\mathbf{F}_{\mathbf{m}_f}$ and $\mathbf{F}_{\mathbf{m}_b}$, respectively, which when combined is defined as $\mathbf{F}_{\mathbf{m}_{fb}}$. For simplicity in this discussion, a generic $\mathbf{F_m}$ will be used to represent each piece, with the details clarified as individual fields are filled in. The Frechet derivative is a matrix given by:

$$\mathbf{F_m} = \begin{bmatrix} \frac{\partial A(\mathbf{m})_{1,1}}{\partial m_1} & \frac{\partial A(\mathbf{m})_{1,2}}{\partial m_2} & \cdots & \frac{\partial A(\mathbf{m})_{1,Dcols}}{\partial m_{Mcols}} \\ \frac{\partial A(\mathbf{m})_{2,1}}{\partial m_1} & \frac{\partial A(\mathbf{m})_{2,2}}{\partial m_2} & \cdots & \frac{\partial A(\mathbf{m})_{2,Dcols}}{\partial m_{Mcols}} \\ \vdots & \vdots & \ddots & \vdots \\ \frac{\partial A(\mathbf{m})_{Drows,1}}{\partial m_1} & \frac{\partial A(\mathbf{m})_{Drows,2}}{\partial m_2} & \cdots & \frac{\partial A(\mathbf{m})_{Drows,Dcols}}{\partial m_{Mcols}} \end{bmatrix} \qquad \textbf{Equation 28}$$

Following the required elements for the steepest descent method, as derived in section 2.3.2, the formula requires the complex-conjugate transpose, $\mathbf{F_m^*}$. Since all terms are real, this is just the transpose of the matrix $\mathbf{F_m}$,

$$\mathbf{F_m^*} = \begin{bmatrix} \frac{\partial A(\mathbf{m})_{1,1}}{\partial m_1} & \frac{\partial A(\mathbf{m})_{2,1}}{\partial m_1} & \cdots & \frac{\partial A(\mathbf{m})_{1,Dcols}}{\partial m_1} \\ \frac{\partial A(\mathbf{m})_{1,2}}{\partial m_2} & \frac{\partial A(\mathbf{m})_{2,2}}{\partial m_2} & \cdots & \frac{\partial A(\mathbf{m})_{2,Dcols}}{\partial m_2} \\ \vdots & \vdots & \ddots & \vdots \\ \frac{\partial A(\mathbf{m})_{1,Dcols}}{\partial m_{Mcols}} & \frac{\partial A(\mathbf{m})_{2,Dcols}}{\partial m_{Mcols}} & \cdots & \frac{\partial A(\mathbf{m})_{Drows,Dcols}}{\partial m_{Mcols}} \end{bmatrix} \qquad \textbf{Equation 29}$$

with each term evaluated at $\mathbf{m}$.

The complex-conjugate transpose is used to determine the steepest *ascent*, $\mathbf{L_m}$. This is a vector in the direction opposite the direction we want to modify our model, and will be negated later on to arrive at the direction of steepest descent,

$$\mathbf{F_m^* r} = \mathbf{L_m} = \begin{bmatrix} \sum_{Drows} \sum_{Dcols} \left(\frac{\partial A(\mathbf{m})_{Drows,Dcols}}{\partial m_1} \right) \mathbf{r}_{Drows,Dcols} \\ \sum_{Drows} \sum_{Dcols} \left(\frac{\partial A(\mathbf{m})_{Drows,Dcols}}{\partial m_2} \right) \mathbf{r}_{Drows,Dcols} \\ \vdots \\ \sum_{Drows} \sum_{Dcols} \left(\frac{\partial A(\mathbf{m})_{Drows,Dcols}}{\partial m_{Mcols}} \right) \mathbf{r}_{Drows,Dcols} \end{bmatrix} \qquad \textbf{Equation 30}$$

In an effort to relate to the subdivided model, the steepest ascent $\mathbf{L_m}$ is further partitioned into forward and backward sections,

$$\mathbf{L}_{\mathbf{m}_{fb}} = \begin{bmatrix} \mathbf{L}_f \\ \mathbf{L}_b \end{bmatrix} \qquad \textbf{Equation 31}$$

where $\mathbf{L}_{\mathbf{m}_{fb}}$ is the steepest ascent described in terms of the forward and backward elements.

In the following equations, indices, known to programmers as pointers, are used to represent various values within arrays and matrices. This method is used to describe the shifting or 'traveling' of the waveforms as a function of rows. Relationships between the pointed to values are the essential make up of the inversion operator. In other words, the amount of shifting that occurs between rows of collected data is the key element for deriving the various sections of the model.

To this end, for the following discussion it is important to distinguish between the arbitrary indexes icol and irow, which are used generically to iterate over summations, and indexes denoted with a subset-variable *f* or *b*, which relate to specific values in sub-vectors of the matrix. A similar nomenclature is used for each subsection.

For example, consider $\mathbf{L}_f$ for which Fcol_j is used to represent a specific index Fcol into $\mathbf{L}_f$. Thus,

$$\boldsymbol{\partial}\left(\mathbf{Fcol}_j - \mathbf{Fcol}\right) = \begin{vmatrix} \mathbf{1}, \mathbf{Fcol}_j = \mathbf{Fcol} \\ \mathbf{0}, \mathbf{Fcol}_j \neq \mathbf{Fcol} \end{vmatrix} \qquad \textbf{Equation 32}$$

means that the partial derivative is nonzero when the constant value Fcol_f is equal to a value within the vector Fcol. In other words, Fcol will be swept across a range of values, while Fcol_j remains constant. Similarly Bcol_b is used to represent a specific index Bcol into $\mathbf{L}_b$. These indexes are not to be confused with Dcol_f , which is the specific Dcol

index into the raw data estimate $\mathbf{d}$ that is a contributing element to the forward traveling waveform array $\mathbf{m}_f$ as shown in Equation 28.

As described in Equation 27, Fcol and its subscripted versions refer to the correct index into $\mathbf{L}_f$ associated with an offset Mcol. Thus, $\mathbf{L}_f$ ranges from 1 to *#Mcols*, and Fcol ranges from 1 to *#Fcols*, which is always greater than *#Mcols*.

Therefore, using Equation 32 to solve each element within $\mathbf{L}_f$,

$$\frac{\partial \mathbf{A}(\mathbf{m})_{(\mathbf{Drow},\mathbf{Dcol})}}{\partial \mathbf{L}_{(f,\mathbf{Fcol}_j)}} = \frac{\partial (\mathbf{L}_{(f,\mathbf{Fcol})} + \mathbf{L}_{(b,\mathbf{Bcol})})}{\partial \mathbf{L}_{(f,\mathbf{Fcol}_j)}} = \boldsymbol{\delta}(\mathbf{Fcol}_j - \mathbf{Fcol}) \qquad \textbf{Equation 33}$$

where

$$\partial \mathbf{L}_{(f,\mathbf{Fcol}_j)} = \sum_{\mathbf{Drow}} \sum_{\mathbf{Dcol}} \boldsymbol{\delta}(\mathbf{Fcol}_j - \mathbf{Fcol})\, \mathbf{r}_{\mathbf{Drow},\mathbf{Dcol}} = \sum_{\mathbf{Drow}} \mathbf{r}_{\mathbf{Drow},\mathbf{Dcol}_f} \qquad \textbf{Equation 34}$$

and

$$\mathbf{Dcol}_f = \mathbf{Fcol}_f - \mathbf{S}_{Drow} \qquad \textbf{Equation 35}$$

where S_{Drow} is a given offset value for the particular row, and

$$\mathbf{r}_{\mathbf{Drow},\mathbf{Dcol}_f} = \mathbf{0} \qquad \textbf{Equation 36}$$

where $\mathbf{r}_{\mathrm{Drow,Dcol}_f}$ is the misfit for the particular row and column of interest, which is outside the bounds where

$$\mathbf{1} \leq \mathbf{Dcol}_f \leq \#\boldsymbol{Dcols} \qquad \textbf{Equation 37}$$

where $\#Dcols$ is the number of data columns, or size of each data test.

Thus, only certain rows of data have column indices that can map to Fcol_f due to a given row offset S_{Drow}.

Finally, to find the model of the backward traveling waveform, $\mathbf{m}_b$, we use same set of equations used to find the forward model, $\mathbf{m}_f$. For solving each element within section $\mathbf{L}_b$,

$$\frac{\partial \mathbf{A}(\mathbf{m})_{(\mathbf{irow,icol})}}{\partial \mathbf{L}_{(b,\mathbf{Bcol}_j)}} = \frac{\partial (\mathbf{L}_{(f,\mathbf{Fcol})} + \mathbf{L}_{(b,\mathbf{Bcol})})}{\partial \mathbf{L}_{(b,\mathbf{Bcol}_j)}} = \boldsymbol{\delta}(\mathbf{Bcol}_j - \mathbf{Bcol}) \qquad \textbf{Equation 38}$$

where

$$\partial \mathbf{L}_{(b,\mathrm{Fcol}_j)} = \sum_{\mathrm{Drow}} \sum_{\mathrm{Dcol}} \delta(\mathrm{Bcol}_j - \mathrm{Bcol})\, \mathbf{r}_{\mathrm{Drow,Dcol}} = \sum_{\mathrm{Drow}} \mathbf{r}_{\mathrm{Drow,Dcol}_b} \qquad \textbf{Equation 39}$$

and

$$\mathbf{Dcol}_b = \mathbf{Bcol}_b - \mathbf{S}_{\boldsymbol{Drow}} + \#\boldsymbol{Dcols} - \#\boldsymbol{Bcols} \qquad \textbf{Equation 40}$$

and

$$\mathbf{r}_{\mathbf{Drow,Dcol}_b} = \mathbf{0} \qquad \textbf{Equation 41}$$

outside the bounds where

$$\mathbf{1} \leq \mathbf{Dcol}_{\boldsymbol{b}} \leq \#\boldsymbol{Dcols} \qquad \textbf{Equation 42}$$

Thus, only certain rows of data have column indices that can map to Bcol_b due to a given row offset, S_{Drow}.

Bringing the forward and backward vectors of $\mathbf{L}$ together:

$$\mathbf{L}_{\boldsymbol{fb_n}} = \begin{bmatrix} \begin{bmatrix} \mathbf{L}_{\boldsymbol{f_1}} \\ \mathbf{L}_{\boldsymbol{f_2}} \\ \vdots \\ \mathbf{L}_{\boldsymbol{f_{Fcols}}} \end{bmatrix} \\ \begin{bmatrix} \mathbf{L}_{\boldsymbol{b_1}} \\ \mathbf{L}_{\boldsymbol{b_2}} \\ \vdots \\ \mathbf{L}_{\boldsymbol{b_{Bcols}}} \end{bmatrix} \end{bmatrix} = \begin{bmatrix} \begin{bmatrix} \sum_{\#\boldsymbol{Drows}} \mathbf{r}_{\boldsymbol{Drow,1-S_{Drow}}} \\ \sum_{\#\boldsymbol{Drows}} \mathbf{r}_{\boldsymbol{Drow,2-S_{Drow}}} \\ \vdots \\ \sum_{\#\boldsymbol{Drows}} \mathbf{r}_{\boldsymbol{Drow,Fcols-S_{Drow}}} \end{bmatrix} \\ \begin{bmatrix} \sum_{\#\boldsymbol{Drows}} \mathbf{r}_{\boldsymbol{Drow,1+S_{Drow}+\#Dcols-\#Bcols}} \\ \sum_{\#\boldsymbol{Drows}} \mathbf{r}_{\boldsymbol{Drow,2+S_{Drow}+\#Dcols-\#Bcols}} \\ \vdots \\ \sum_{\#\boldsymbol{Drows}} \mathbf{r}_{\boldsymbol{Drow,Bcols+S_{Drow}+\#Dcols-\#Bcols}} \end{bmatrix} \end{bmatrix} \qquad \textbf{Equation 43}$$

With the steepest ascent defined, the next step is to calculate the optimal value of the scaling factor *k*, defined as the step size in which to move in the direction of the steepest descent. The following calculations are required for finding *k*.

$$\mathbf{g}_{\boldsymbol{fb_n}} = -\mathbf{F}_{\mathbf{m}_{\boldsymbol{fb_n}}} \mathbf{L}_{\boldsymbol{fb_n}} = \begin{bmatrix} \begin{bmatrix} \mathbf{g_1} \\ \mathbf{g_2} \\ \vdots \\ \mathbf{g}_{\boldsymbol{Dcols}} \end{bmatrix}_{\mathbf{1}} \\ \begin{bmatrix} \mathbf{g_1} \\ \mathbf{g_2} \\ \vdots \\ \mathbf{g}_{\boldsymbol{Dcols}} \end{bmatrix}_{\mathbf{2}} \\ \vdots \\ \begin{bmatrix} \mathbf{g_1} \\ \mathbf{g_2} \\ \vdots \\ \mathbf{g}_{\boldsymbol{Dcols}} \end{bmatrix}_{\boldsymbol{Drows}} \end{bmatrix} \qquad \textbf{Equation 44}$$

where $\mathbf{g}_{fb_n}$ is the *nth* iteration of the calculated step required for finding the proper step size. To find each element of $\mathbf{g}_{j_n}$,

$$\mathbf{g}_{j_n(Gcol,Grow)} = \sum_j \frac{\partial A(\mathbf{m})_{(Dcol,Drow)}}{\partial m_j} \mathbf{L}_j \qquad \textbf{Equation 45}$$

Taking the partial derivative reduces most of the equation to 1, leaving $\mathbf{L}_j$ as the component of importance for finding each point of $\mathbf{g}_{j_n}$.

$$\mathbf{g}_{fb_n(Gcol,Grow)} = \mathbf{L}_{f_{Fcol}} + \mathbf{L}_{b_{Bcol}} \qquad \textbf{Equation 46}$$

where $Gcol$ and $Grow$ represent the respective indices of column and row within $\mathbf{g}_{fb_n}$.

With $\mathbf{L}_{fb_n}$ and $\mathbf{g}_{fb_n}$ defined, the step-size constant k_{fb_n} can be calculated,

$$\boldsymbol{k_{fb_n}} = \frac{\left\|\mathbf{L}_{fb_n}\right\|^2}{\left\|\mathbf{g}_{fb_n}\right\|^2} \qquad \textbf{Equation 47}$$

where k_{fb_n} is the step-size in which to correct each element of the model to minimize the misfit, or in other words, to converge upon the best estimate of the model.

At this point, each variable of the steepest descent process is thoroughly defined as it applies to the problem. A new estimate of the model using the parameters is calculated,

$$\boldsymbol{\phi}\left(\mathbf{m}_{fb_{n+1}}\right) = \mathbf{m}_{fb_n} - \boldsymbol{k_{fb_n}}\mathbf{L}_{fb_n} \qquad \textbf{Equation 48}$$

The steepest descent method is applied to the model as summarized in . The equations in are a quick reference to the operations used to update the model for the forward and backward traveling waveforms, described as m_f and m_b (see section 3). For

the derivation of the steepest descent method utilized in this table, please see section 2.3.2. The iterative process described by Table 1 is repeated until the residual error, $\mathbf{r}_n$ is minimized,

$$\mathbf{r}_n \leq \boldsymbol{\varepsilon_0} \qquad \textbf{Equation 49}$$

where ε_0 is the acceptable error threshold. For practicality, another reason to exit the iteration process is if the change in the model $\delta\mathbf{m}$ from one iteration to the next becomes insignificant,

$$(\boldsymbol{\delta}\mathbf{m}_n - \boldsymbol{\delta}\mathbf{m}_{n+1}) \approx \mathbf{0} \qquad \textbf{Equation 50}$$

If this occurs before the error is minimized, the iteration process can be stopped with the assumption that further iterations will not significantly change the model and the error threshold is unreachable.

A full steepest descent process is performed each time a new row of data is collected (once the minimum amount of data is reached.) A model is created for each segment of a branched test wire, and with more data the model is better refined. When a new data set is introduced it is compared to the model for existing segments to determine if it belongs to that segment. It is either matched to an existing segment data set, or is used as the basis for a new segment.

3.5 Discerning Segment Endpoints

When the backward traveling waves have been isolated from the forward traveling waves, the first wave encountered by this algorithm will have been caused by

Table 1: Quick Guide to Steepest Descent Method for Forward and Backward Traveling Waveforms (*fb*).

1) $\mathbf{r}_n = \mathbf{A}(\mathbf{m}_{fb_n}) - \hat{\mathbf{d}}$

2) $\mathbf{L}_{fb_n} = \mathbf{F}^*_{\mathbf{m}_{fb_n}} \mathbf{r}_n$

3) $\mathbf{g}_{fb_n} = -\mathbf{F}_{\mathbf{m}_{fb_n}} \mathbf{L}_{fb_n}$

4) $k_{fb_n} = \frac{\left\|\mathbf{L}_{fb_n}\right\|^2}{\left\|\mathbf{g}_{fb_n}\right\|^2}$

5) $\phi\left(\mathbf{m}_{fb_{n+1}}\right) = \mathbf{m}_{fb_n} - k_{fb_n} \mathbf{L}_{fb_n}$

6) $n = n + 1$

the nearest reflection point that has not been passed. This is true because if a reflection point has been passed, or even a reflection from a wire whose branch point has been passed, the waves will immediately be considered forward traveling, and thus segregated. If data are combined from both sides of a reflector, the sudden switch of that reflector from traveling backward to forward will cause the model of that reflector to diminish. For this purpose, it is vital that the data collected from one side of a reflector not be analyzed with data collected from the other side of the same reflector.

While the discussed inversion algorithm is used to find the nearest reflection point that has not been passed, it is important to know when the EM probe is in the act of passing a reflection point. This knowledge can prevent estimation errors from propagating from one segment to the next.

By keeping a stored model of the separated waves, newly collected data can be compared to the calculated model. By monitoring the amount of distortion that a new set of data causes to the calculated model, we can find the point at which a particular reflector changes from causing backward traveling waves to causing forward traveling waves, or vice versa. This phenomenon will only occur when physically passing the reflector with the EM probe. In Figure 8, the EM probe is located just before a reflection point. This means the reflection point will still cause backward traveling waves. In Figure 9, the reflection point has been passed, and its reflection will suddenly be missing from the backward waveform, and become invisible to the EM probe. In application, the software uses the sudden absence of the reflected wave to recognize when it has passed from one segment into another. When this occurs, the first segment is finished being analyzed and analysis of the next segment begins.

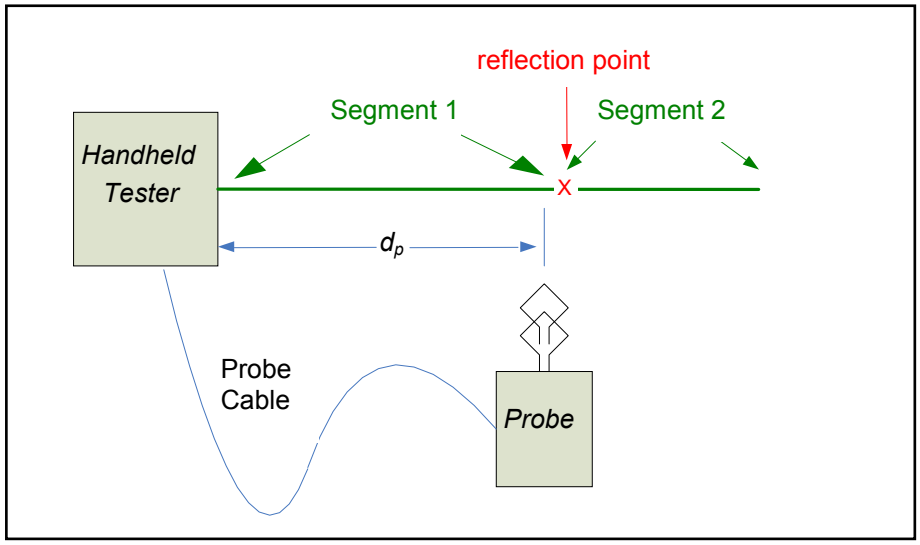

Figure 8: Representation of the EM probe just before passing a reflection point.

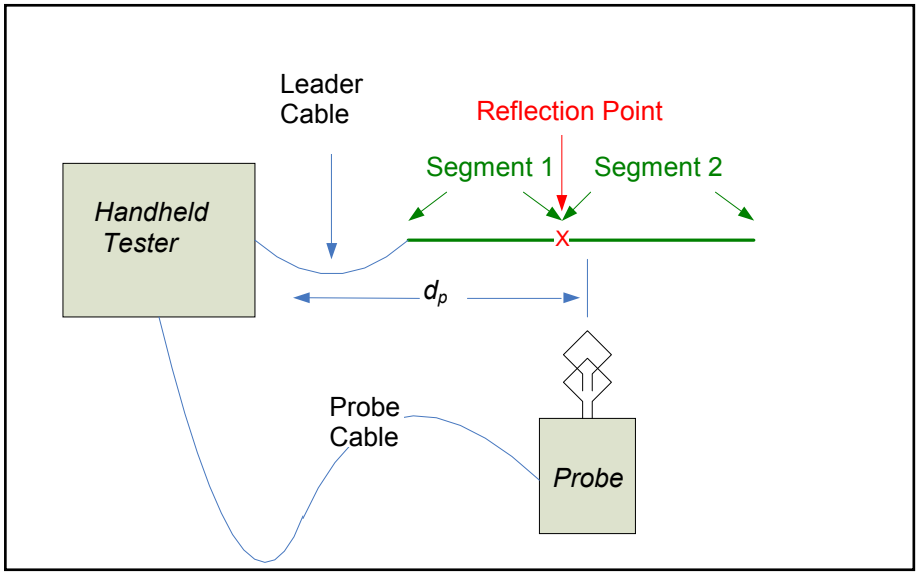

Figure 9: Representation of the EM probe just after passing a reflection point.

CHAPTER 4

RESULTS

4.1 Simulation

In order to understand the mechanics and ability of the proposed method, simulations were developed and performed using a variety of wave shapes. The simulations were run using perfect data at first, and then noise was increasingly injected to understand the limitations of the algorithm.

4.1.1 Pulse, Square, Triangle, SSTDR

Wave patterns were created (in software) to resemble the patterns created by testing a typical wire in ideal conditions. A wave pattern describes the waveform detected by the simulated EM probe as the probe is moved along a wire. Each row of data represents the samples collected at a single probe position. The simulated wave pattern consists of a single forward traveling incident wave and two backward traveling waves. These could correspond to waves created by a branch or an endpoint in the test wire. A variety of wave shapes were applied to the total wave pattern. These simulated tests help to determine and differentiate the causes of errors; whether they are inherent to the core algorithm, caused by other software shortcomings, or otherwise waveform dependant. The pulse wave pattern is simulated in Figure 10, with separated models of each segment shown in Figure 11 and Figure 12. The square wave pattern is simulated in Figure 13,

with separated models of each segment shown in Figure 14 and Figure 15. The triangle wave pattern is simulated in Figure 16, with separated models of each segment shown in Figure 17 and Figure 18. The SSTDR wave pattern is simulated in Figure 19, with separated models of each segment shown in Figure 20 and Figure 21.

It can be seen from the simulated results that the traveling waves, F and B, are successfully separated and identified in each of the cases. The ability to separate the waves is proven to be independent of the wave shape, but appears to work best when the waveform is simplified and narrowed, as in the case of the pulse.

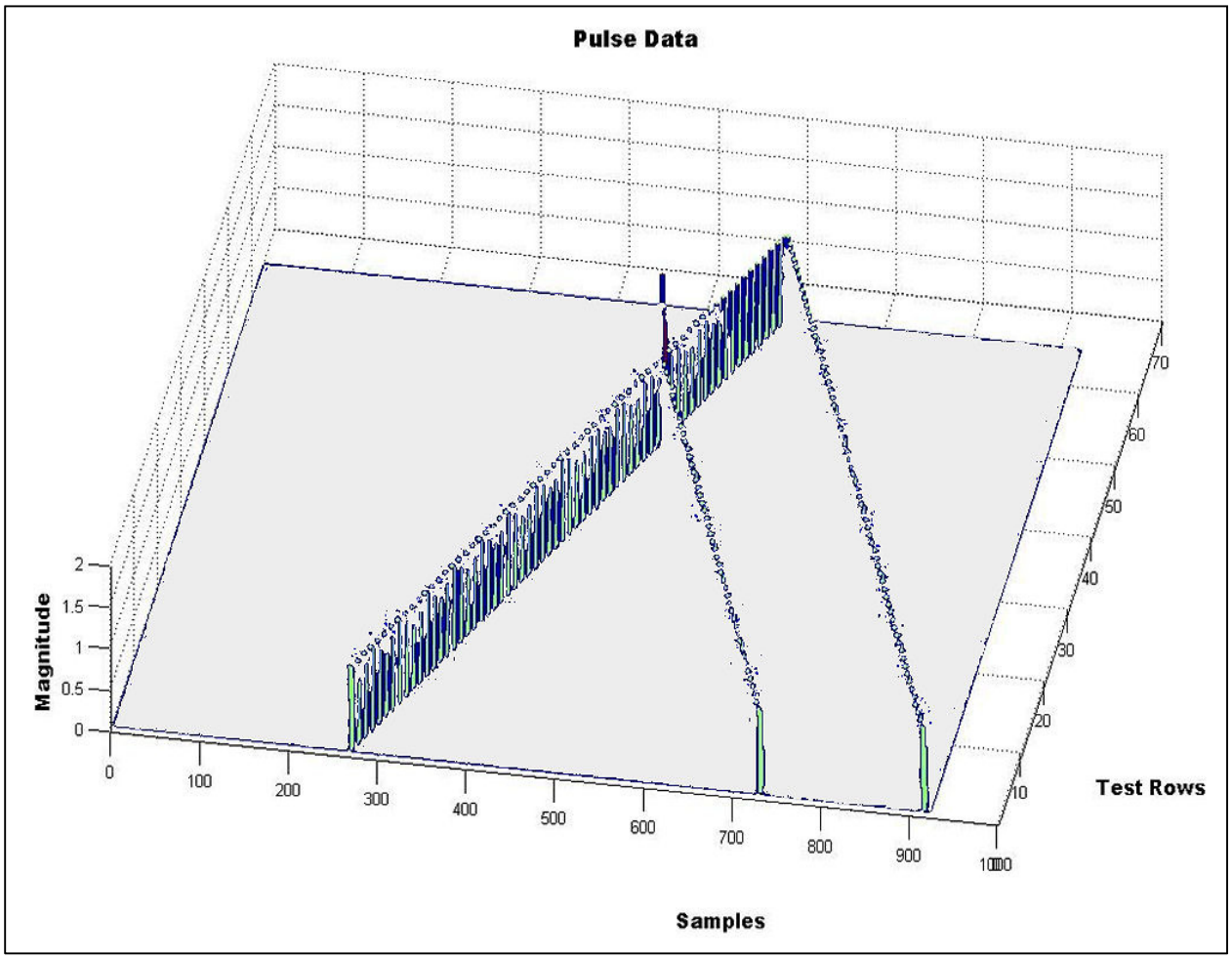

Figure 10: Simulated data set using a pulse wave pattern.

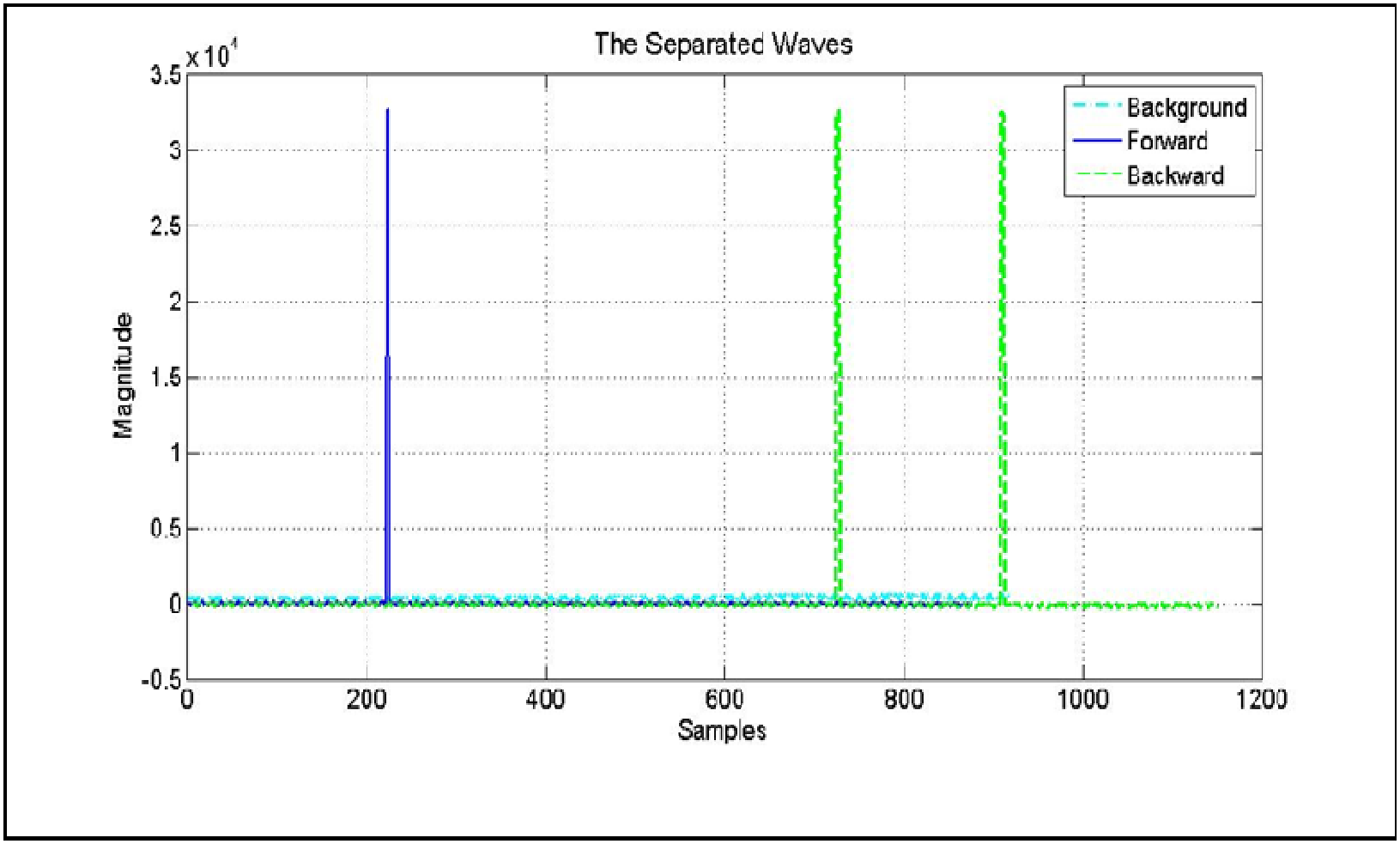

Figure 11: Pulse: separated models of FB waveforms, algorithm results of simulated data.

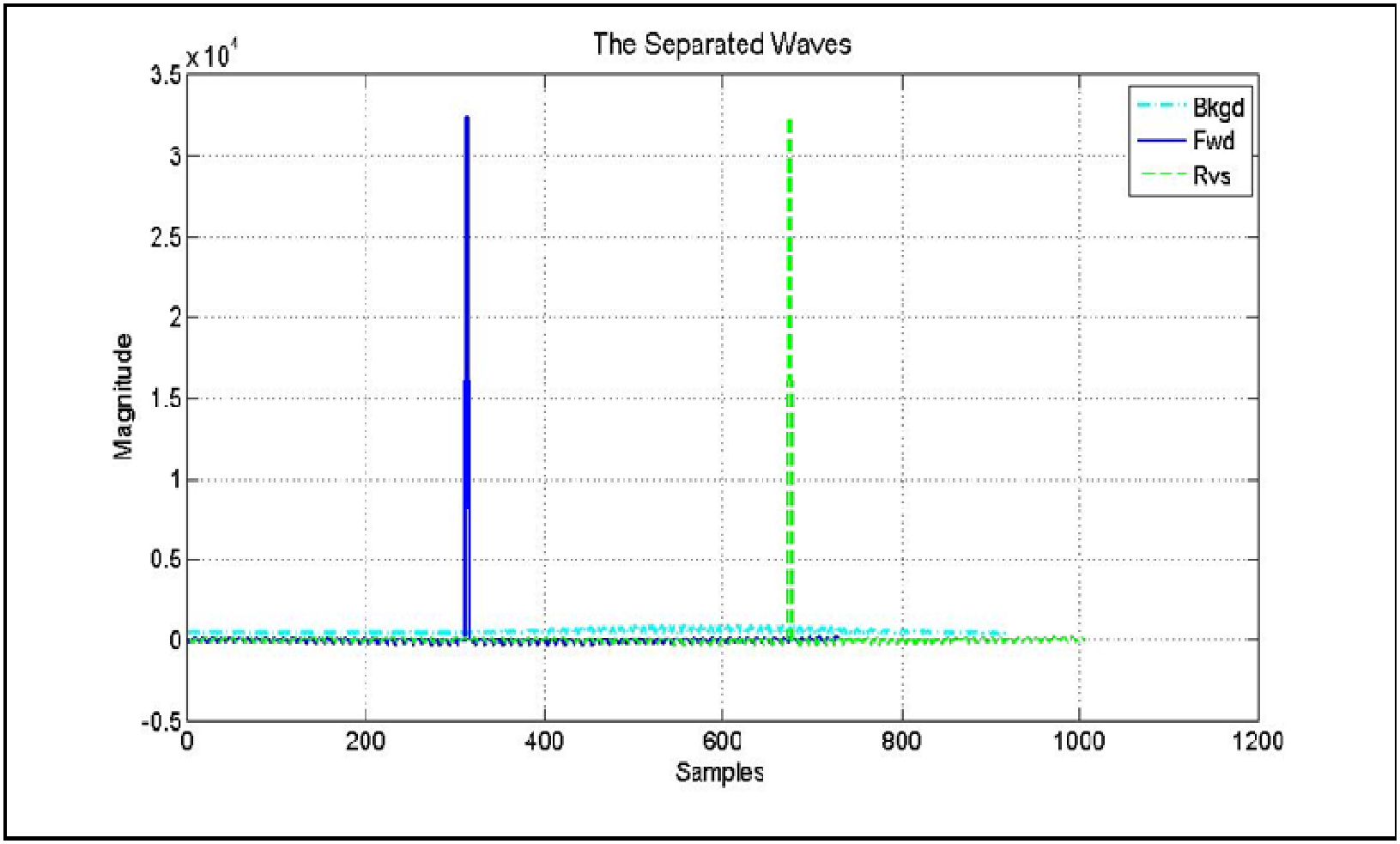

Figure 12: Pulse: Separated models of FB waveforms after passing the first reflection.

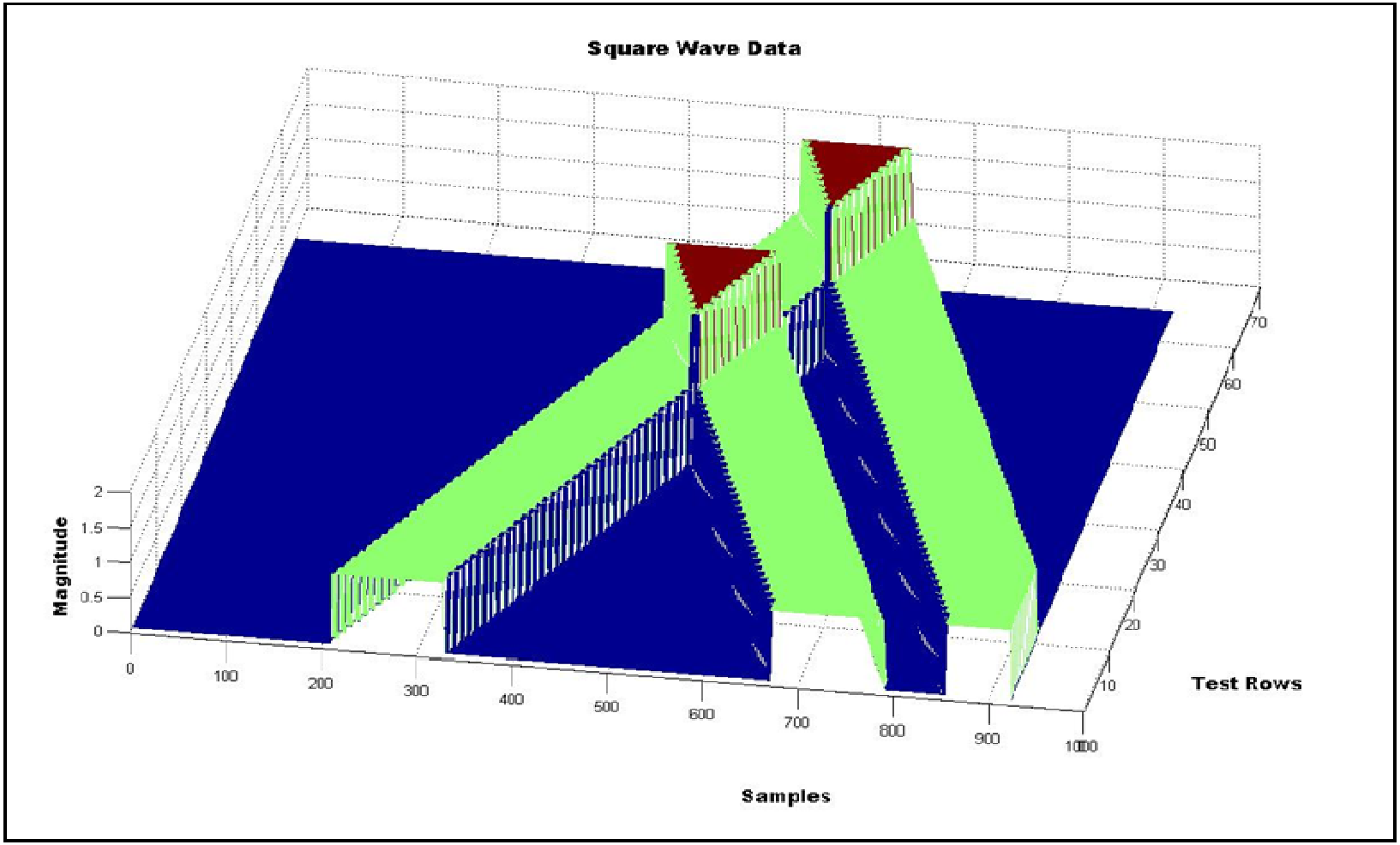

Figure 13: Simulated data set using a square wave pattern.

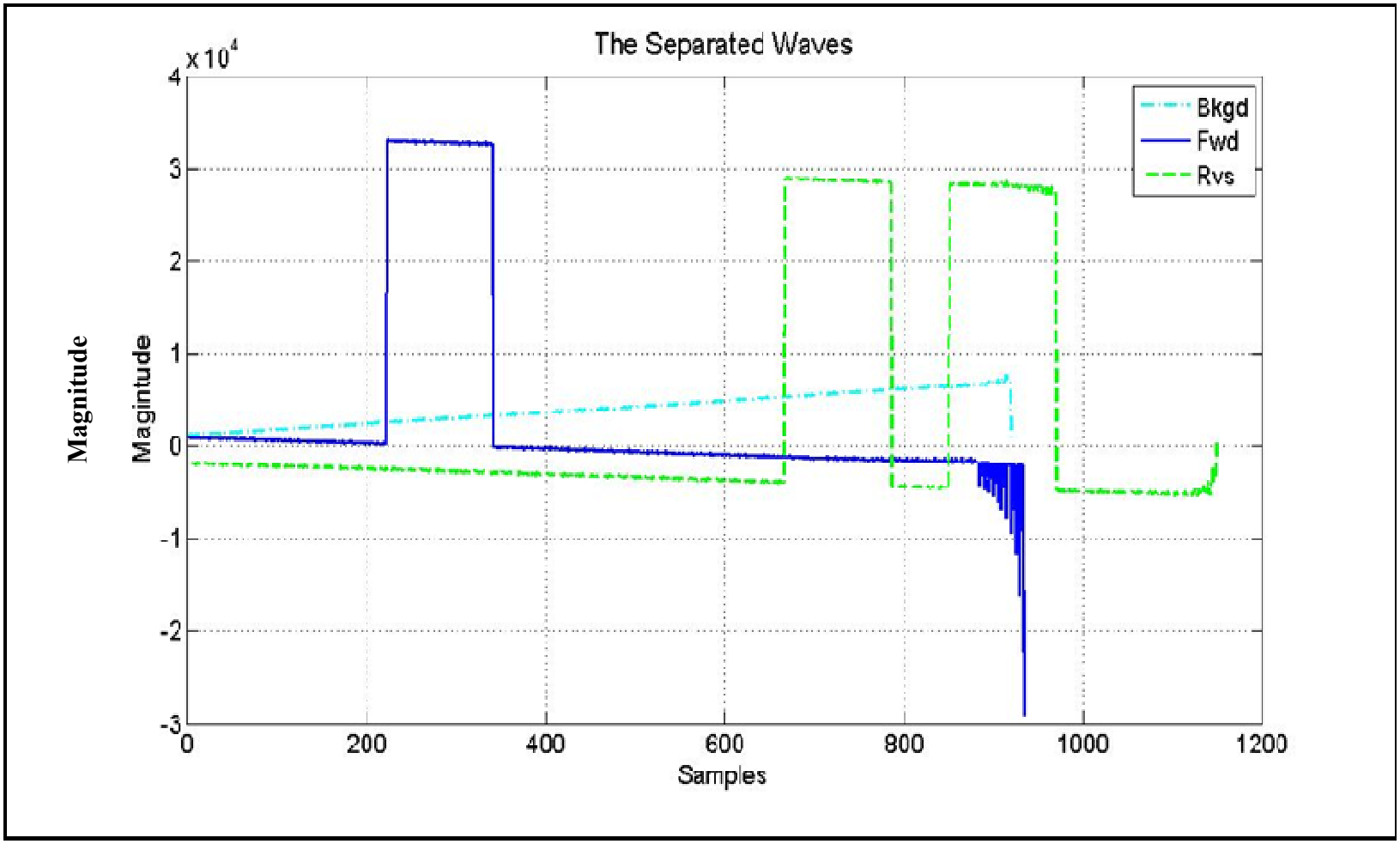

Figure 14: Square: separated models of FB waveforms, algorithm results of simulated data.

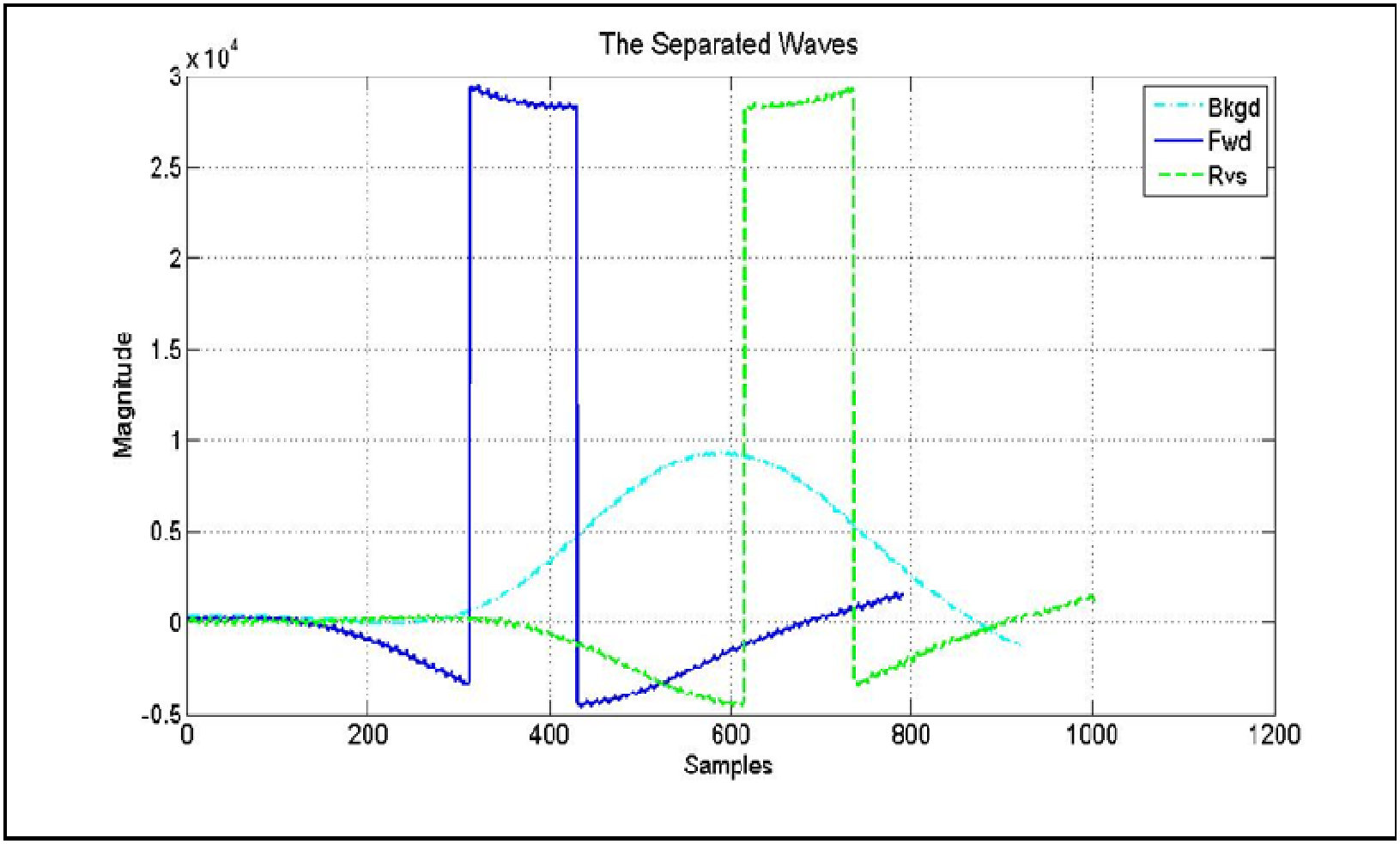

Figure 15: Square: separated models of FB waveforms after passing the first reflection.

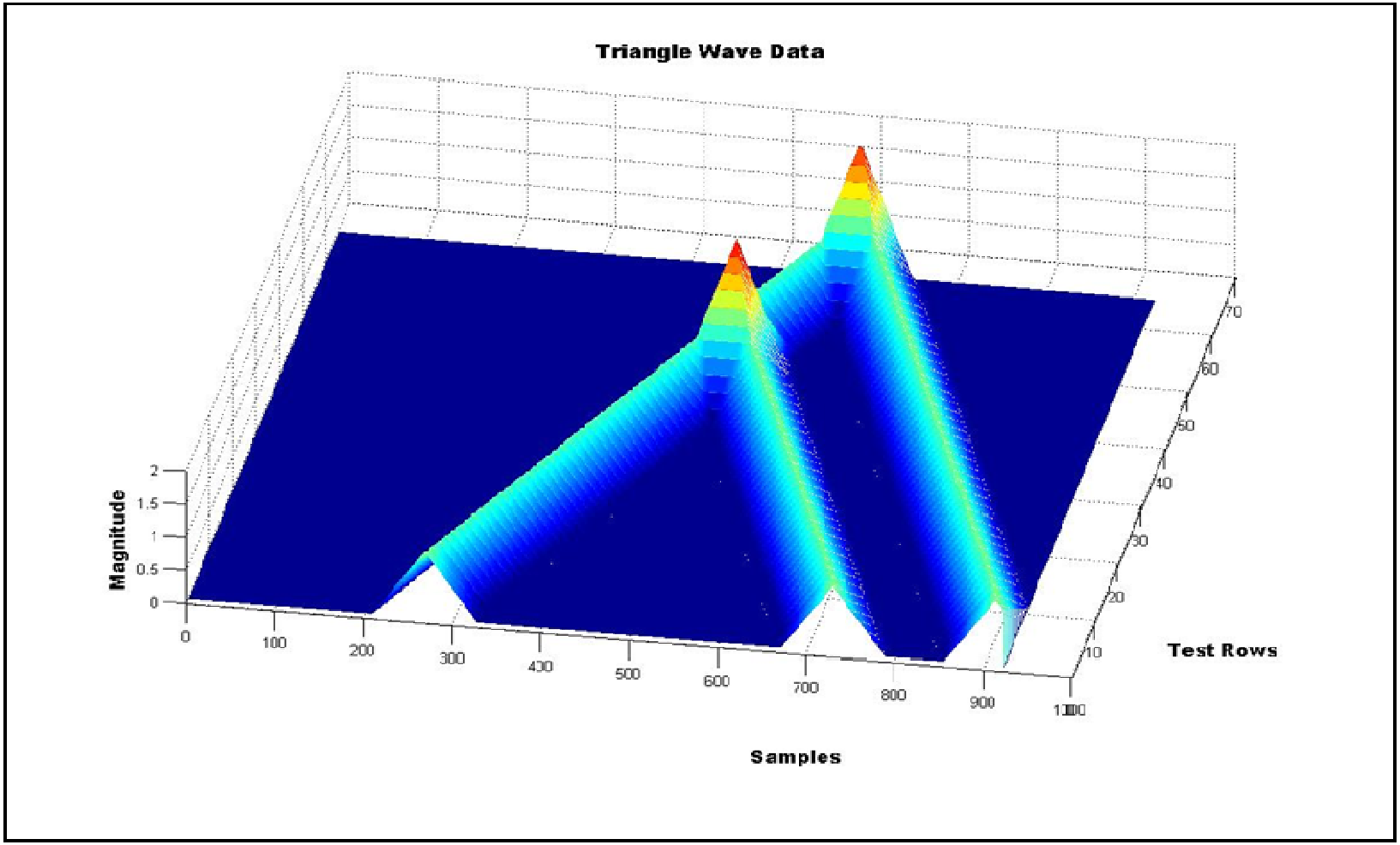

Figure 16: Simulated data set using a triangle wave pattern.

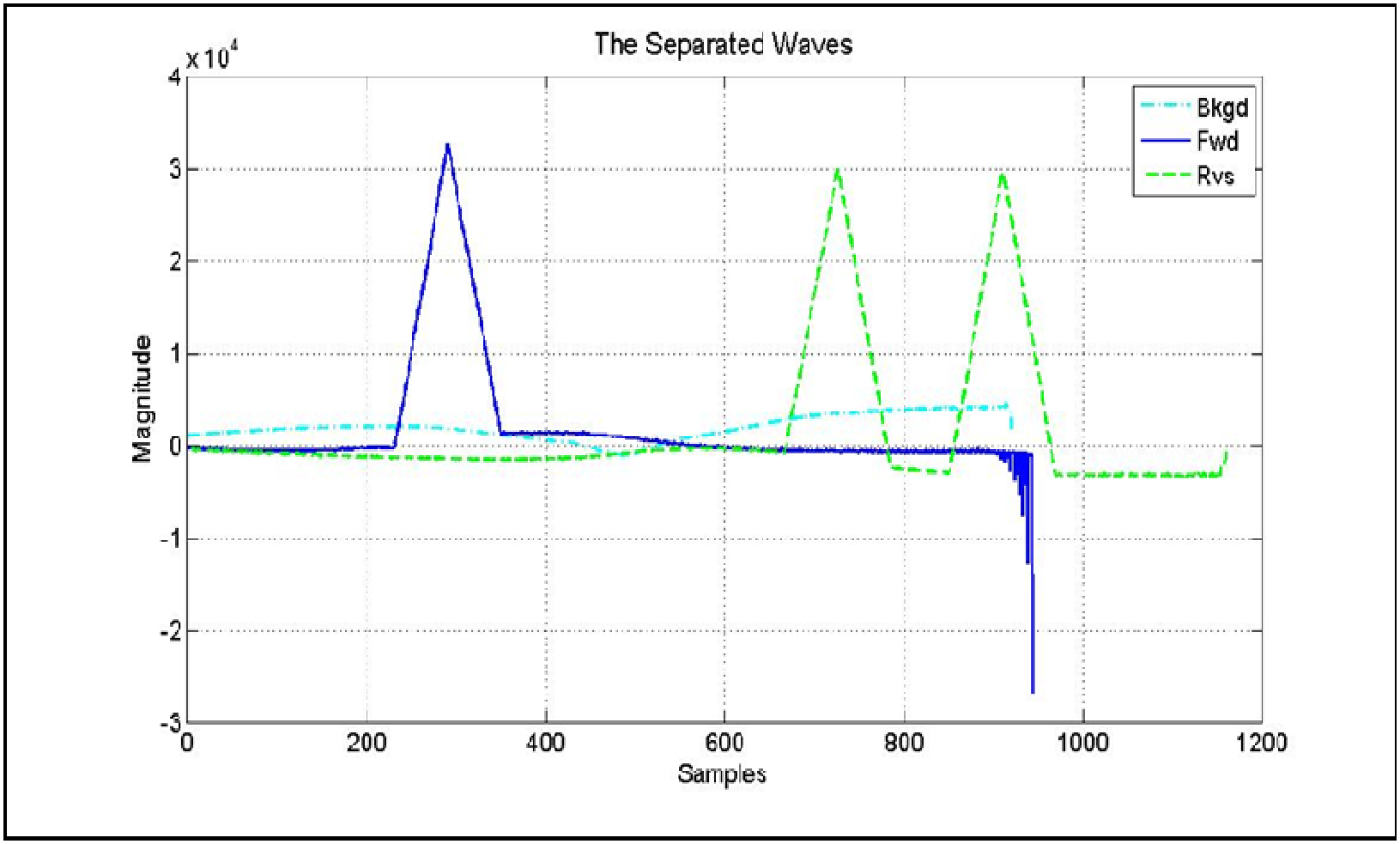

Figure 17: Triangle: separated models of GFB waveforms, algorithm results of simulated data.

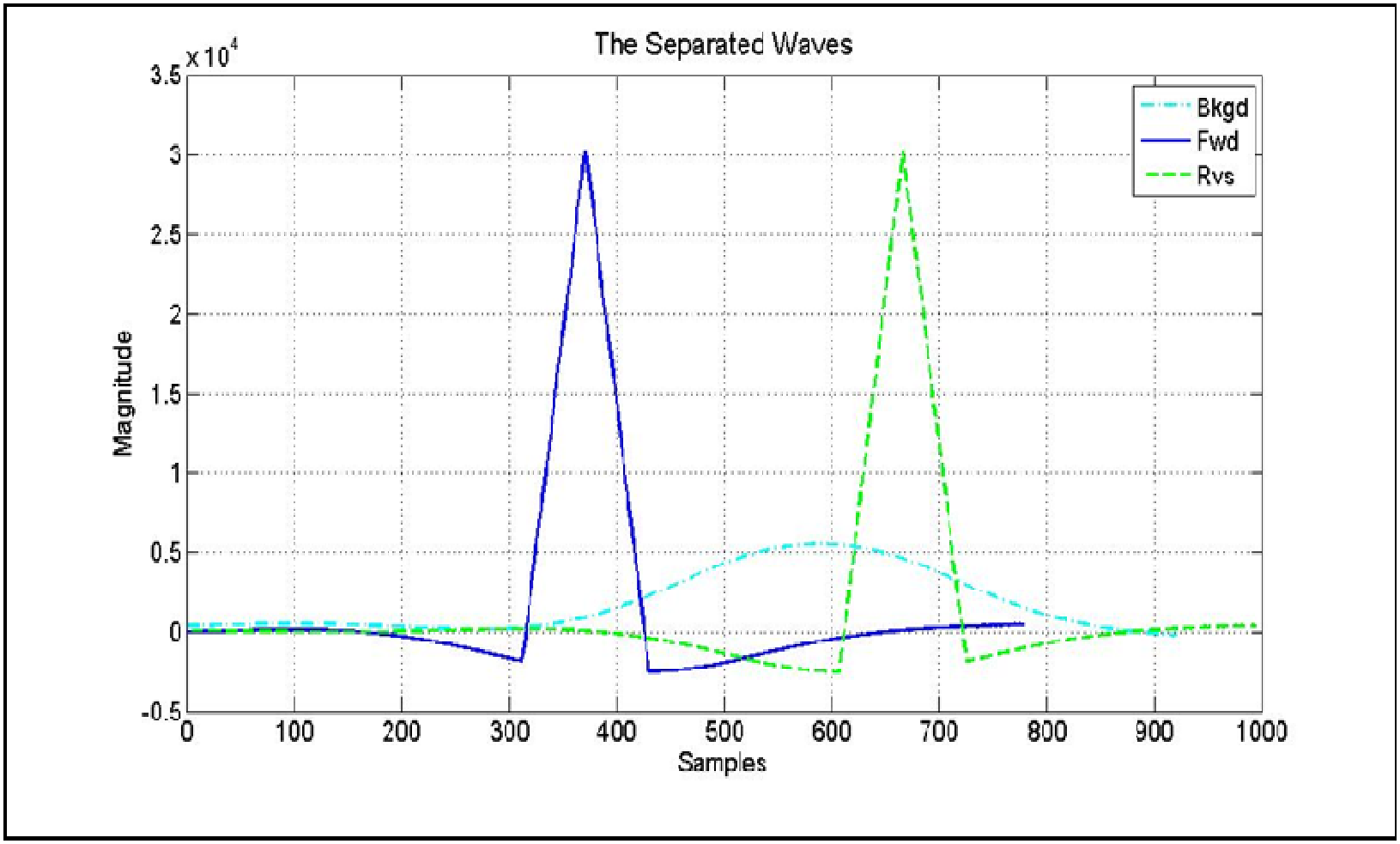

Figure 18: Triangle: separated models of GFB waveforms after passing the first reflection.

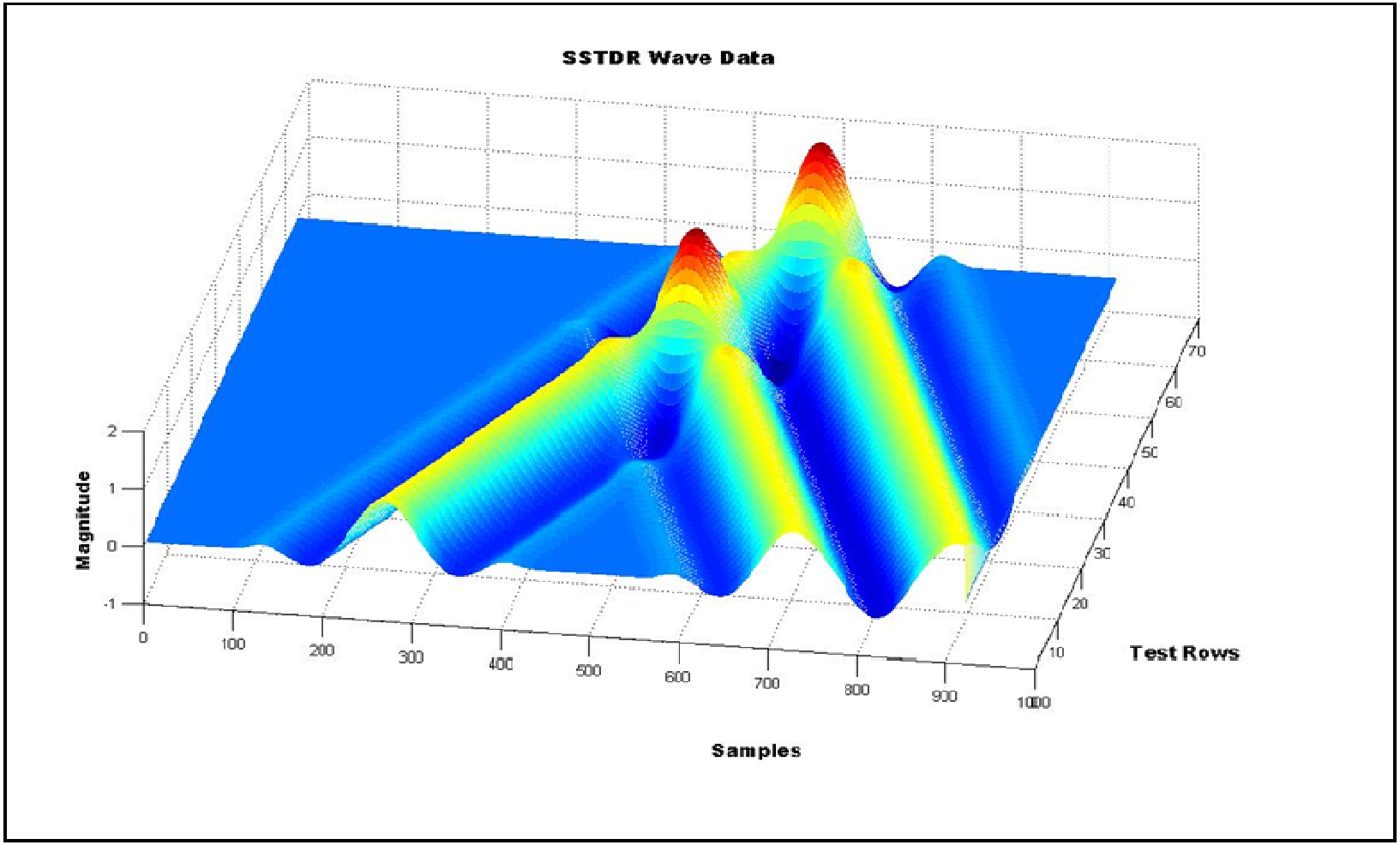

Figure 19: Simulated data set using a convolved SSTDR wave pattern.

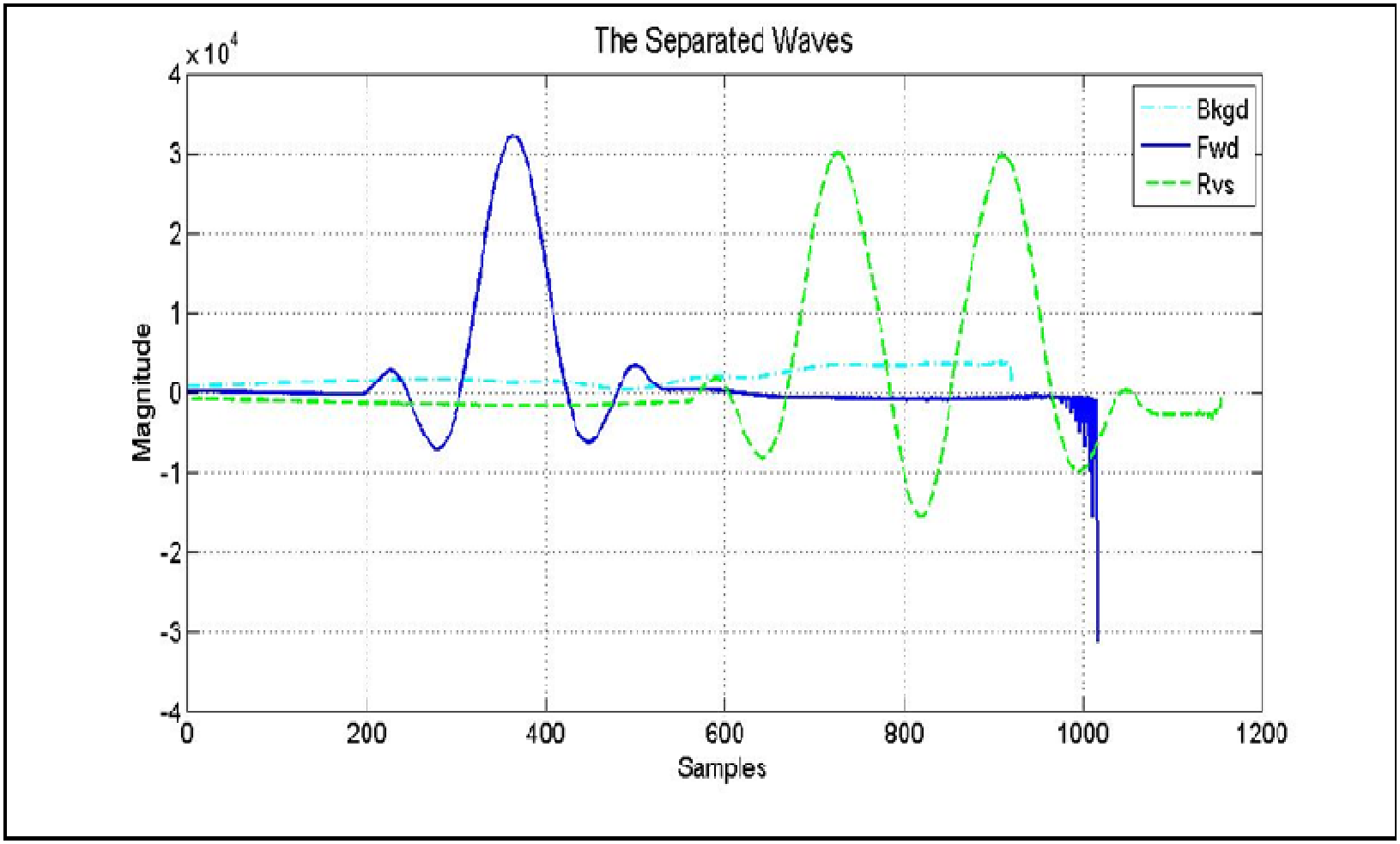

Figure 20: SSTDR: separated models of GFB waveforms, algorithm results of simulated data.

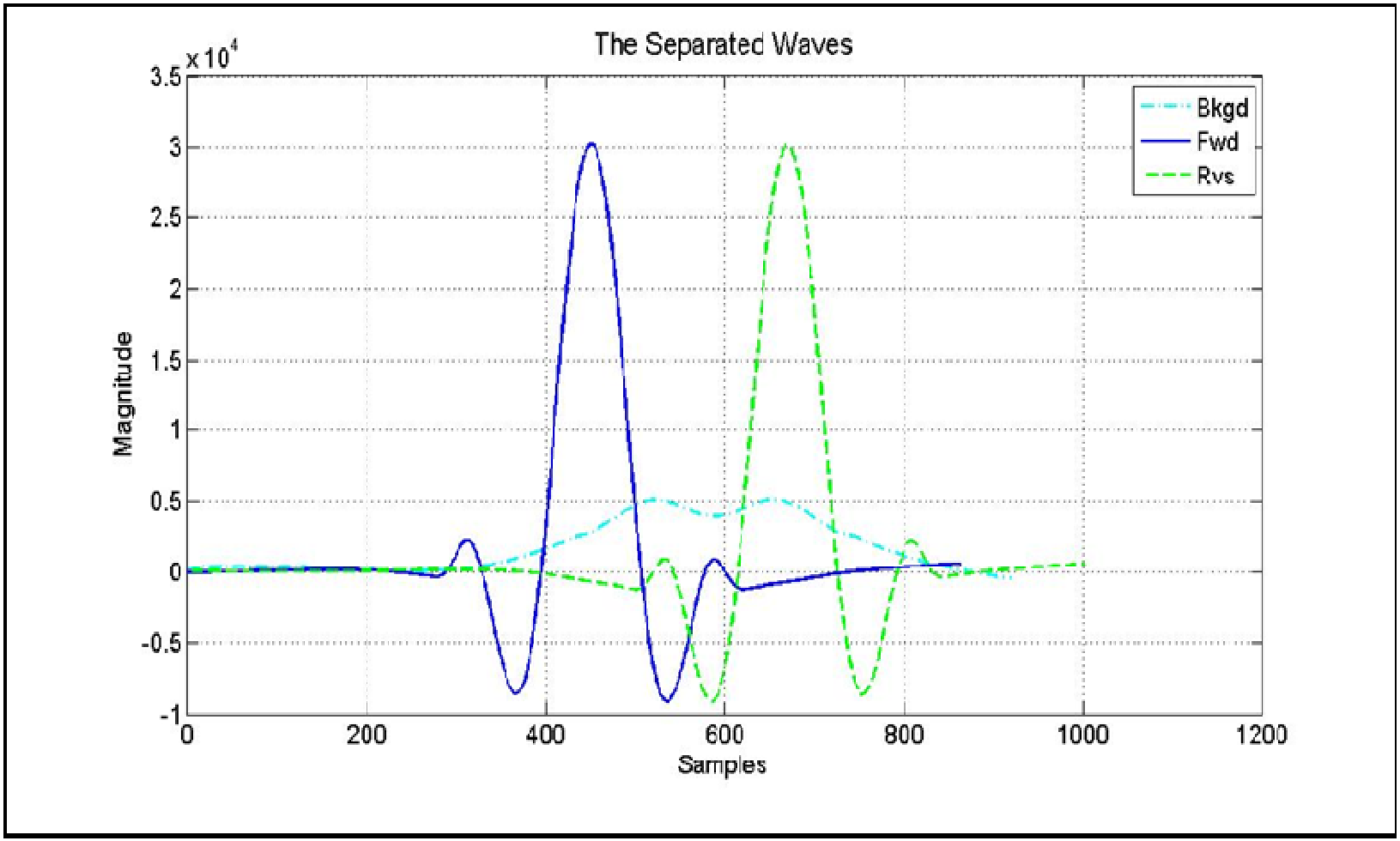

Figure 21: SSTDR: separated models of GFB waveforms after passing the first reflection.

Notice the large amount of data categorized as background G particularly in cases when data are collected after passing the first reflection point. Because the input data are simulated and contain zero noise, model results are categorized as background G only when it could not be placed as a traveling wave. In other words, in a noiseless environment the background is synonymous with error. The cause of this error can be predicted by performing another test, to determine if the algorithm transitions improperly from one segment to the next, or if the errors are due to an insufficient amount of data rows, not allowing the algorithm enough iteration to clearly resolve the traveling waves.

Figure 22 shows a simulated data set using a convolved SSTDR wave pattern, with a short or reflection near the starting point. Figure 23 and Figure 24 show the separated models of each segment of the simulated data. Notice from Figure 23 and Figure 24 that the error indicated by high G movement does not stay with the segment transition, but rather follows the segment with the smaller number of rows, and more importantly, the smaller amount of distance traveled. This means that a short segment is a significant cause of modeling errors, particularly if there is not distinguishing data within the segment.

4.1.1 Number of Required Test Locations vs. Resolution

Observations in the previous section lead to the question of how many rows of data are required to separate the forward and backward traveling waves enough to obtain a successful distance reading. This ability will also depend on the robustness of the distance calculating algorithm (developed separated), amount of noise in the system, and the distance traveled between incremental measurements. To reduce this to a single

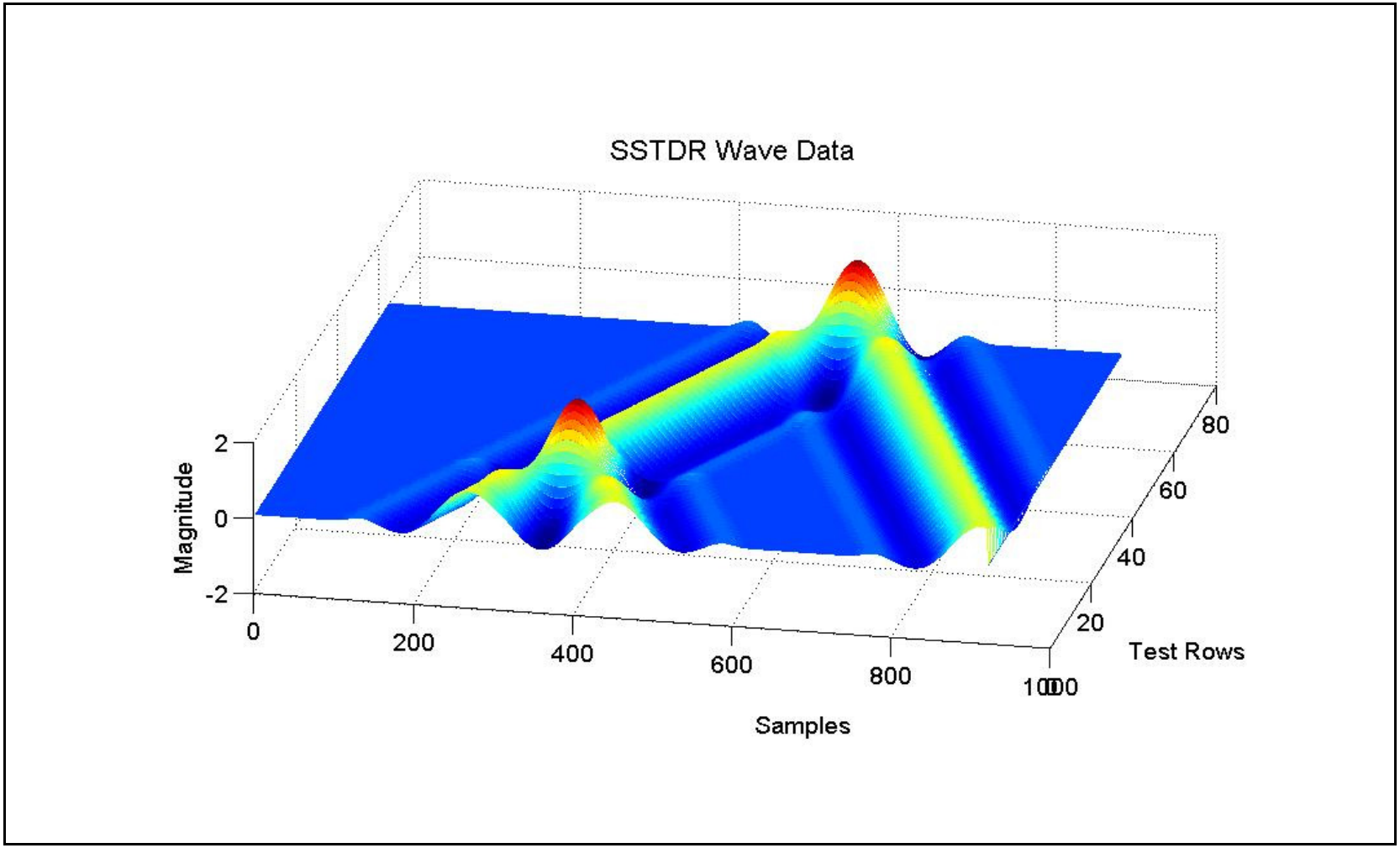

Figure 22: Simulated data set using a convolved SSTDR wave pattern, first reflection positioned close to the starting point.

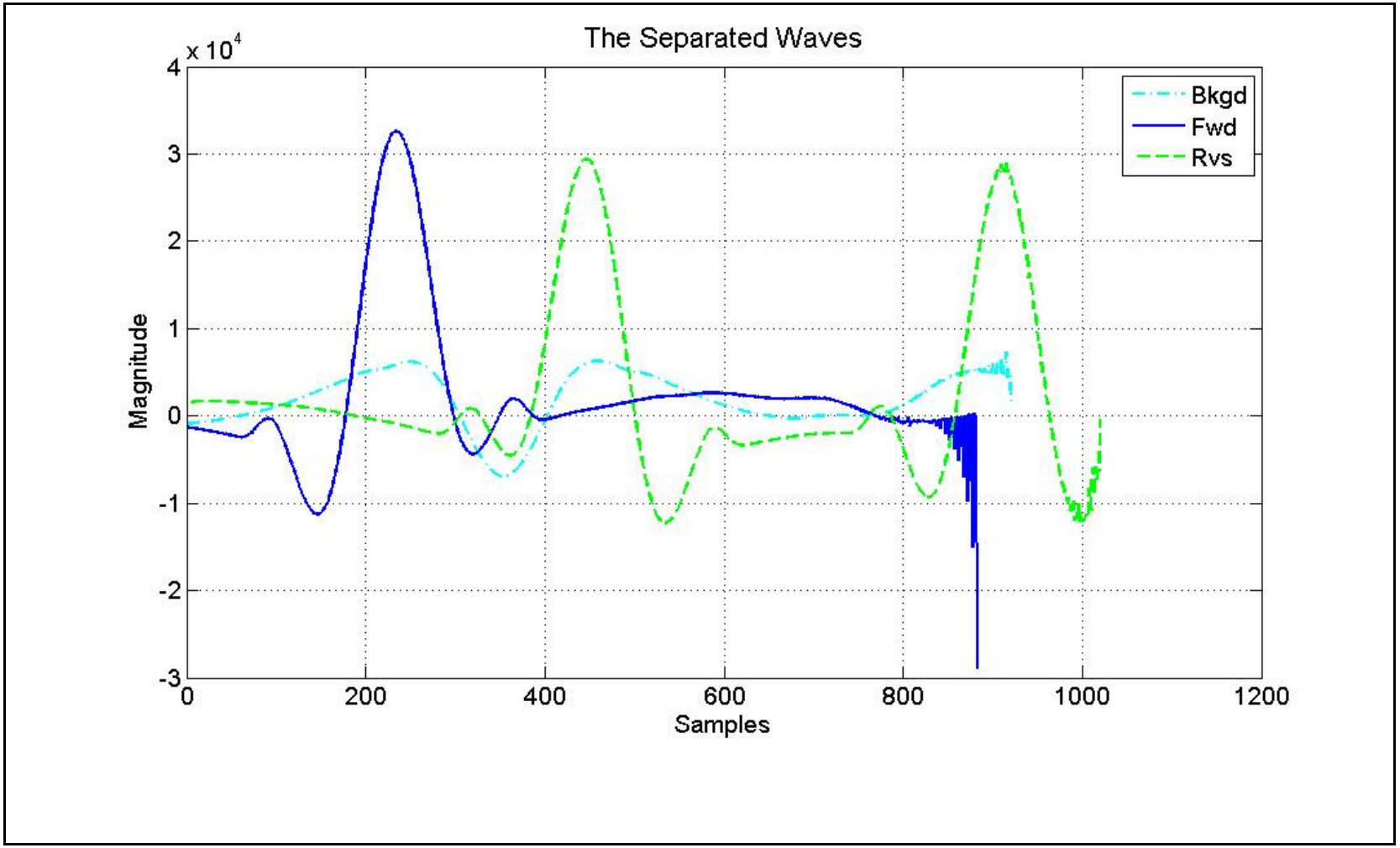

Figure 23: SSTDR: separated models of GFB waveforms, algorithm results of simulated data.

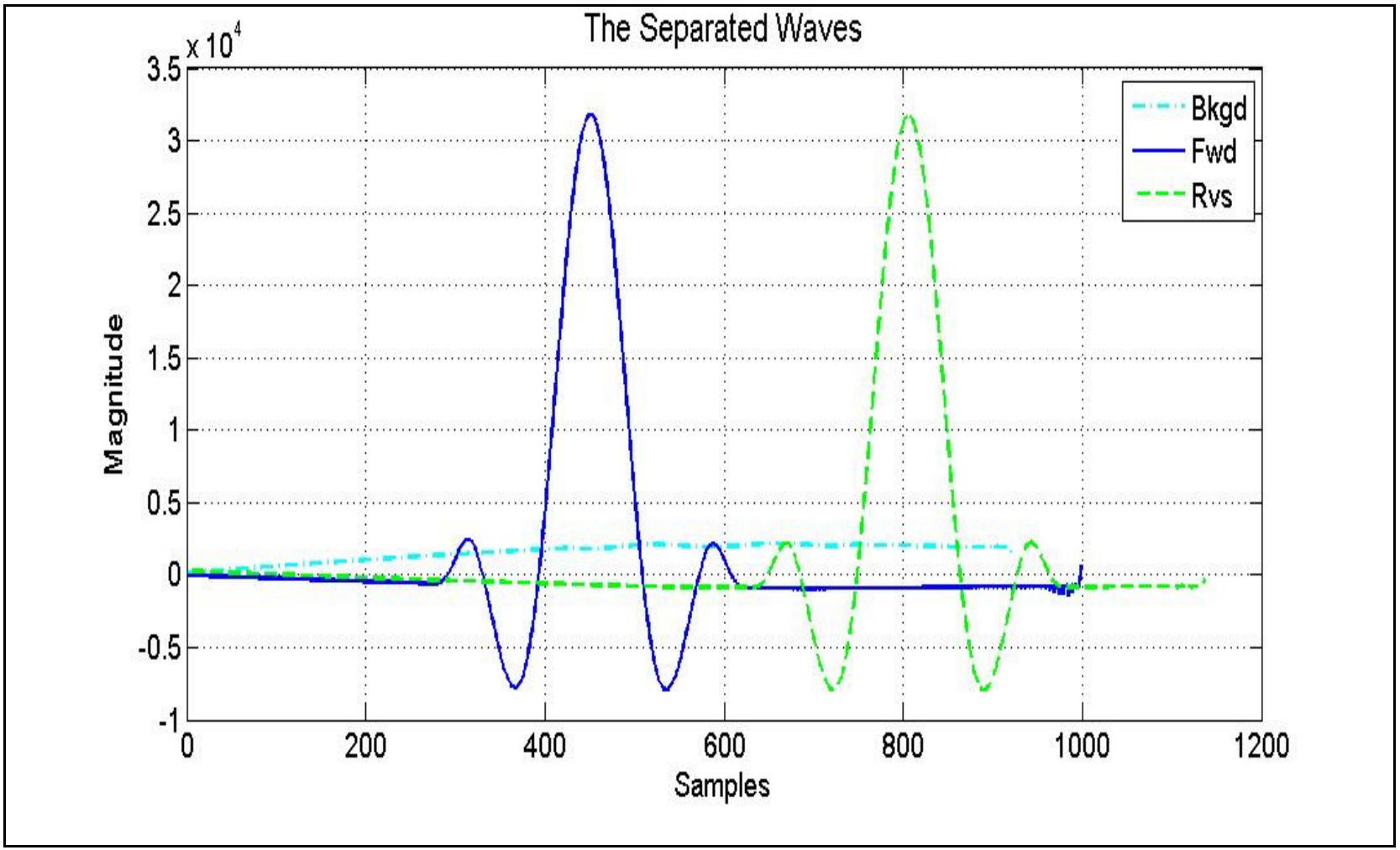

Figure 24: SSTDR: separated models of GFB waveforms after passing the first reflection.

experimental variable the data are kept noiseless, the distance calculating algorithm remains unchanged, and the distance traveled between measurements remains constant. Only the number of tests, and thus the tested length of the segment, is adjusted.

Experience with the algorithm and test equipment called for the algorithm to not be performed until 6 rows of data have been collected. Unpredictable results are more likely to occur if using fewer rows of data. Therefore, we set 6 to be the minimum and move on from there. The misfit of the model is used to show how much change to the model is caused by the addition of each new row of data. Notice in Figure 25 that the misfit is calculated only after 6 rows have been collected.

It is observed in Figure 25 that at row 12 the misfit begins to dramatically reduce. This reduction is caused by the success of the algorithm in modeling the traveling waves well enough so that the addition of data causes fewer changes to the model. Our confidence that the model is correct increases as additional data produce only minor changes to the model. The simulated row 12 can be roughly correlated to a distance 6 feet from the starting point.

4.1.3 Random Noise Injection

In order to test the algorithm in a noisy environment random noise was injected into the simulated data. The input data were combined with random 2% magnitude noise and the results are shown in Figure 26 and Figure 27. The input data were combined with 10% noise and the results are shown in Figure 28 and Figure 29.

The algorithm performs successfully in both 2% and 10% noise. While performing noise experiments it was quickly found that injecting more than 10% of random noise will often break the other mechanisms of the test software before affecting the inversion algorithm. Because of these technical problems, the pure ability of the algorithm in a random noise environment could not be analyzed. In practice, random noise is removed to less than 1% by averaging multiple rows of data collected at the same location. Interference caused by external sources or metallic structures are a more likely cause of algorithm failure. Future work could include modeling of interference source during simulation to explore the effects.

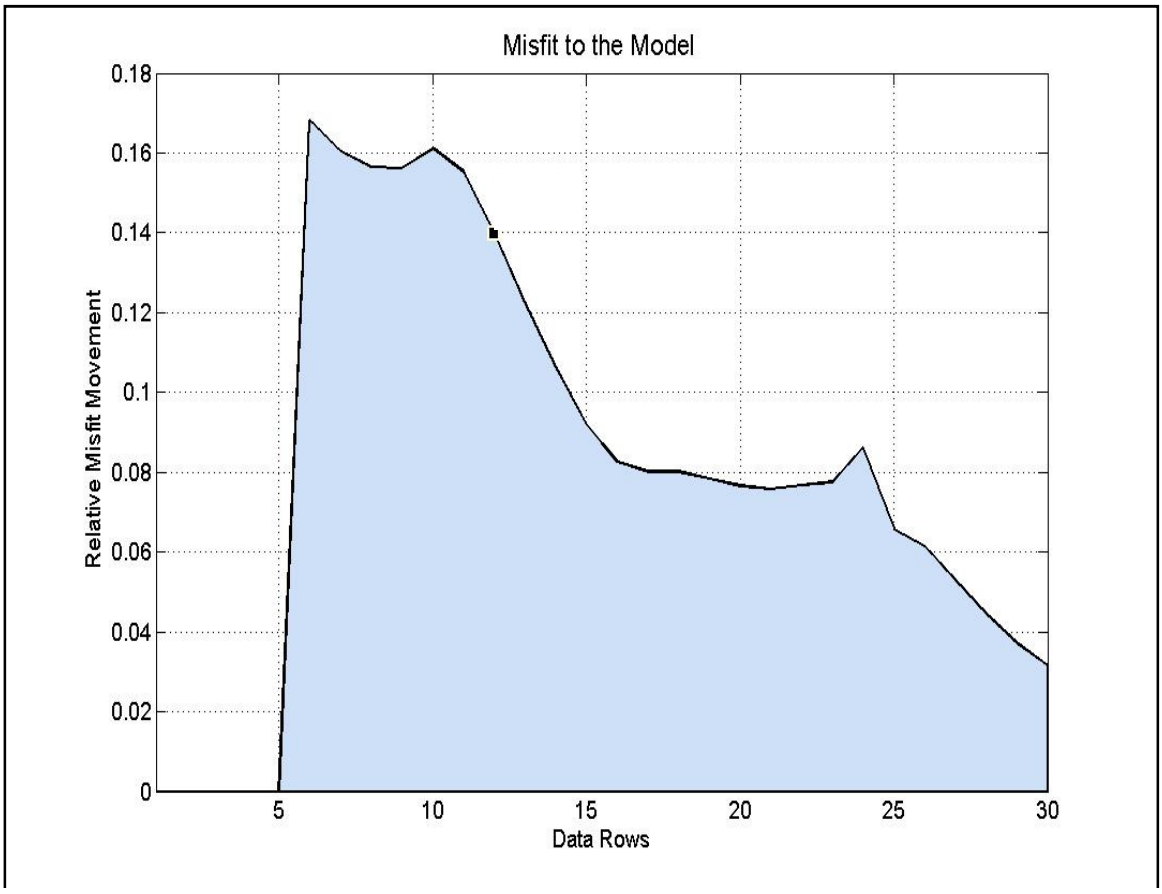

Figure 25: Misfit to the model is calculated as each row is added to the base of data.

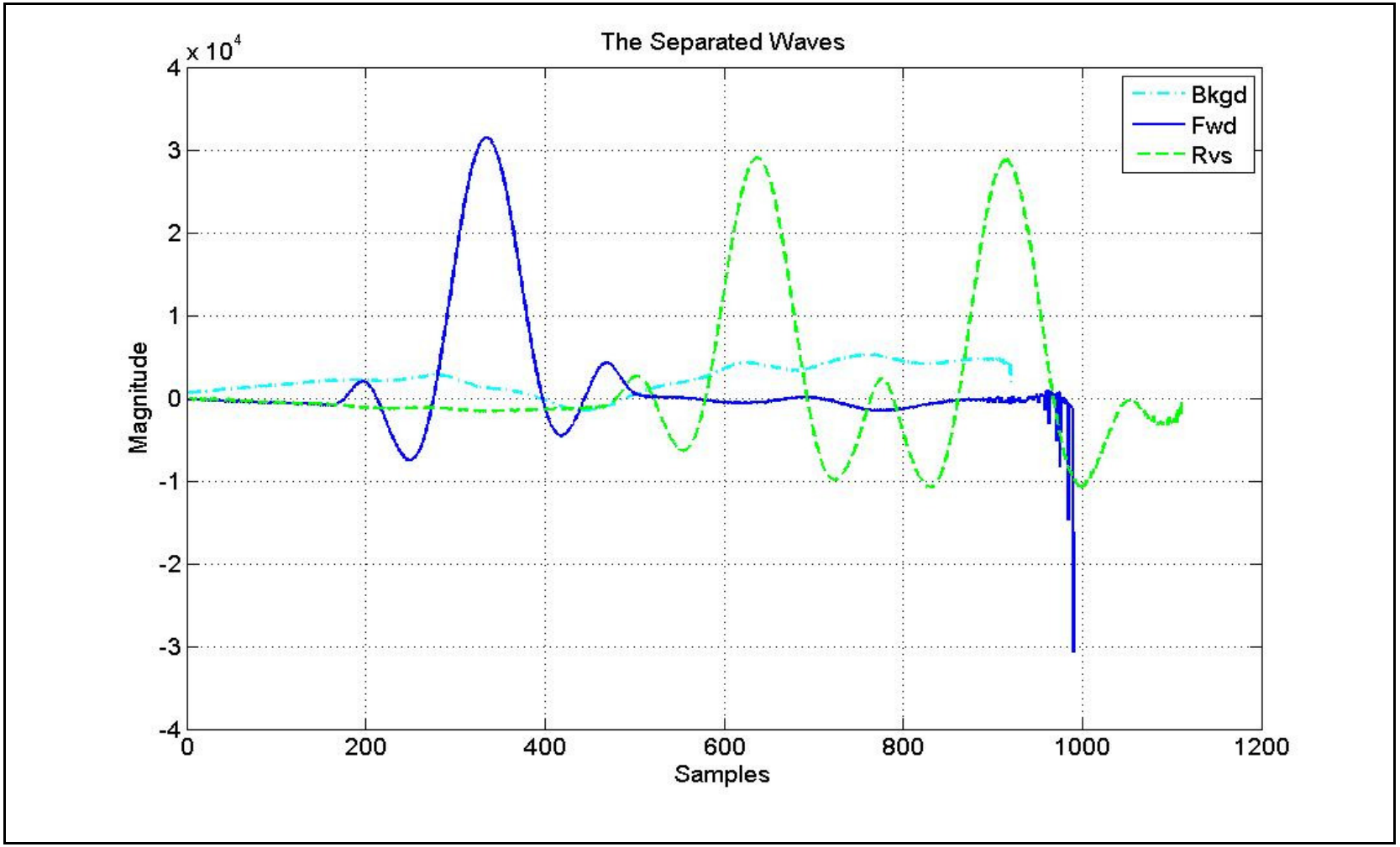

Figure 26: SSTDR: separated models of GFB waveforms of the first segment, with 2% noise injected.

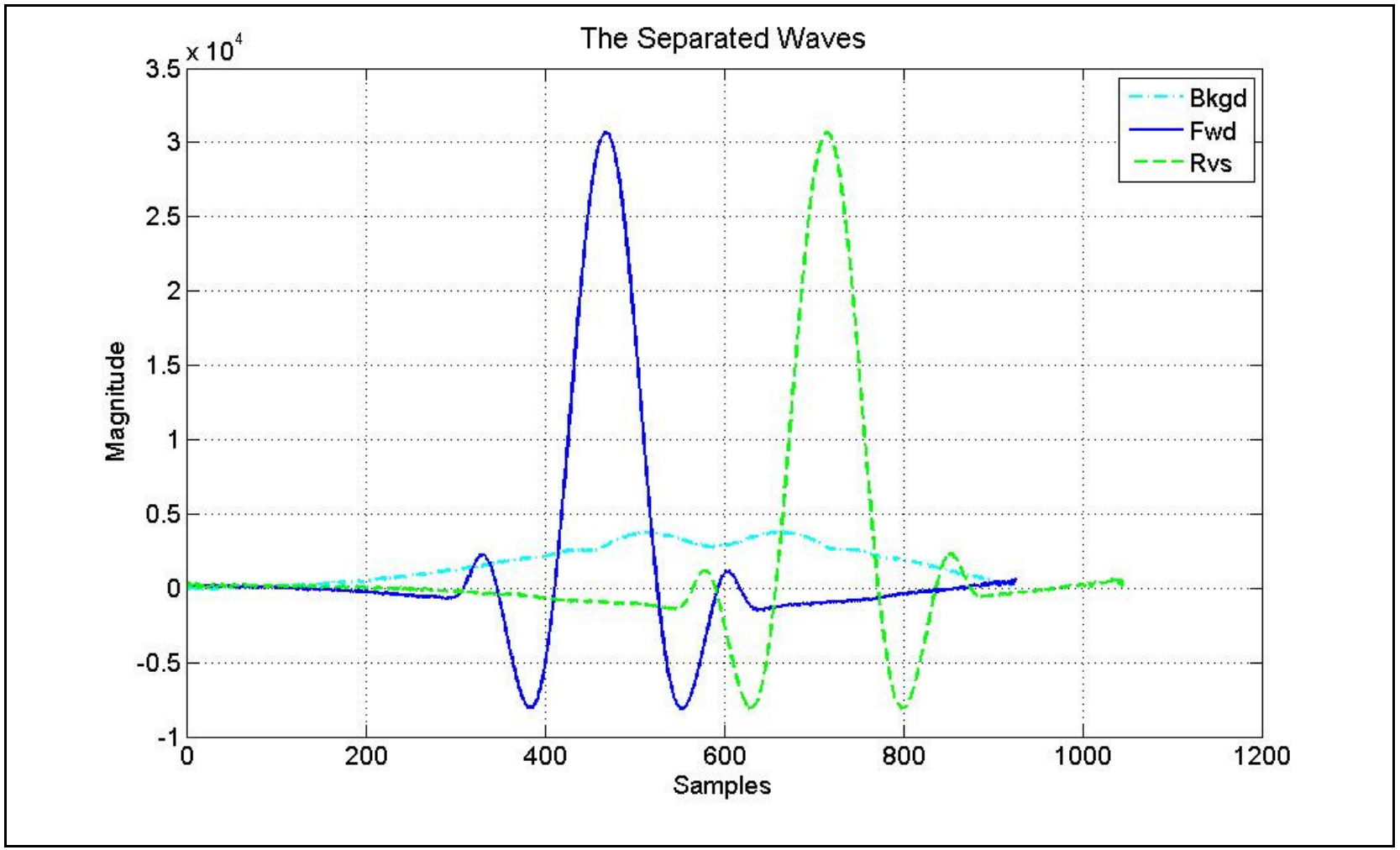

Figure 27: SSTDR: separated models of GFB waveforms of the second segment, with 2% noise injected.

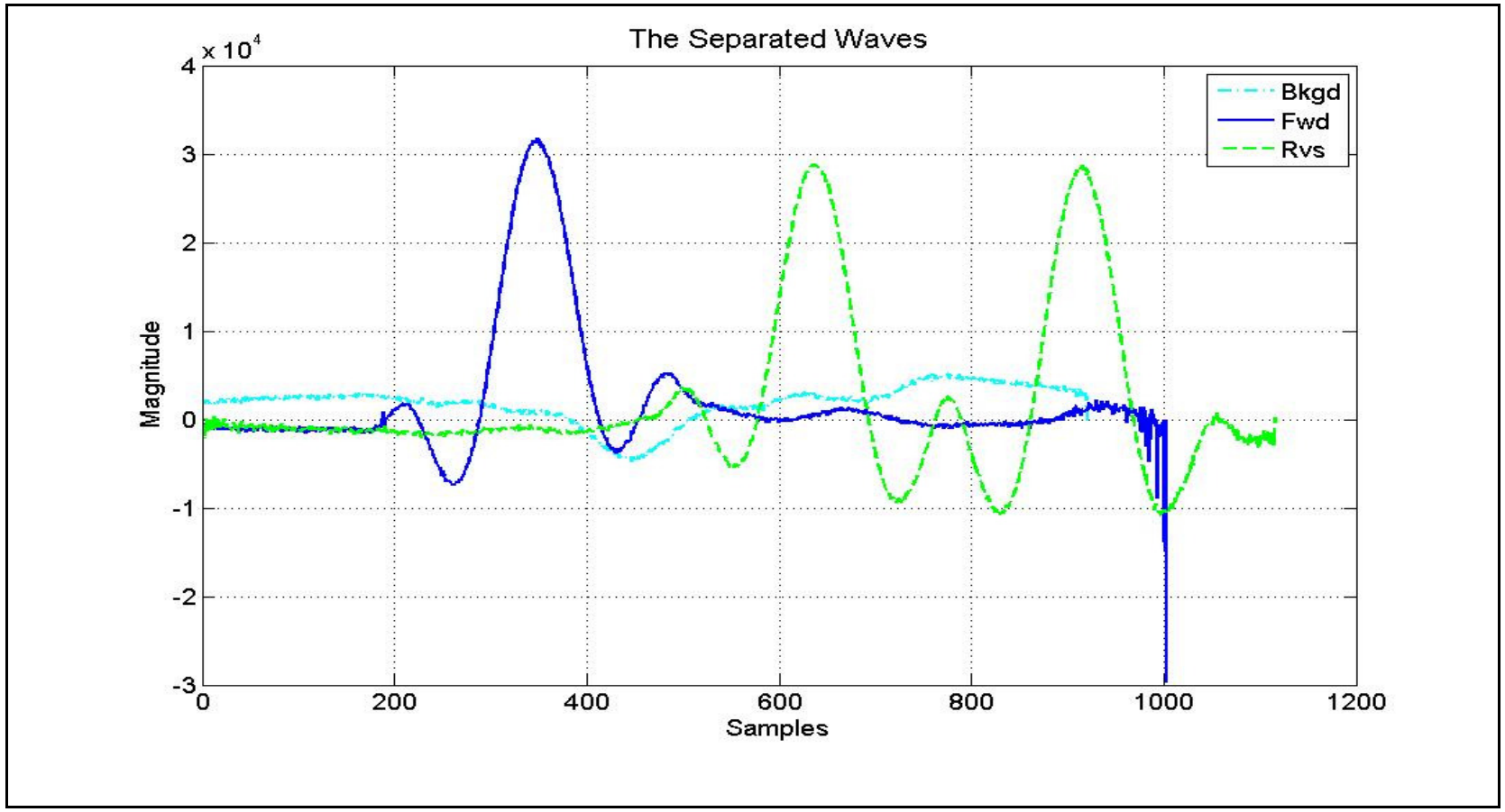

Figure 28: SSTDR: separated models of GFB waveforms of the first segment, with 10% noise injected.

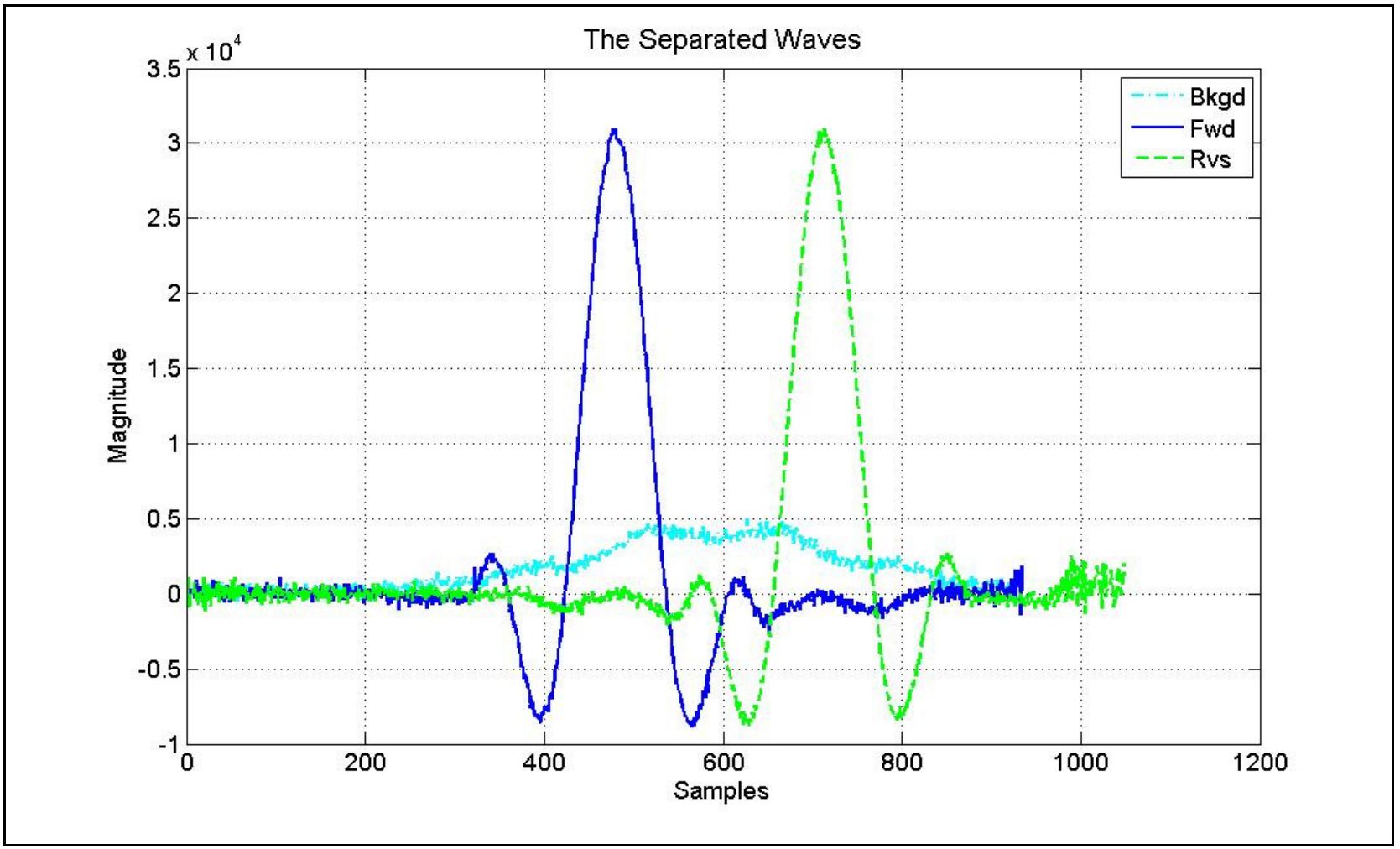

Figure 29: SSTDR: separated models of GFB waveforms of the second segment, with 10% noise injected.

4.2 Measured Results

The following section contains results, charts, and tables that were prepared by the author at Livewire Test Labs for the Federal Aviation Administration (FAA). These elements are used with permission from the FAA.

4.2.1 Wave Separation Results

Figure 30 shows the branched network test cases that involve a three-segment network. The test cases consist of a two-conductor trunk wire that has a branch attached at some point along the wire. Faults will be placed at the ends or within segment 2. The purpose for these tests is to show the capabilities of detecting faults, detecting branches, locating faults beyond branches, and locating networks beyond faults.

The results contain processed waveforms reconstructed by the algorithm, along with the calculated segment length. The results also contain graphical representations of the relative difference between the calculated model of the wire to that point and the next set of data presented.

Three-segment branched network experiments were set up. Data were collected using an EM probe while injecting SSTDR signals onto the test wires at 144 MHz. The EM probe was positioned within proximity of 3 inches of the wire, each test taken at an interval of six inches along the entire length of the wire.

The algorithm provides information required for graphically reconstructing the topography of the wire. This information comes packaged into segments. The segment number and segment length are reported, and can be referenced to the known topology

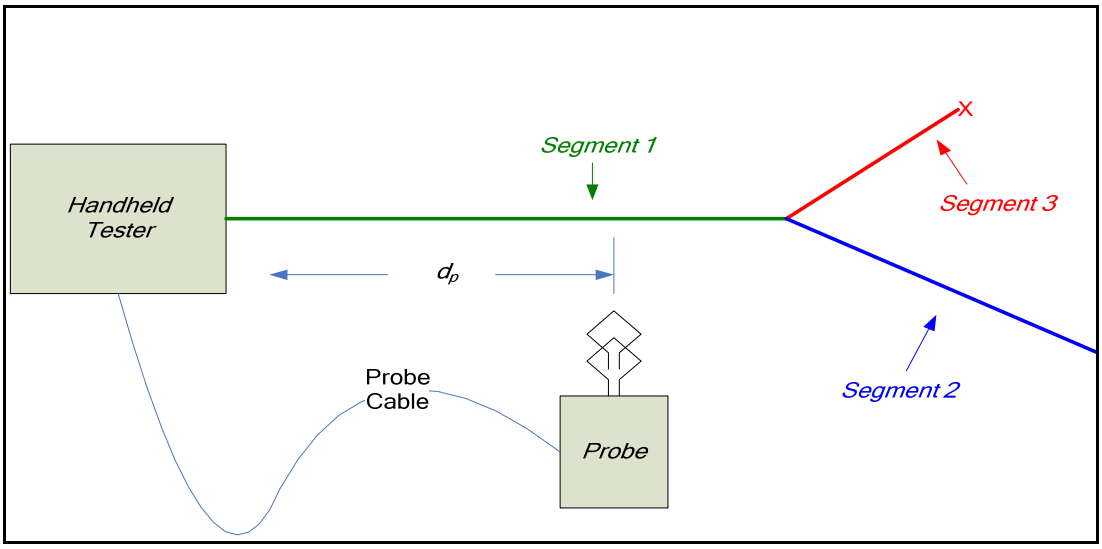

Figure 30: Three-segment Network Test Case

described in Table 2 for each test configuration. Figure 31 shows an example of a full set of collected data. The data are visually divided into the segments that were scanned, allowing one to note the extreme changes that occur to the data when a reflection point is passed.

The following tests were performed on a three-segment test wire, as shown in Figure 30 and described in Table 2. The branched point and types of faults are the variable factors between the tests. In the waveform figures, the y-axis scaling is shown to indicate relative amplitude of each composite waveform and is normalized to the maximum of the signal. The segment length calculation was based on the point chosen by the algorithm as described previously.

Table 2: Three-segment Test Configuration Details

Test Description - Actual Segment Lengths (ft)				
Test	Segment 1	Segment 2	Segment 3	Feature of Interest
3-1	6.5	24.5	11	both ends open
3-2	14.5	16.5	11	both ends open
3-3	23.5	7.5	11	both ends open
3-4	6.5	24.5	11	end of Deg 3 short
3-5	14.5	16.5	11	end of Deg 3 short
3-6	23.5	7.5	11	end of Deg 3 short

4.2.1.1 Tests on Branched Wire – Both Open Ends

The following tests were performed while both end points of the branched wire were left in an open circuit condition.

4.2.1.1.1 Test 3-1 (Branch Point at 6.5 Feet)

Figure 32, Figure 33, and Figure 34 show the resultant forward and backward traveling waveform reconstruction of each segment of a three-segment network with a branching point at 6.5 feet, an open circuit at 24.5 feet past the branching point, and an open circuit 11 feet past the branching point on the other branch.

4.2.1.1.2 Test 3-2 (Branch Point at 14.5 Feet)

Figure 35, Figure 36, and Figure 37 show the resultant forward and backward traveling waveform reconstruction of each segment of a three-segment network with a

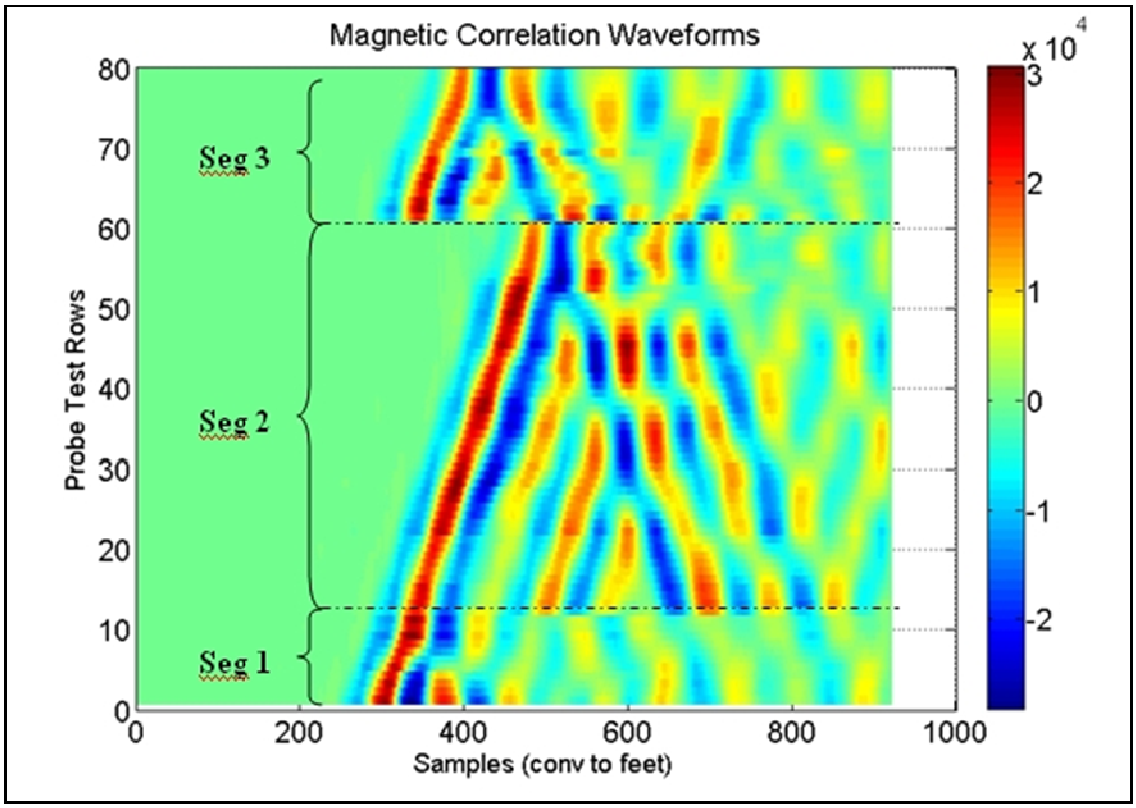

Figure 31: Example of a full data set seen from a top view, with visual marking of the segment from which each test row was collected.

branching point at 14.5 feet, an open circuit at 16.5 feet past the branching point, and an open circuit 11 feet past the branching point on the other branch.

4.2.1.1.3 Test 3-3 (Branch Point at 23.5 Feet)

Figure 38, Figure 39, and Figure 40 show the resultant forward and backward traveling waveform reconstruction of each segment of a three-segment network with a branching point at 23.5 feet, an open circuit at 7.5 feet past the branching point, and an open circuit 11 feet past the branching point on the other branch.

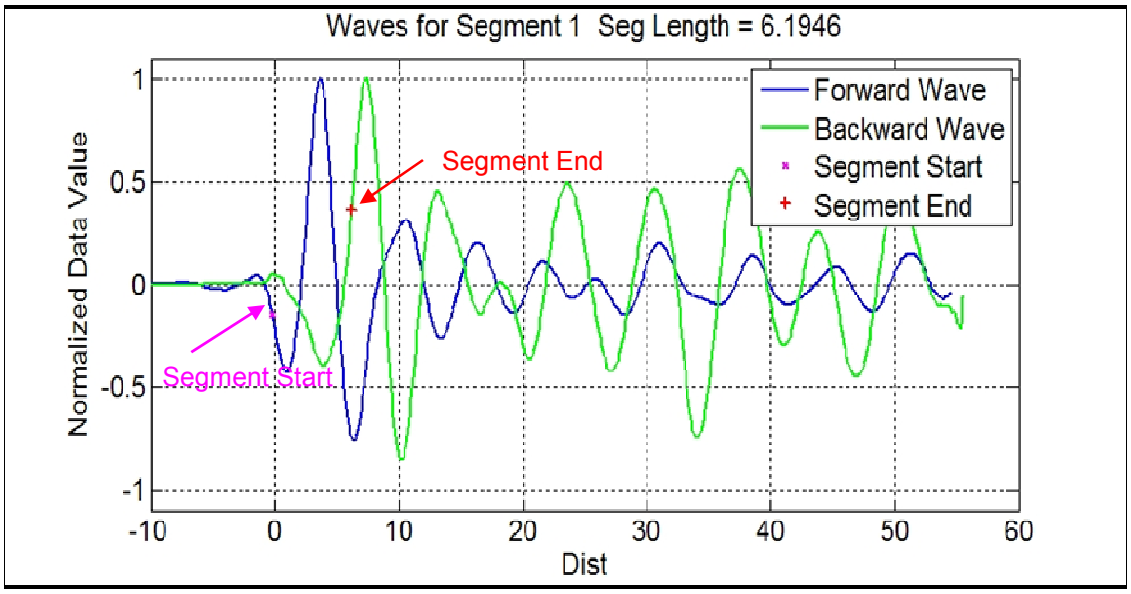

Figure 32: Test 3-1 - Reconstructed waves collected from segment 1.

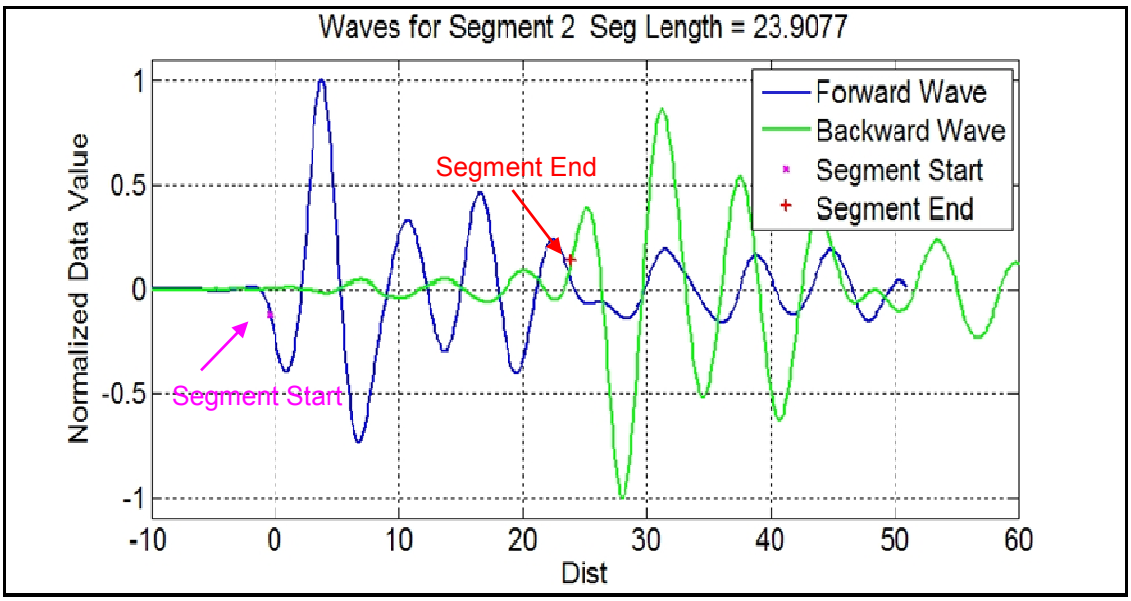

Figure 33: Test 3-1 - Reconstructed waves collected from segment 2.

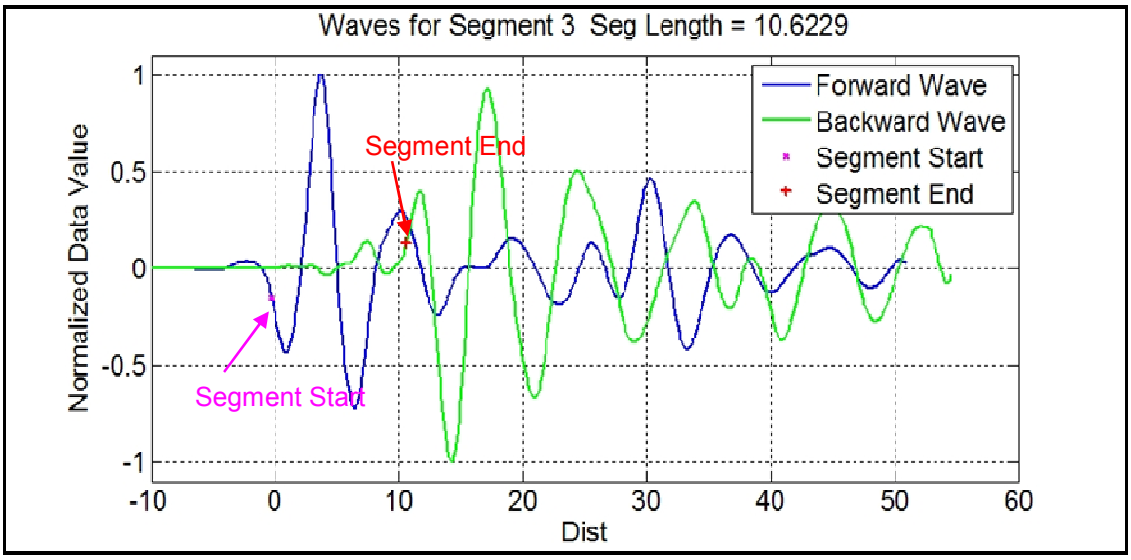

Figure 34: Test 3-1 - Reconstructed waves collected from segment 3.

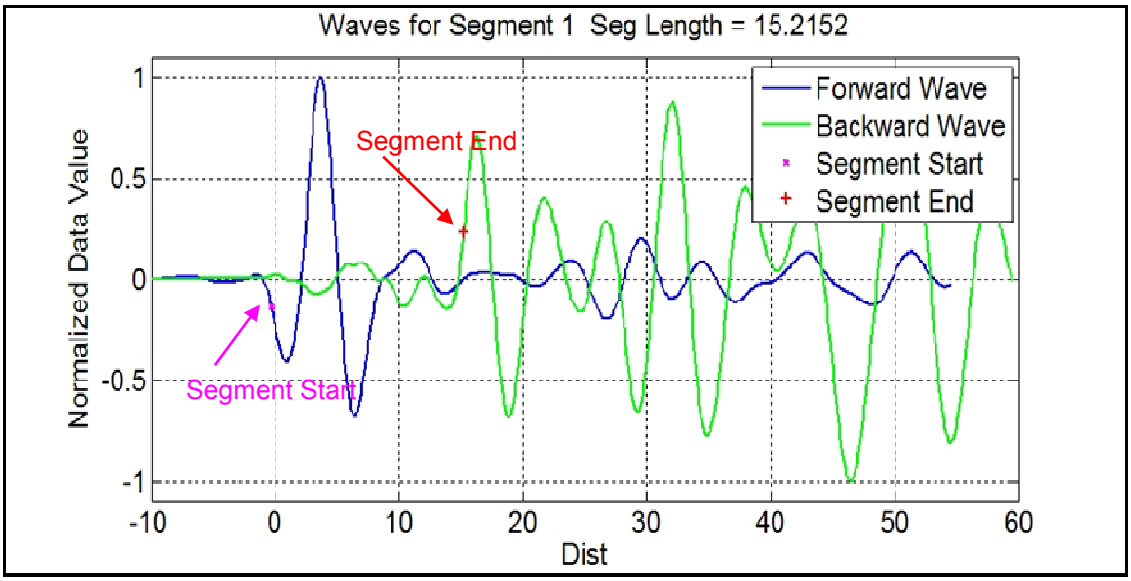

Figure 35: Test 3-2 - Reconstructed waves collected from segment 1.

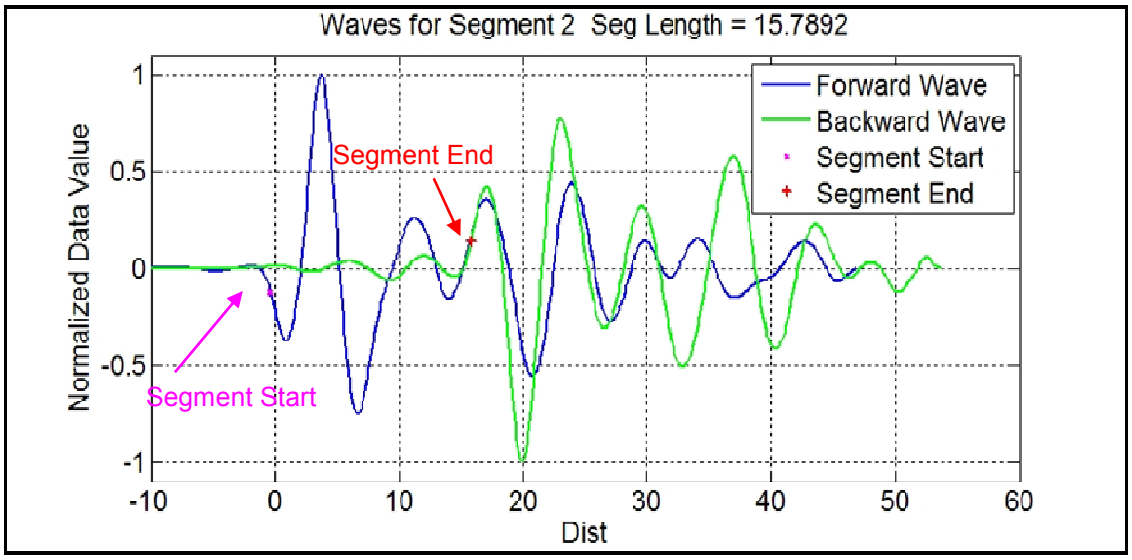

Figure 36: Test 3-2 - Reconstructed waves collected from segment 2.

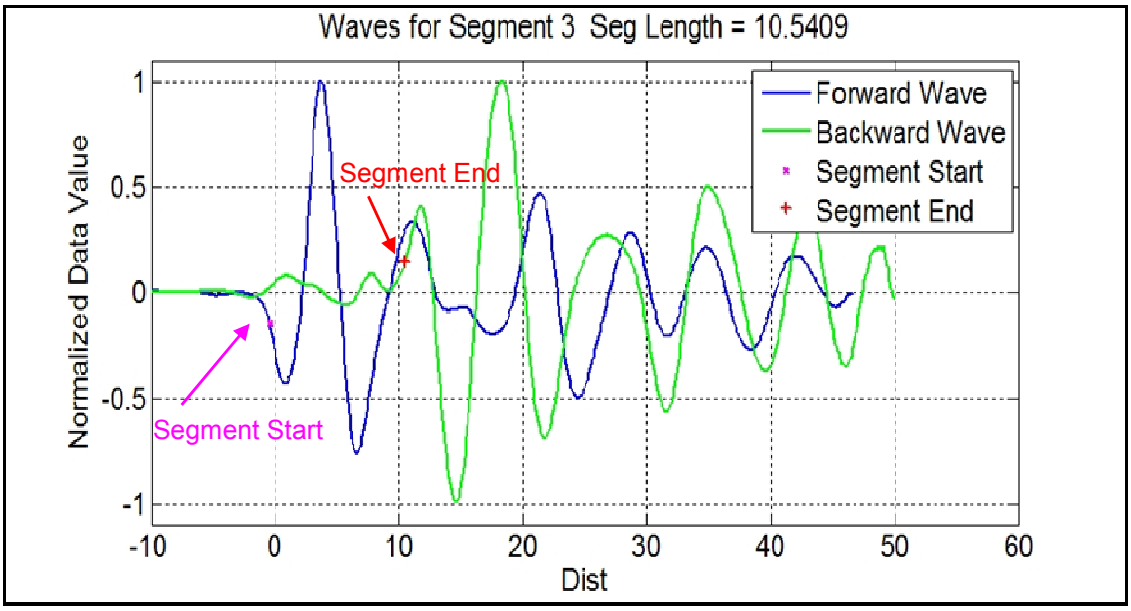

Figure 37: Test 3-2 - Reconstructed waves collected from segment 3.

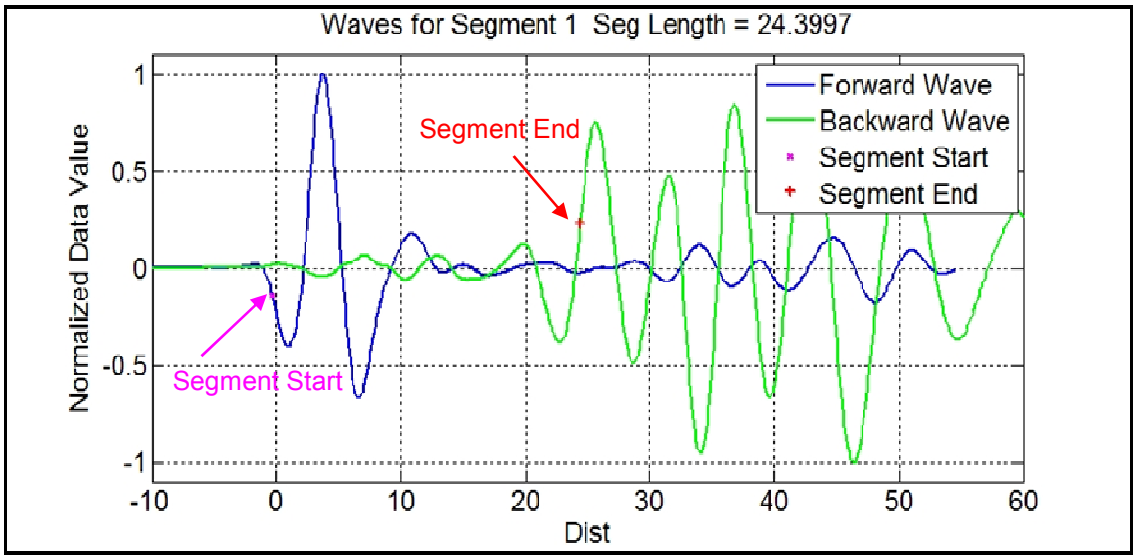

Figure 38: Test 3-3 - Reconstructed waves collected from segment 1.

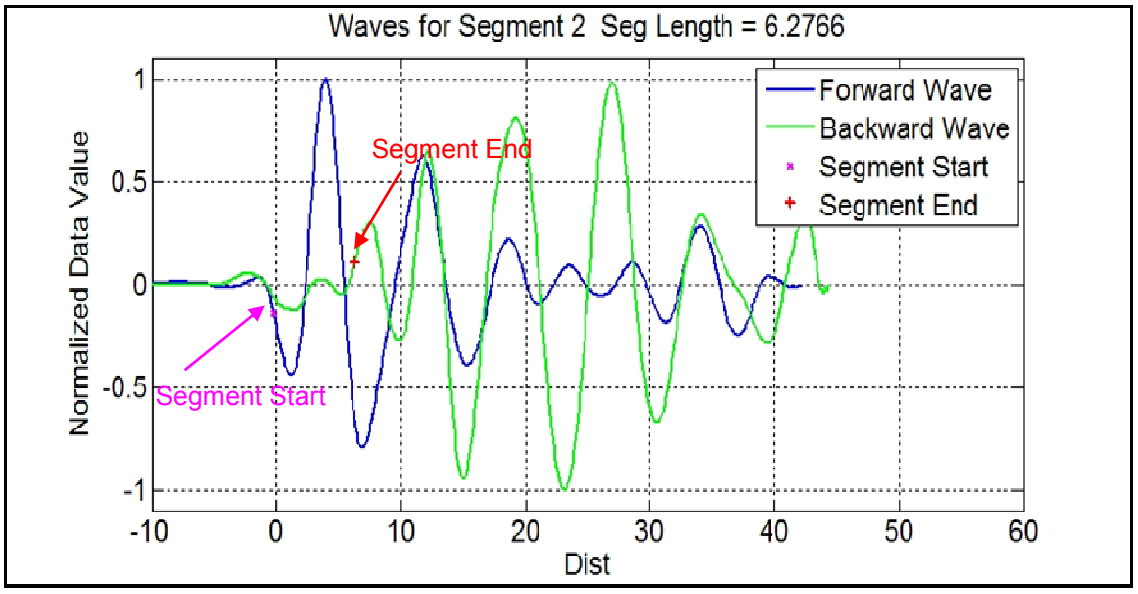

Figure 39: Test 3-3 - Reconstructed waves collected from segment 2.

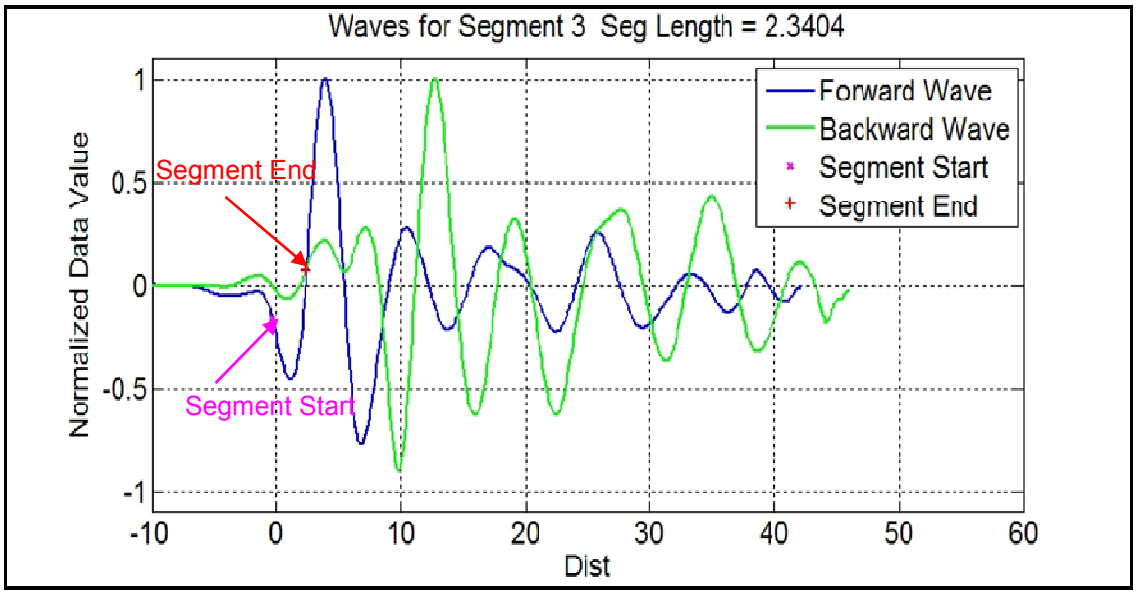

Figure 40: Test 3-3 - Reconstructed waves collected from segment 3.

4.2.1.2 Tests on Branched Wire (End of Segment 3 Shorted)

The following tests were performed while the end of segment 2 was left open, and end of segment 3 was shorted.

4.2.1.2.1 Test 3-4 (Branch Point at 6.5 Feet)

Figure 41, Figure 42, and Figure 43 show the resultant forward and backward traveling waveform reconstruction of each segment of a three-segment network with a branching point at 6.5 feet, an open circuit 24.5 feet past the branching point, and a short circuit 11 feet past the branching point on the other branch.

4.2.1.2.2 Test 3-5 (Branch Point at 14.5 Feet)

Figure 44, Figure 45, and Figure 46 show the resultant forward and backward traveling waveform reconstruction of each segment of a three-segment network with a

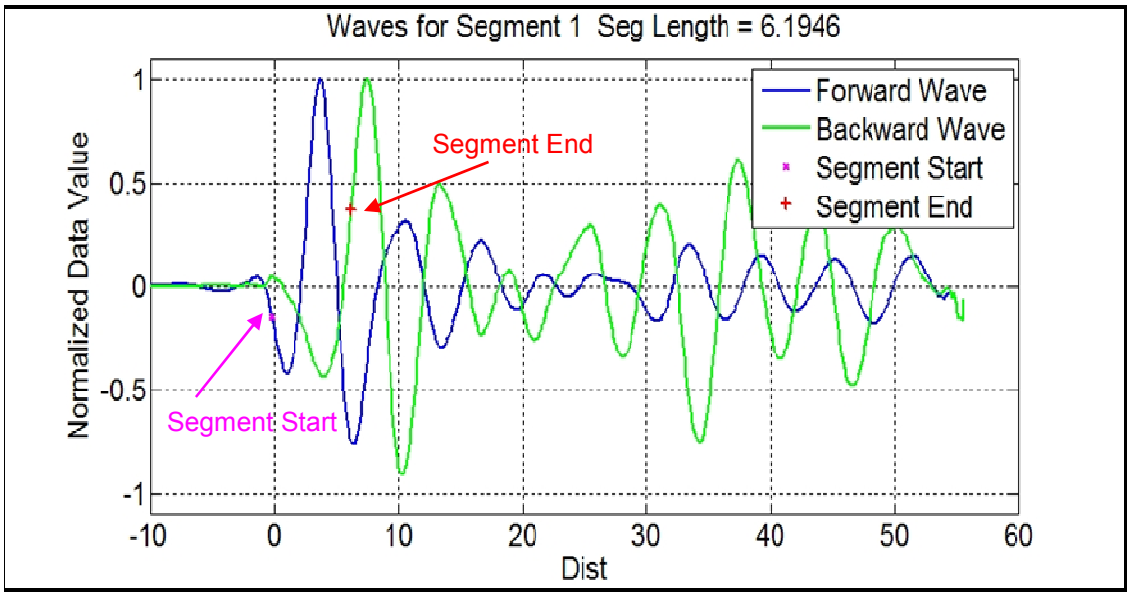

Figure 41: Test 3-4 - Reconstructed waves collected from segment 1.

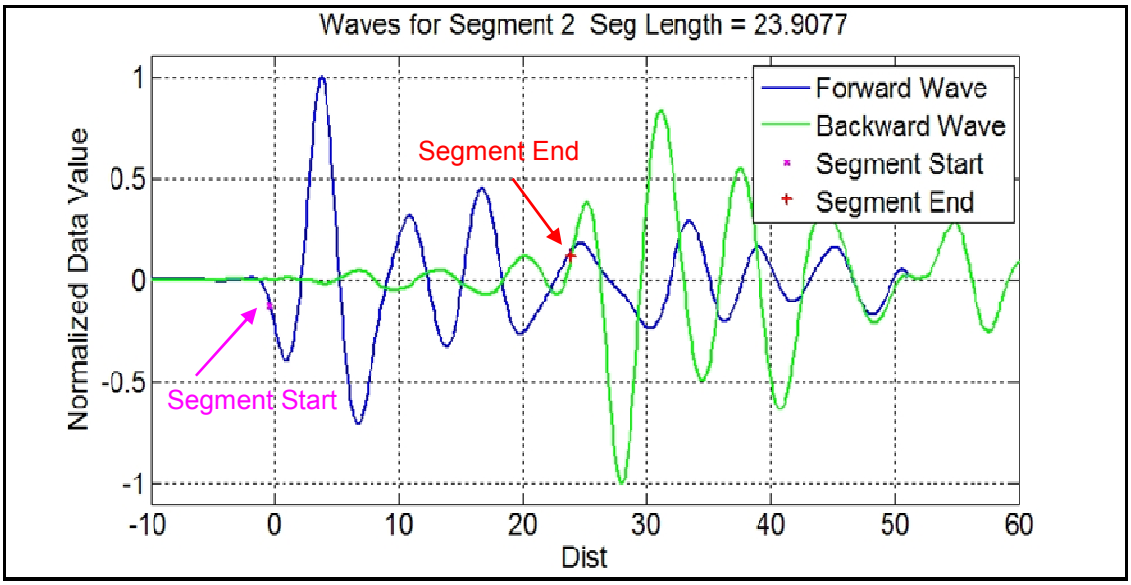

Figure 42: Test 3-4 - Reconstructed waves collected from segment 2.

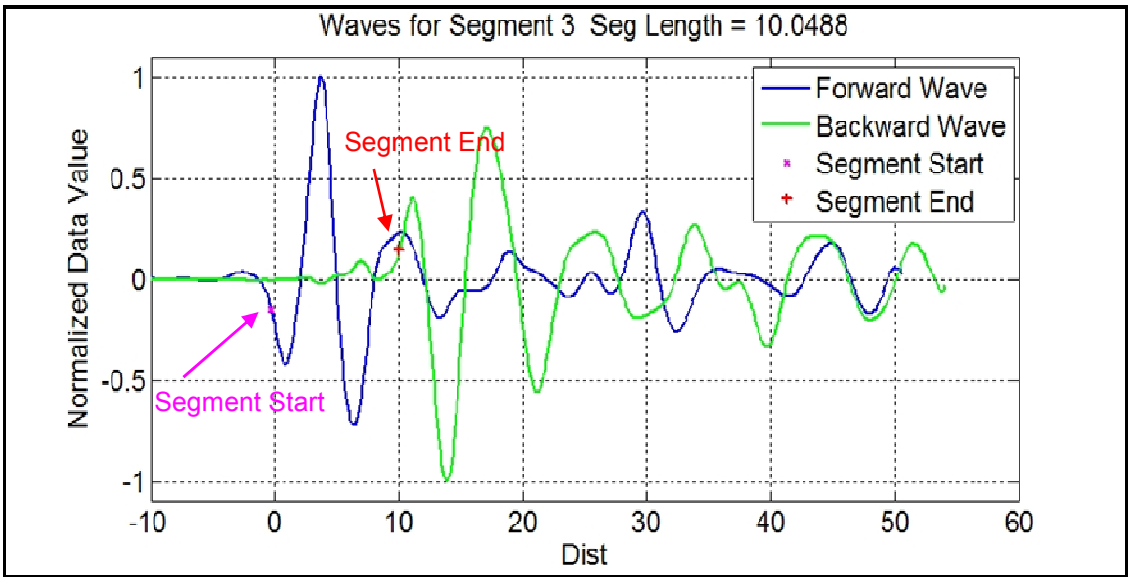

Figure 43: Test 3-4 - Reconstructed waves collected from segment 3.

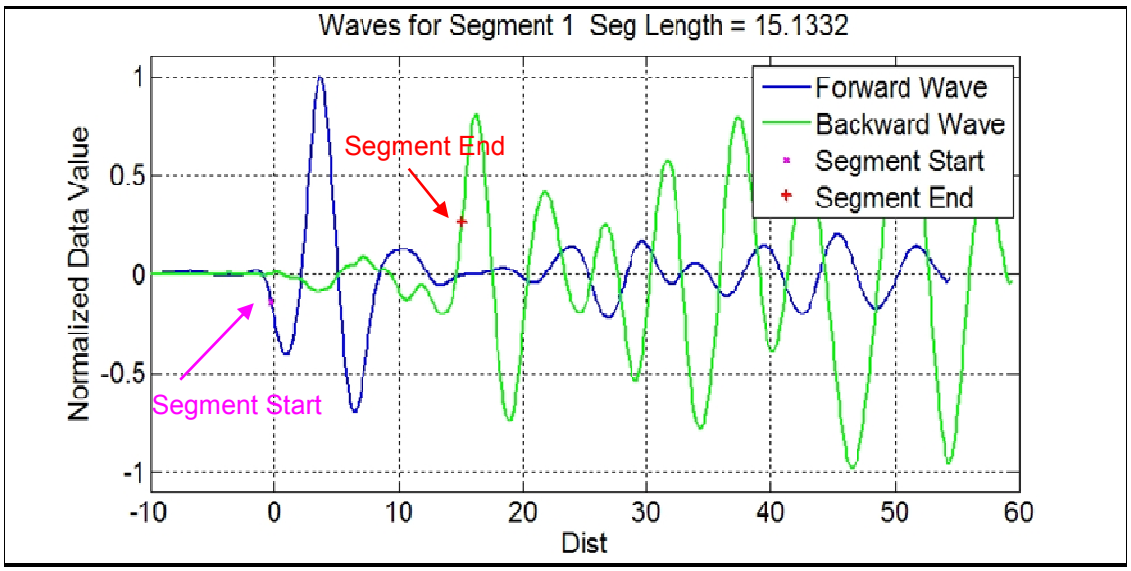

Figure 44: Test 3-5 - Reconstructed waves collected from segment 1.

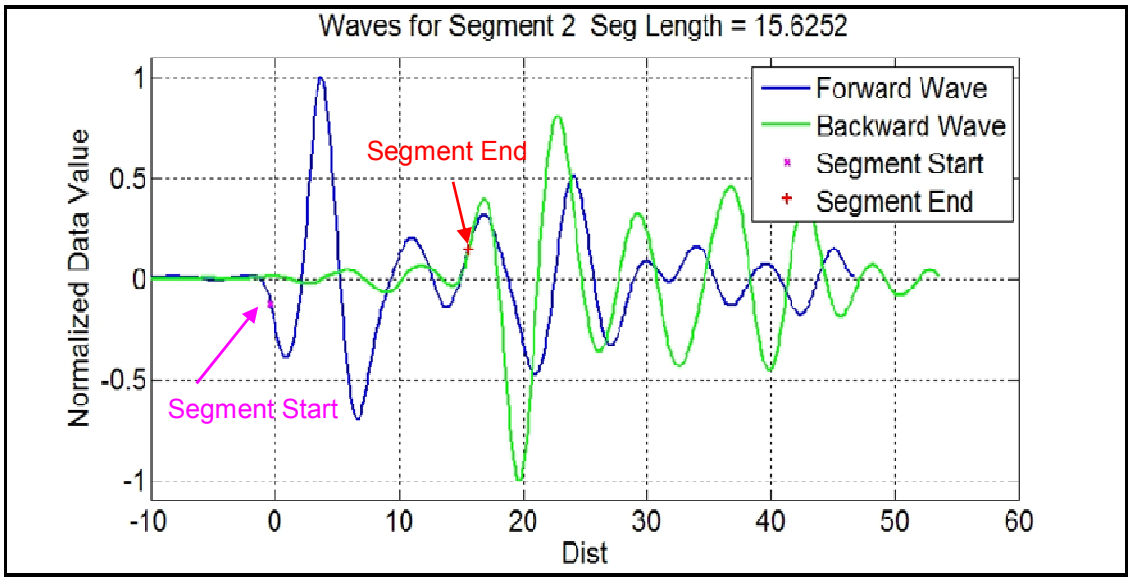

Figure 45: Test 3-5 - Reconstructed waves collected from segment 2.

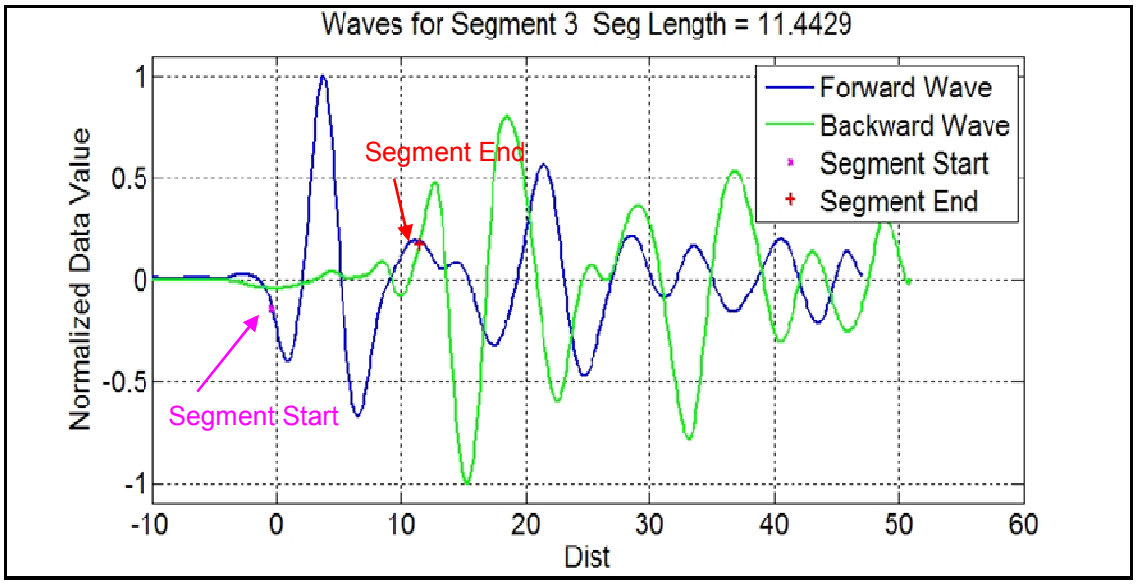

Figure 46: Test 3-5 - Reconstructed waves collected from segment 3.

branching point at 14.5 feet, an open circuit 16.5 feet past the branching point, and a short circuit 11 feet past the branching point on the other branch.

4.2.1.2.3 Test 3-6 (Branch Point at 23.5 Feet)

Figure 47, Figure 48, and Figure 49 show the resultant forward and backward traveling waveform reconstruction of each segment of a three-segment network with a branching point at 23.5 feet, an open circuit 7.5 feet past the branching point, and a short circuit 11 feet past the branching point on the other branch.

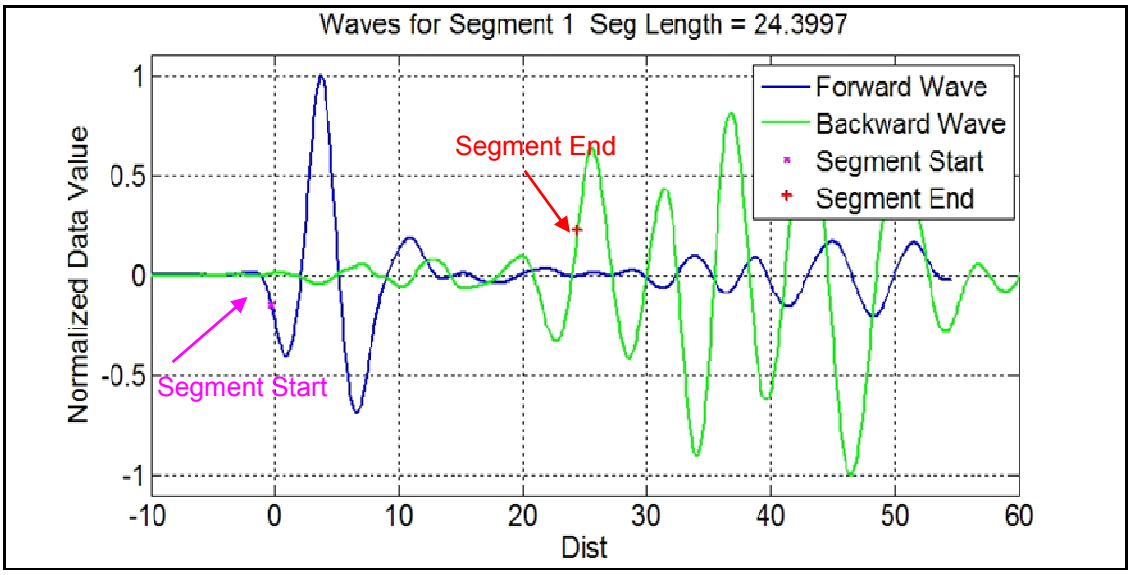

Figure 47: Test 3-6 - Reconstructed waves collected from segment 1.

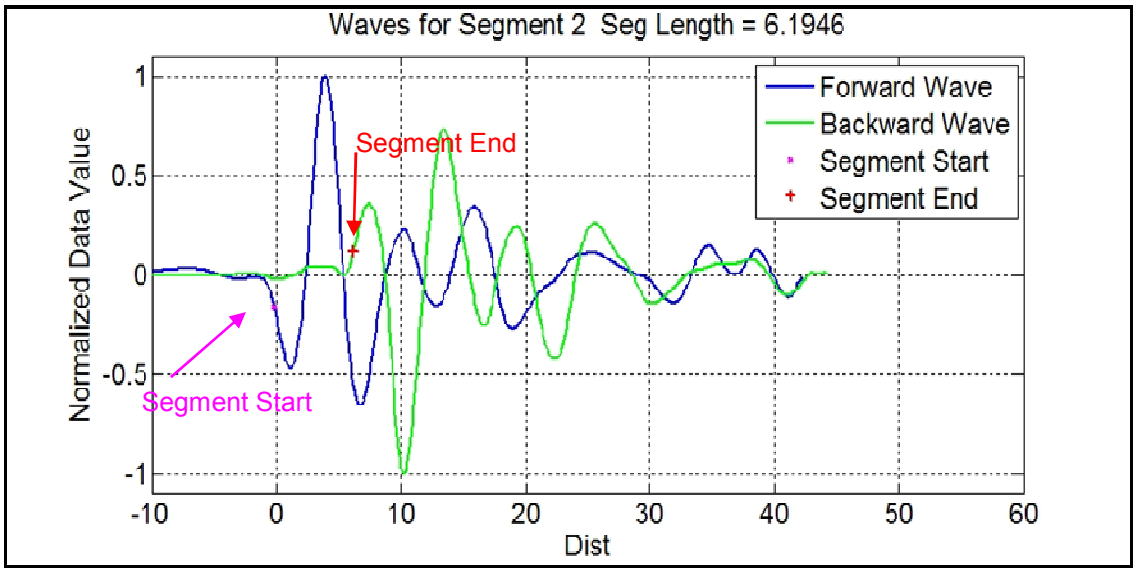

Figure 48: Test 3-6 - Reconstructed waves collected from segment 2.

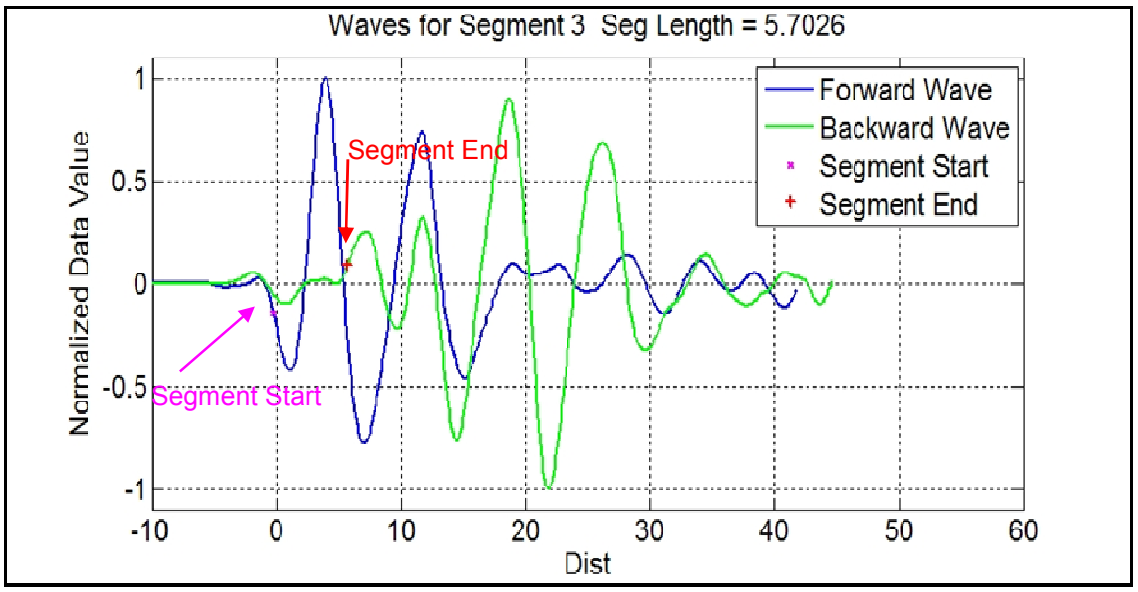

Figure 49: Test 3-6 - Reconstructed waves collected from segment 3.

4.2.2 Summary of Results

The erroneous wave is very likely caused by signals reflecting off of the branch not being tested. The case in which this can occur is when the branch not under test is shorter than the branch under test. The signals could reflect off the branch not under test and then be picked up by the probe because it is still in close proximity to that branch while testing at the head of the branch.

This issue could be solved by employing differentially paired antennas, spaced a short distance from each other, possibly allowing signals being sensed from neighboring branches to be filtered out or significantly diminished.

Table 3 contains a summary of the three-segment network results. Results that do not meet the target accuracy of 1.5 feet are highlighted in yellow. For all the test cases shown for the three-segment network, the accuracy in identifying the location of features at the end of a segment improved.

Two test cases did not meet the target accuracy of being within 1.5 feet. Because a short circuit and open circuit at the end of a cable have very similar characteristics, these test cases can be considered similar in nature, and the cause of the error is very likely to be the same for both cases. Upon inspection of the reconstructed reflection model for these erroneous cases, we can see that while the expected wave exists in the model, a second wave exists in the model at the closer distance, thus causing the error. The erroneous wave is marked with an arrow on Figure 50.

This erroneous wave is very likely caused by signals reflecting off of the branch not being tested. The case in which this can occur is when the branch not under test is shorter than the branch under test. The signals could reflect off the branch not under test

Table 3. Summary of the Three-Segment Branched Network Test Results

3-Segment Test Result Summary						
Test	Segment	Feature of Interest	Measured length	Calculated Length	Error (feet)	% Error
3-1	1	branch	6.5	6.19	0.31	4.7%
	2	open	24.5	23.91	0.59	2.4%
	3	open	11.0	10.62	0.38	3.4%
3-2	1	branch	14.5	15.22	0.72	4.9%
	2	open	16.5	15.79	0.71	4.3%
	3	open	11.0	10.54	0.46	4.2%
3-3	1	branch	23.5	24.40	0.90	3.8%
	2	open	7.5	6.28	1.22	16.3%
	3	open	11.0	2.34	8.66	78.7%
3-4	1	branch	6.5	6.19	0.31	4.7%
	2	open	24.5	23.91	0.59	2.4%
	3	full short	11.0	10.05	0.95	8.6%
3-5	1	branch	14.5	15.13	0.63	4.4%
	2	open	16.5	15.63	0.87	5.3%
	3	full short	11.0	11.44	0.44	4.0%
3-6	1	branch	23.5	24.40	0.90	3.8%
	2	open	7.5	6.19	1.31	17.4%
	3	full short	11.0	5.70	5.30	48.2%

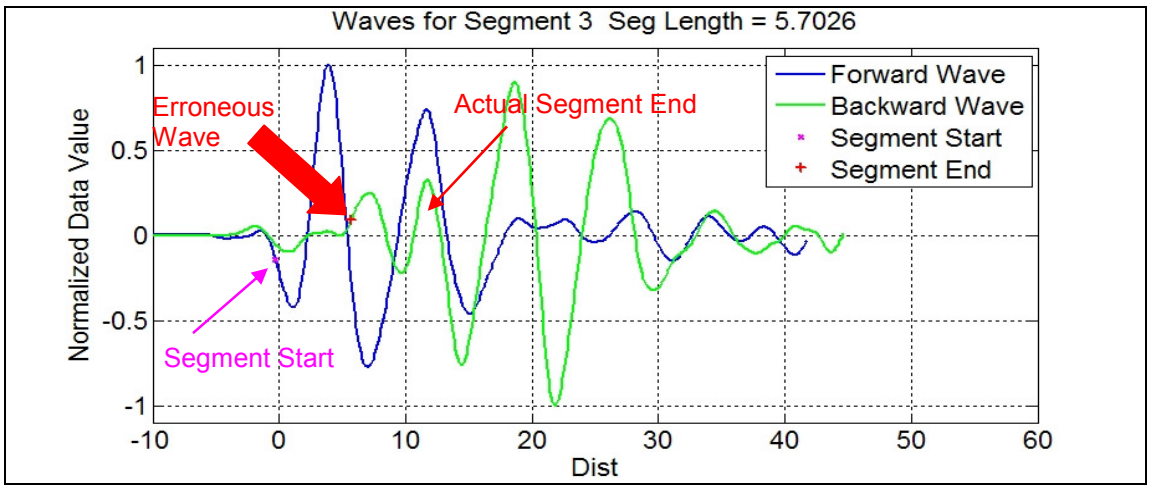

Figure 50: Test 3-6 - Reconstructed waves collected from segment 3 – Erroneous Wave.

and then be picked up by the probe because it is still in close proximity to that branch while testing at the head of the branch.

This issue could be solved by employing differentially paired antennas, spaced a short distance from each other, possibly allowing signals being sensed from neighboring branches to be filtered out or significantly diminished.

4.2.3 Known Limitations of the Test Configuration

The network topology graph will often overestimate the length of a segment, particularly if the segment end is an endpoint of the wire bundle.

The order in which probe tests are performed is important. Jumping between segments, performing less than the minimum number of tests per segment, or testing a child segment before its parent is not recommended during the initial scan. Once the entire network has been properly scanned, tests can be performed at any location, on any segment. Whenever a new fault test is performed, the Test ID is incremented and the network topology is flushed, requiring an initial scan with the probe to be performed.

If a particular test is deemed by the software to be unusable, the data are not included in the analysis. This occurs due to a weak or noisy signal.

4.3 Network Topology Results

The following tests were performed on a two-segment and three-segment test cord. This dual wire, untwisted cord was specifically chosen to represent the controlled condition with the least interference from external factors. The branched point and types of faults are the variable factors between the tests. In the following waveform models the y-axis scaling is shown to indicate relative amplitude of each composite waveform and is

normalized to the maximum of the signal. The segment length is calculated from the waveform, and the node distance was calculated from the maximum model error algorithm. The network topology is calculated using the node distance first, then the estimated segment length. The measured network configuration is described in Table 4.

The network topology for Test 1-1 that was calculated by the network algorithm is depicted in Figure 51. Figure 52 shows the resultant backward traveling waveform reconstruction of each segment of a two-segment network with a short circuit at 14.5 feet, an open circuit at 16.5 feet past the fault.

The network topology for Test 1-2 that was calculated by the network algorithm is depicted in Figure 53. Figure 54 shows the resultant backward traveling waveform reconstruction of each segment of a three-segment network with a branching point at 14.5 feet, an open circuit at 16.5 feet past the branching point, and an open circuit 11 feet past the branching point on the other branch.

Two test cases are shown to represent the data collected in this category. Table 5 shows a summary of the results of the representative two-wire reference tests for mapping a network topology.

Test 1-2 shows the successful analysis of a branched network under simple conditions. During the development of the algorithm, the ability to map a branched network with these conditions has been very repeatable. Noise levels during these two-wire tests are low enough to allow the branch to be detected.

Test 1-1 shows the difficulty the network algorithm has in finding short circuits that exist in non-endpoint locations. While these faults are sometimes detected during lab tests, the network algorithm has proven to be unreliable at detecting this type of fault.

Table 4: Two-Wire Test Configurations

Simple 2-Wire Test Configurations		
Test	# of Segments	Configuration Description
1-1	2	Seg 1 = 14.5ft, Short at 14.5ft, Seg 2 = 16.5ft
1-2	3	Seg 1 = 14.5ft, Branch at 14.5ft, Seg 2 = 16.5ft, Seg 3 = 11ft

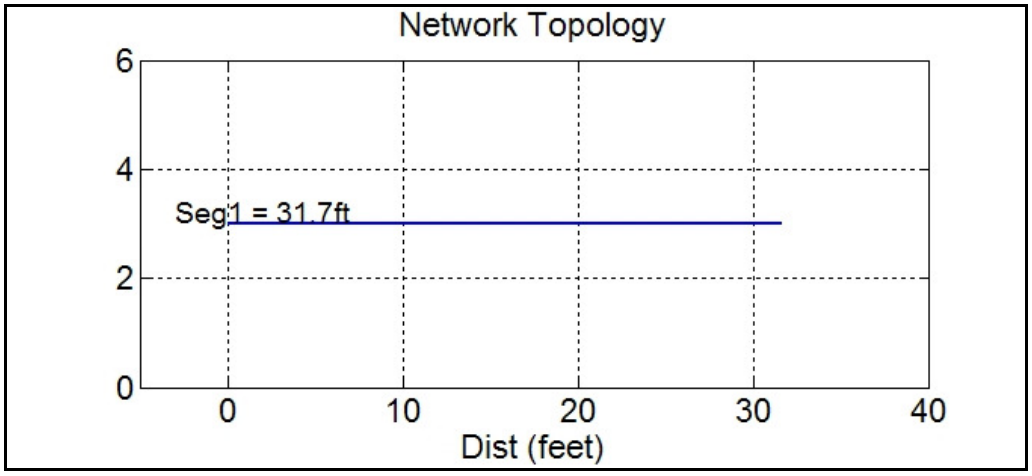

Figure 51: Test 1-1 - Network topology calculated by the network algorithm

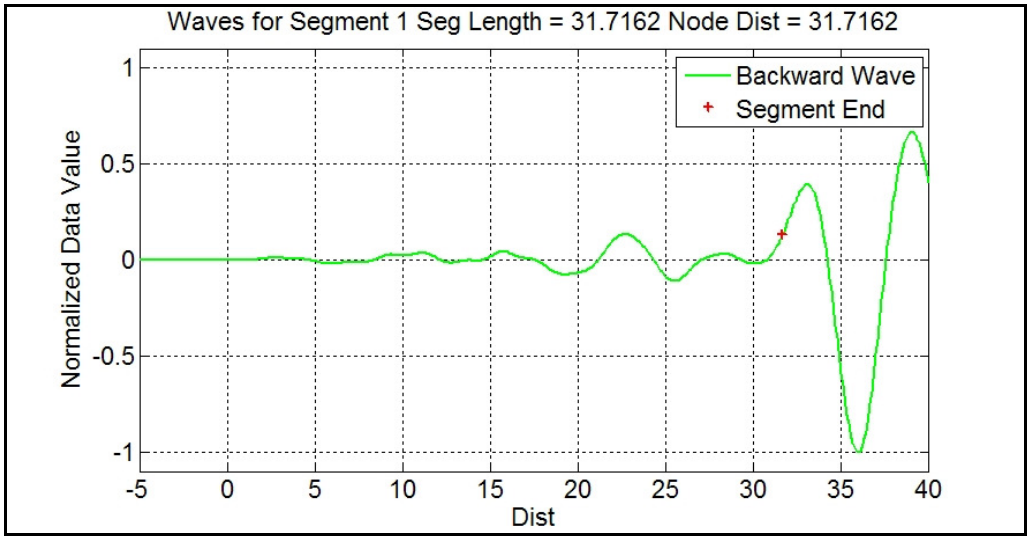

Figure 52: Test 1-1 - Reconstructed reverse-traveling waves

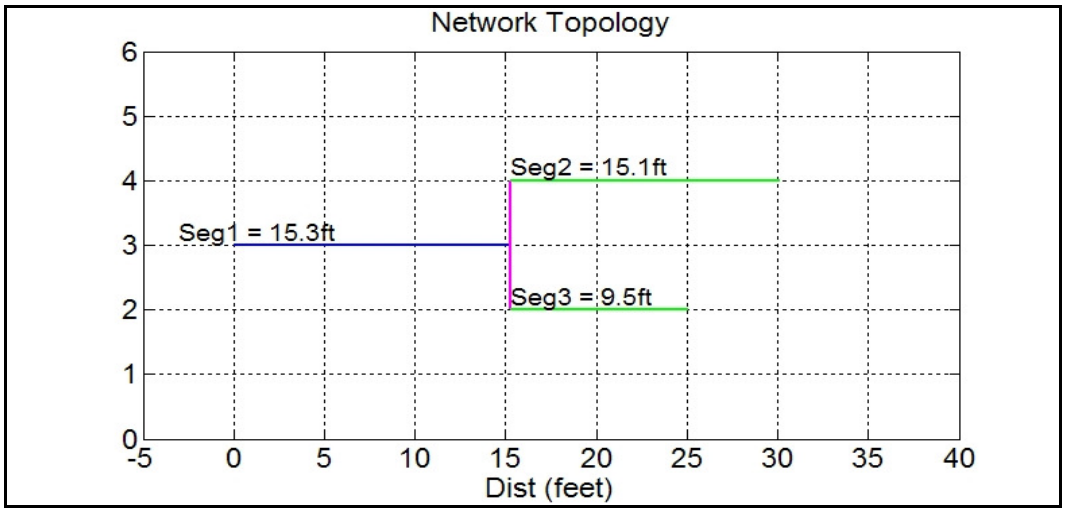

Figure 53: Test 1-2 - Network topology calculated by the network algorithm

Table 5: Two-Wire Test Result Summary

Two-Wire Test Result Summary						
Test	Segment	Feature of Interest	Measured length	Calculated Length	Error (feet)	% Error
1-1	1	short	14.5	31.70	17.20	118.6%
	2	open	16.5	0.00	16.50	100.0%
1-2	1	branch	14.5	15.30	0.80	5.5%
	2	open	16.5	15.10	1.40	8.5%
	3	open	11.0	9.50	1.50	13.6%

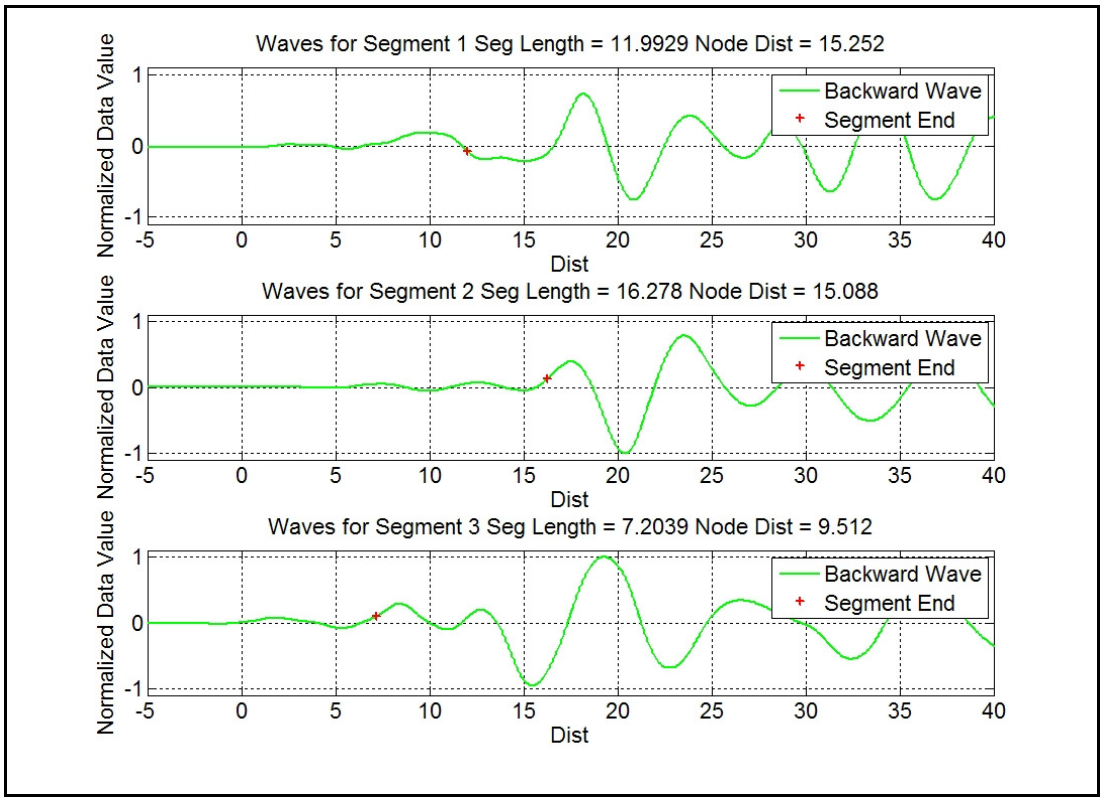

Figure 54: Test 1-2 - Reconstructed reverse-traveling waves.

The waveform caused by the short is insignificant compared to the waveform caused by the end of the wire. Figure 55 shows the reconstructed reverse-traveling waves for test 1-1. Notice that the calculated segment end is at the end of the wire. The actual waveform that should have been used as the segment end is circled. Previous testing has shown the ability to detect this type of fault. The main difference with the testing in this report is the fact that no previous knowledge about the network topology was applied to finding the solution.

Resolving this issue is not a simple task. If the sensitivity of the wave detection algorithm is increased, erroneous waves will be detected. Significant research and algorithm development are necessary to improve the algorithm enough to be able to reliably detect short circuits at non-endpoint locations without prior knowledge of their location. This will involve improving the data collection, data processing, and network algorithm so that waves caused by shorts are always more significant than erroneous waves.

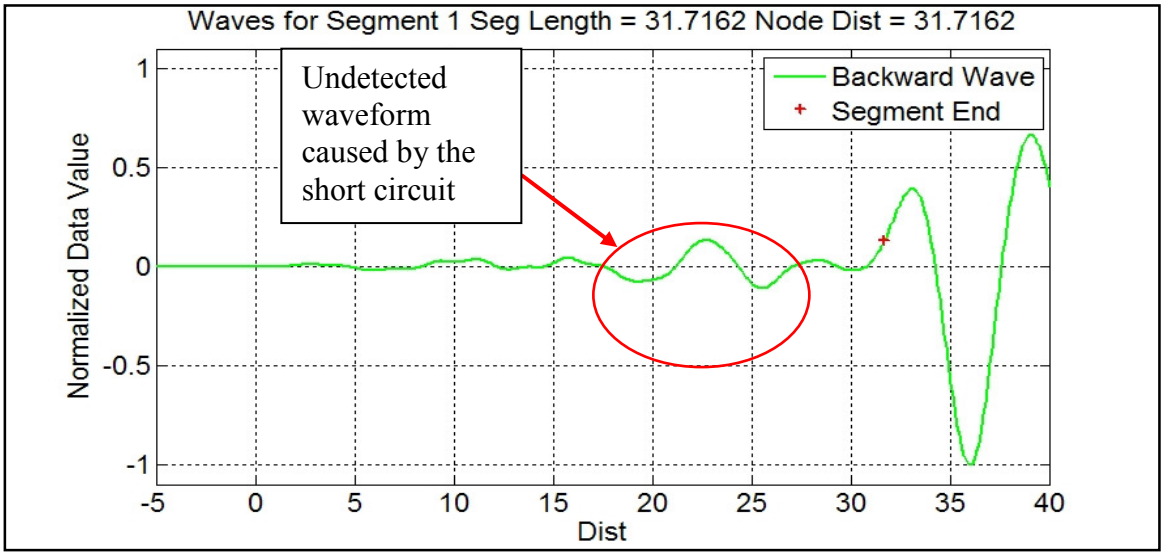

Figure 55: Test 1-1 - Reconstructed reverse-traveling waves with the short circuit indicated.

CHAPTER 5

CONCLUSIONS

5.1 Summary

This thesis has explored state of the art applications of Spread Spectrum Time Domain Reflectometry (SSTDR) and other systems that are related to testing aging aircraft wiring. It has reviewed other current solutions for cable fault detection on branched wiring and their limitations, mainly the lack of a method to reliably guide an aircraft wiring maintainer to a precise physical location of an existing fault on an un-branched or branched wire. The method of the proposed solution, using spread spectrum technology with wave separation data analysis techniques to nondestructively find faults and cable topology, has been described. Using the method described with the proper hardware could allow the maintainer to quickly locate faults or other specific points of interest along the wire, even if the wire bundles are hidden behind nonmetallic paneling, as is common in the interior of aircraft.

5.2 Future Work

Preliminary testing in noisy environments indicated that more testing in real environments is needed to determine the major possible sources of errors and interference. Additional study should pay particular attention to the signal cross-talk

effects of additionally bundled wires as they are routed next to and around the test wire, and also as they are routed away from the test wire.

It was found during simulation that at least 6 rows of data are required to gain a sufficient understanding of the model, if not more. Significant improvements to the algorithm could be made by using a priori [13] SSTDR wave model to predict the shape of the waveform, and thereby more quickly develop accurate traveling wave models. Wires shorter than the requisite 6 feet could be tested properly by arriving at the correct model using fewer required rows, and thus shorter distances. This could improve the practical functionality of the algorithm for providing information about a wider variety of wiring applications.

Other reflectometry methods could benefit from the ability to separately model the forward and backward traveling waves. Research could be conducted to find out if other reflectometry waveforms may lend themselves for easier signal analysis.

This algorithm has the potential to be applied to several disciplines of study and applications. This method could be useful in 3-D modeling and reconstruction, where data are collected from multiple points of reference, and the model is separated into distinct groups of desirable characteristics.

5.3 Conclusions

This thesis has developed and quantified the ability to separate and model reflectometry signals in order to characterize simple unbranched and branched wiring network topologies. Data were collected using a reflectometry system in tandem with a field sensor at multiple positions, analyzed, and information about that network was displayed to the user.

The use of an EM probe and wire tester to collect data at multiple points along a test wire for reconstructive analysis in Matlab was demonstrated in a controlled environment. Under limited conditions the technology is capable of accurately modeling a cable network without prior knowledge of the topology, revealing the validity of numerical data inversion for this application. By using inversion and multiple EM sensor positions, waves can be isolated into their respective models. This enables algorithms to more successfully calculate the distance to those waves, in turn providing a more accurate distance to the fault, branch, or endpoint, and ultimately a more accurate network topology. Simulation and test results support the ability to physically locate a fault within and error margin of 1.5 feet in most simple situations. Test results show that the error margin was greater than 1.5 feet in certain cases, particularly with more complex wire branches.

While wave separation is a useful tool for clarifying the location of anomalies, limitations have been described that affect the detection and accuracy of the system. In summary these limitations include cable segments shorter than approximately 6 feet, separation of segments, external noise sources, under-sampling, and wave distortion caused by metallic interference.

The purpose of the developed method is to reliably guide an aircraft wiring maintainer to the precise location of an existing fault on an unbranched and branched wire. Using the method described with the proper hardware could allow the maintainer to quickly find the physical location of the fault, even if the wire bundles are hidden behind nonmetallic paneling, as is common in the interior of aircraft.

REFERENCES

[1] Conley, T., *The Relationship Among Component Age, Usage (Reliability) and Cost of Naval Aviation Repairables*, Aging Aircraft Conference, Sep. 2003.

[2] Furse, C., Lo, C., Chung, Y., Smith, P., Pendayala, P., Nagoti, K., *Spread Spectrum Sensors for Critical Fault Location on Live Wire Networks,* 12, Salt Lake City: Wiley InterScience, 2005.

[3] Furse, C., Haupt, R.L., *Down to the Wire: The Hidden Hazard of Aging Aircraft Wiring.* IEEE Spectrum, February, 2001.

[4] Hall, J., In the matter of investigation of incident involving Trans World Airlines, Inc. Flight 800. [Online] December 1997. http://www.ntsb.gov/events/twa800/exhibits/th971211.pdf.

[5] LiveWire Test Labs, Inc. *LiveWire Handheld Tester Operation Guide.* 2007.

[6] LiveWire Test Labs, Inc. *Theory and Resolution for Near-field Sensing.* 2006.

[7] Nagoti, K., Lo, C., Furse, C., *Mapping of Wiring Network Topologies Using Reflectometry Methods.* IEEE Sensors Journal. December, 2005.

[8] Pozar, David M. *Microwave Engineering.* Amherst : Wiley, 2005.

[9] Ranter, H., Lujan, F., Swissair 111 special action. *www.aviationsafety.net.* [Online] http://www.aviationsafety.net/specials/sr111/main.htm.

[10] Slaney, M. and Kak, A.C., *Principals of Computerized Tomographic Imaging.* New York : IEEE Press, 1987.

[11] Smith, P., Furse, C., Gunther, J., *Fault Location on Aircraft Wiring using Spread Spectrum Time Domain Reflectometry*, IEEE Sensors Journal, Vol. 5, No. 6, pp. 1469-1478.

[12] Thiele, G. A. and Stutzman, W. L., *Antenna Theory and Design.* Danvers : Wiley, 1998.

[13] Zhdanov, Michael S. *Geophysical Inverse Theory and Regularization Problems.* New York : Elsevier Science, 2002.